Thin Films Deposition for Energy Efficient Windows and Solar Cells

CHEN, S

Thin Films Deposition for Energy Efficient Windows and Solar Cells

Shuqun Chen

Thesis Submitted in Partial Fulfilment for Requirements of Doctor of Philosophy

Declarations

I, Shuqun Chen, confirm that the research included within this thesis is my own work or that where it has been carried out in the collaboration with, or supported by others, that this is duly acknowledged below and my contribution indicated. Previously published material is also acknowledged below.

I attest that I have exercised reasonable care to ensure that the work is original, and does not to the best of my knowledge break any UK law, infringe any third party's copyright or other Intellectual Property Right, or contain any confidential material.

I accept that the College has the right to use plagiarism detection software to check the electronic version of the thesis.

I confirm that this thesis has not been previously submitted for the award of a degree by this or any other university.

Signature:

Date:

Acknowledgements

First of all, I wish to express my gratitude to my supervisor Dr. Russell Binions for his invaluable help throughout my PhD. His continued support, guidance and patience have made the past 3.5 years a very productive and enjoyable time. I would also like to thank Dr. Luz Romero, Dr. Michael E.A. Warwick and Dr. Nuruzzaman Noor, who have provided tremendous help in the beginning of my research.

I am grateful to my amazing colleagues and friends, Louise Anderson, Pelin Yimaz, Alex Winbawa, Dr. Yongfei Cui, Dr. Nimra Jalali and Shi Yi all other people from SEMS office 372 and postgraduate hub. Dr. Joe Briscoe is especially thanked for many valuable discussions. Dr. Rory Wilson is acknowledged for the support in XRD measurements and crystal lattice parameters calculations. Dr. Andrei Sapelkin is thanked for performing photoluminescence tests. Prof. Davide Barreca from Padova University and Prof. Ivan Parkin from University of College London are acknowledged for assistance in XPS measurements. Dr. Qijing Cheng from Xiamen University is thanked for the TEM analysis.

My deepest appreciation belongs to my wife and family for their great patience and understanding.

Abstract

This work mainly investigates the use of aerosol assisted chemical vapour deposition (AACVD) process to fabricate thin film materials for energy efficient glazing and thin film solar cells applications.

Ga-doped ZnO thin films were firstly deposited onto glass substrates by AACVD of zinc and gallium acetylacetonates in methanol. After optimizing the doping concentration, film thickness and heating temperature, ZnO:Ga coatings with high visible transparency (> 80 %) and infrared reflection (up to 48.9 % at 2500 nm) were obtained, which is close to the optical requirements for commercial energy saving glazing. Pyramid-shaped and plate-shaped zinc oxides films were then deposited on glass substrates by AACVD of zinc-acetate-dihydrate, acetic acid and deionized water in methanol. These surface-textured ZnO films exhibited good visible transparency (~70 %), low sheet resistance (~60 Ω sq^{-1}) and ultra large haze factor (up to 98.5 %), which is the most hazy ZnO ever reported and can be potentially used as the front contact in thin-film solar cells. Finally, uniform compact $CH_3NH_3PbI_3$ perovskite films with high phase purity and micron-sized pinhole-free grains were deposited on glass substrates by a novel two-step and three-step sequential AACVD process.

In conclusion, AACVD shows a great potential for the scalable fabrication of ZnO-based and organometallic halide-based thin film materials.

Table of Contents

List of Figures

Chapter 2

Chapter 5

Chapter 6

List of Tables

Chapter 7

List of Equations

Chapter 6

List of Abbreviations

CVD: Chemical Vapour Depositon

AACVD: Aerosol Assisted Chemical Vapour Deposition

APCVD: Atmospheric Pressure Chemical Vapour Deposition

LPCVD: Low Pressure Chemical Vapour Deposition

MOCVD: Metal Organic Chemical Vapour Deposition

PECVD: Plasma Enhanced Chemical Vapour Deposition

UHVCVD: Ultrahigh Vacuum Chemical Vapour Deposition

TCO: Transparent Conducting Oxide

ITO: Tin-doped Indium Oxide

FTO: Fluorine-doped Tin Oxide

PVD: Physical Vapour Deposition

DEZ: Diethylzinc

PV: Photovoltaic

SEM: Scanning Electron Microscope

EDS: Energy-dispersive X-ray Spectrometer

TEM: Transmission Electron Microscope

XRD: X-ray Diffraction

XPS: X-ray Photoelectron Spectroscopy

AFM: Atomic Force Microscopy

PL: Photoluminescence

BE: Bind Energy

RMS: Root Mean Square

ZAD: Zinc-acetate-dihydrate

IPA: Isopropyl Alcohol

MEA: Monoethanolamine

DMF: N,N-Dimethylformamide

DFT: Density-functional Theory

Chapter 1 Introduction

1.1 Background

Global energy demand has been continually increasing with industrial development and population growth in recent decades, especially for conventional energy resources such as oil, coal and natural gas. To date, over 80 % of energy consumption is generated from fossil fuels and this causes environmental pollution and global warming issues.[1] Buildings are said to be responsible for about 40 % of the world's total annual energy consumption and 30 % of all carbon dioxide emissions due to the excessive use of lighting, air-conditioning and heating.[2,3] These numbers will continue to grow as increasingly larger areas of the world become developed and greater numbers of buildings are constructed.[4] Currently, there are two important approaches to reduce energy costs for buildings. The first one is to use thin film coatings on building glazing to limit the amount of solar radiation entering (for hot climates) or blackbody radiation leaving (for cold climates) a building. The second one is to employ rooftop photovoltaic systems to convert solar energy into electricity.

Transparent conducting oxides (TCOs) can be used as energy efficient window coatings if they 1) have a wide band gap (usually greater than 3 eV) which enables them to transmit light in the visible spectrum and 2) have a high carrier density (10^{20} to 10^{21} cm^{-3}) that can induce plasma reflection in the near infrared light.[5] Tin-doped indium oxide (ITO) and fluorine-doped tin oxide (FTO), for example, have

been widely employed as energy efficient glazing coatings.[6] As a new generation TCO material, zinc oxide has been extensively investigated in recent years for its large band gap, high chemical and thermal stability, low cost with no toxicity and ease of fabrication or patterning.[7] Thus, doped ZnO films become a promising candidate for new energy efficient coating.

The other important application of TCOs is their function as electrical electrodes in thin-film solar cells. This is especially true when the TCO layer is surface textured because a rough surface can bring efficient light scattering inside the solar cell and, therefore, enhances light absorption along the longer scattering path, leading to an increase of the photo-generated current.[8,9] A proven example is the growth of transparent conductive B-doped ZnO films with random pyramidal texture by means of low pressure chemical vapour deposition (LPCVD), which has already been successfully employed in commercial silicon solar modules.[10,11] Unfortunately, the volatile zinc precursor diethylzinc (DEZ) used is highly pyrophoric and expensive.[12] Therefore, continuous efforts are being made by the CVD community to explore novel cost-effective techniques and precursors for textured ZnO materials.

During the past several years, organometallic halide based perovskite thin film solar cells have emerged as a leading next-generation photovoltaic (PV) technology. The certificated device power-conversion efficiency has increased significantly from 3.8 % in 2009 to 21.0 % in 2015,[13] and further efforts are being made to push this value toward and beyond that of crystalline silicion (25 %).[14] The key material in perovskite solar cells is the organometallic halide. Methylammonium lead iodide

($MAPbI_3$), for example, is a semiconducting pigment with a direct band gap of 1.55 eV, a high optical absorption coefficient ($\alpha = 10^4$-10^5 cm^{-1} in 300-780 nm), and a long electron/hole diffusion (exceeding 1 μm in polycrystalline film), which makes this material a good light harvester in solar cells.[15] The morphology and crystal structure of organometallic halide absorbers are key parameters for maximizing pervoskite solar cells efficiency, both being strongly influenced by the deposition method used.

A variety of techniques have been employed to deposit semiconductor coatings including sol-gel,[16] chemical vapour deposition (CVD),[17] spray pyrolysis [18] and physical vapour deposition (PVD) methods.[19] Among them, CVD is the quite common method to thin film, which can be used to deposit on small scale coatings, such as microelectronics and larger areas of growth, for example glass/steel coatings.[20,21] In recent years aerosol assisted CVD, a solution based variant of the conventional CVD process, has been increasingly utilized to fabricate high quality CVD products because it could provide a much wider choice and availability of precursors.[22] Thus, in this thesis, AACVD is the main technique concerned for materials fabrication. Certain sol-gel dip coating work has also been conducted since it is one of the widely accepted methods for large-scale architectural coatings.[23]

1.2 Aims and objectives

The aim of current work is to deposit high quality semiconducting thin films on glass substrates for energy efficient glazing and thin film solar cells applications by using

low-cost deposition techniques and chemical precursors together. The main objectives are:

1. To fabricate transparent conductive ZnO based thin films for use as energy efficient window coating via sol-gel dip coating and AACVD methods;
2. To synthesis highly surface-textured ZnO based thin films for use as front contacts in thin film solar cells via AACVD method;
3. To produce compact phase pure $MAPbI_3$ thin films for use as light absorber in perovskite solar cells via AACVD method.

1.3 Thesis structures

The thesis has been divided into 8 chapters and the respective summaries of each chapter are:

Chapter 1 gives brief background information on buildings energy consumption, the approaches and the materials for energy saving in buildings, followed by the aims and objectives of the project.

Chapter 2 is the literature review. It covers the background of thin film deposition technique, the fundamental of solar energy materials, and their applications in energy efficient glazing and thin film solar cells.

Chapter 3 presents the details of materials fabrication and characterization techniques used in this work.

Chapter 4 describes the deposition of gallium doped zinc oxide films on silica glass substrates by using sol-gel dip coating method utilising low-cost zinc acetate and gallium acetylacetonate as precursors. The effects of coating layers, heating temperatures and atmosphere on the ZnO:Ga film structural and opto-electronic properties were discussed.

Chapter 5 investigates the deposition of gallium doped zinc oxide films on silica glass substrates by using AACVD method utilising low-cost zinc and gallium acetylacetonates as precursors. The influence of doping content, deposition temperature and time on the ZnO:Ga film structural parameters and functional performances were discussed.

Chapter 6 probes the deposition of surface-textured zinc oxide films on FTO and silica glass substrates by using AACVD method utilising inexpensive precursors *i.e.* zinc-acetate-dihydrate, acetic acid and deionized water in methanol. The effect of acetic acid on ZnO nucleation and crystal growth behaviours was discussed.

Chapter 7 focuses on the deposition of compact phase pure methylammonium lead iodide films on FTO glass substrates using a novel two-step and three-step sequential AACVD method. The advantages of the multi-step deposition process over the single-step procedure were discussed.

Chapter 8 summarises the conclusions of all chapters and suggests the future research areas related to this work.

Chapter 2 Literature Review

2.1 Thin film production

Thin film deposition has led to many different approaches to the required goal. Sol-gel and chemical vapour deposition are two distinct groups of low-cost thin film growth techniques, which have been widely investigated and employed from laboratory-scale research to industry-scale production.

2.1.1 Sol-gel processing

Sol-gel is one of the most prevalent technologies for the production of thin films. It involves the generation of colloidal suspensions ("sols") that are subsequently converted into viscous gels and hence to solid materials.[24]

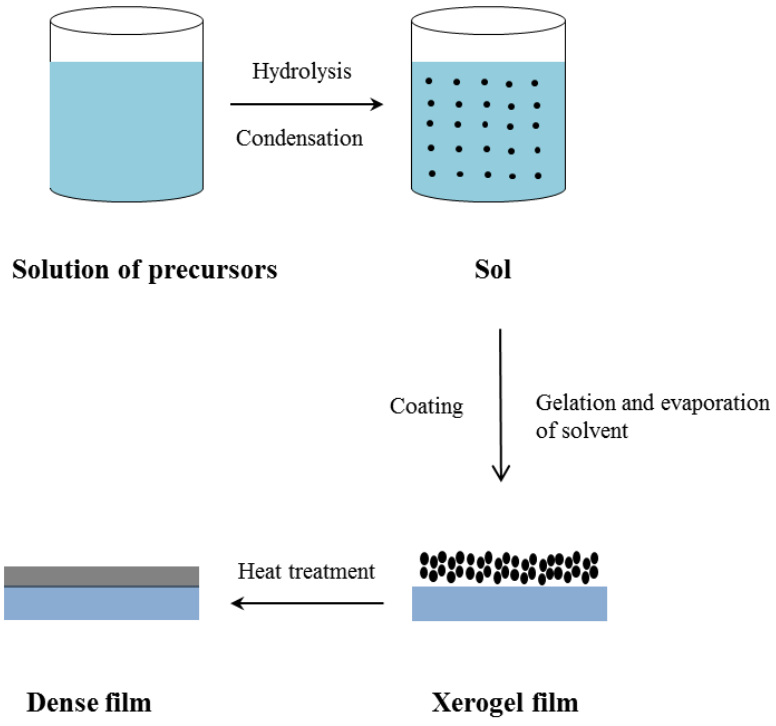

Figure 2.1 The schematic of thin film synthesis via sol-gel route.

Fig. 2.1 shows the schematic view of thin film synthesis from a colloidal sol. As observed, the molecular precursors (normally metal alkoxides or metal salts) in a homogeneous solution would undergo a succession of transformations (a) hydrolysis of the molecular precursor; (b) condensation by dehydration; (c) gelation by solvent evaporation; and (d) nucleation and grain growth to form dense films.[25]

2.1.1.1 Basic principles of sol-gel chemistry

The chemical aspects play an important role in studying and controlling the sol-gel process. The first step in a sol-gel reaction is the formation of an inorganic polymer by hydrolysis and condensation reaction. These reactions, taken the metal alkoxide precursors as an example, can be expressed as follow:[16,26,27]

(i) hydrolysis for the formation of reactive M-OH groups

$$M-OR+H_2O \rightarrow M-OH+R-OH \quad (2\text{-}1)$$

Where M refers to metal atom (M = Si, Ti, Al, *etc*.) and R is usually an alkyl group (R = CH_3, C_3H_5, C_3H_7, *etc*.).

(ii) condensation leading to the formation of bridging oxygen

$$M-OH+RO-M \rightarrow M-O-M+R-OH \quad (2\text{-}2)$$

or

$$M-OH+HO-M \rightarrow M-O-M+H_2O \quad (2\text{-}3)$$

2.1.1.2 Coating processes for depositing sol-gel films

Dip coating and spin coating are two main techniques adopted to coat sol-gels. The schematic view of the steps involved in dip coating and spin coating process are illustrated in Fig. 2.2.

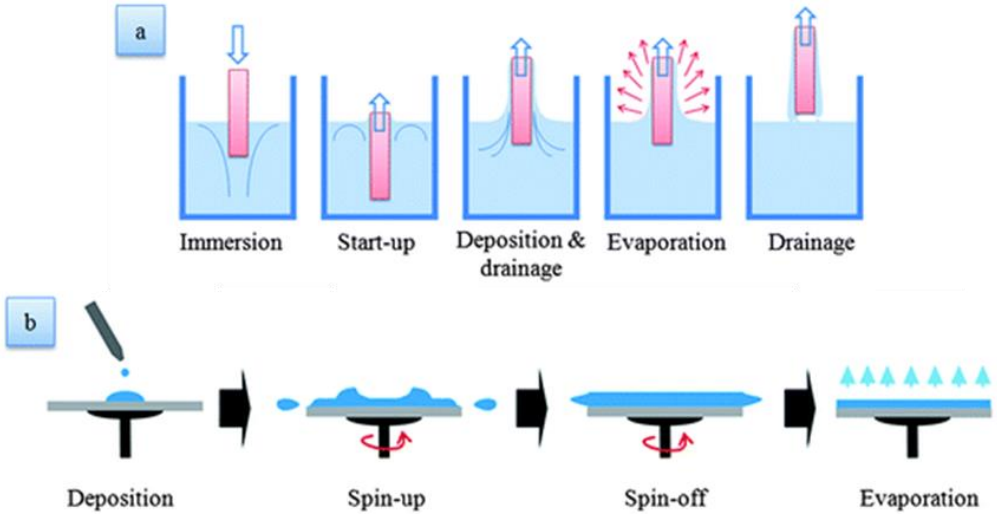

Figure 2.2 Steps involved in (a) dip coating and (b) spin coating.[28]

Dip coating

Dip coating is the most common and easiest way to deposit sol-gel film on a substrate. In this process, the substrate is dipped and withdrawn from the desired solution at a well-defined withdrawal speed under controlled temperature and atmospheric conditions. The substrates could be flat panels, cylinders or complex geometry and the coating areas could reach an order of square meters.[16,28]

The stages in the dip coating process can be divided into immersion, start-up, deposition, evaporation and drainage (see Fig. 2.2(a)). During the withdraw, the atmosphere controls the solvent evaporation and the subsequent destabilization of the

sols, leading to a gelation process and the formation of a transparent film due to the small particle size in the sols (nanometer range).[29] This gelation process is illustrated in Fig. 2.3.

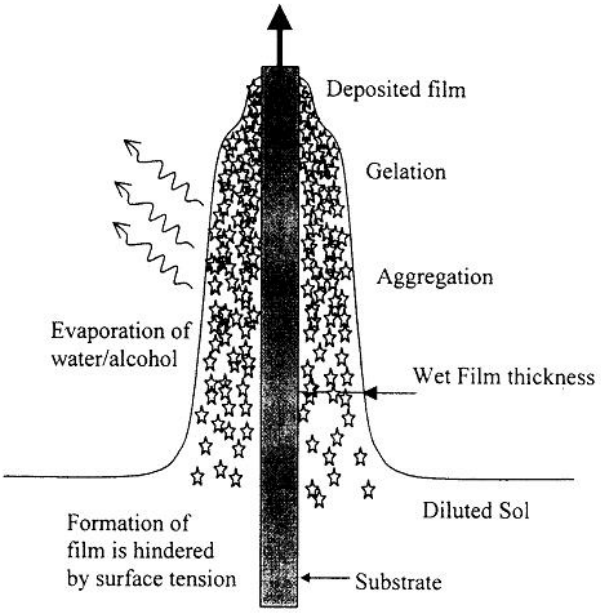

Figure 2.3 Gelation process during dip coating process obtained by evaporation of the solvent and subsequent destabilization of the sol.[29]

The resulting film thickness is mainly defined by the withdrawal speed, the solid content and the viscosity of the liquid. When the substrate speed and solution viscosity are low (often the case for sol-gel deposition), the coating layer thickness can be calculated by using Landau-Levich equation:[30]

$$d' = 0.94 \cdot \frac{(\eta' \cdot u')^{2/3}}{(\gamma')^{1/6}(\rho' \cdot g)^{1/2}} \tag{2-4}$$

Where d' is the coating thickness, η' is the viscosity of the coating solution, u' is the withdrawal speed, γ' is the liquid-vapour surface tension, ρ' is the density of the coating solution and g is the acceleration due to gravity.

Spin coating

Spin coating is a batch-production technique which produces thin films on flat or marginally curved substrates. It involves deposition of a small puddle of viscous film material and subsequent spinning of the substrate at high angular speed thereby forcing the puddle to spread owing to centripetal force (shown in Fig. 2.2(b)). The substrates used for this process is limited to a smaller size that can be held down steadily for spinning under high rotational speeds.[28]

2.1.1.3 Heat treatment for sol-gel films

The as-deposited amorphous xerogel film has to be densified by thermal treatment to form crystalline structures. For a multi-layer coated sample, the heat treatment is normally carried out into two steps. For the first step, a low temperature pre-heat treatment is applied after each coating for a short time (*i.e.* 10 mins), which aims to dry the gel film quickly before next coating procedure. In the second step, a high temperature annealing is employed for a longer period (*i.e.* 1 h) to obtain a well-crystallized films and fully decompose the organic by-products.[25] The final densification temperature depends on the film composition as well as the nature of the substrates.

Film crystallization

During the high temperature heat treatment, the nucleation, coarsening and coalescence phenomenon would occur in a sequence to reduce the system energy and form crystallized thin films.

Nucleation

According to the classical nucleation theory, the total free energy ΔG_r to form a spherical particle with a radius r comprises a contribution G_s to create the surface of the particle and a contribution ΔG_{int} which is due to the phase transformation inside the particle:

$$\Delta G_r = \Delta G_s + \Delta G_{\text{int}} = 4\pi r^2\gamma + \frac{4}{3}\pi r^2 \Delta G_v \tag{2-5}$$

From the relation $\partial(\Delta G_r)/\,\partial r = 0$, a free energy barrier, ΔG_c, which subcritical embryos must overcome to become supercritical nuclei, is given by equation (2-6):

$$\Delta G_c = \frac{16\pi\gamma^3}{3(\Delta G_v)^2} \tag{2-6}$$

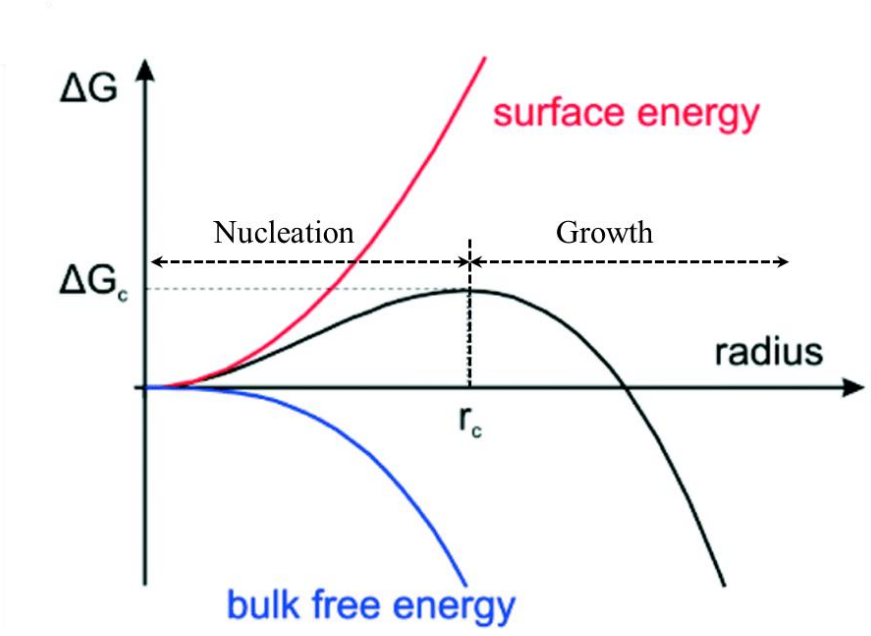

Figure 2.4 Nucleation and growth of a spherical particle.[31]

When the nucleus is formed on a flat substrate characterized by contact angle, θ, the reduced barrier, ΔG_c^*, can be derived as follows:

$$\Delta G_c^* = f(\theta)\Delta G_c \quad (2\text{-}7)$$

Where

$$f(\theta) = \frac{1}{4}(2 + \cos\theta)(1 - \cos\theta)^2 \quad (2\text{-}8)$$

and

$$\cos\theta = \frac{\gamma_s - \gamma_{sn}}{\gamma_n} \quad (2\text{-}9)$$

Where γ_s is the surface energy of the substrate, γ_n is the surface energy of the nucleus, and γ_{sn} is the interfacial energy between them.

Coarsening and coalescence

After nucleation, a coarsening process would simultaneously happen to reduce the amorphous material area and increase the size of the particles. Once these enlarged particles make contact, there is an energetic driving force for formation of a grain boundary that eliminates the free surface energies of the two contacting islands, in exchange for the lower energy of the newly formed grain boundary. This coalescence process normally would result into compact film with bigger grains, and may also lead to an evolution in the grain orientation distribution.[32]

Film structure and morphology

Due to the unique film thickening procedure, the nucleation and grain growth (coarsening and coalescence) processes in a sol-gel sample would proceed at the same time across the film. As a result, sol-gel derived coatings are often comprised by equiaxed fine grains. Fig. 2.5 shows the surface and cross-section images of a

typical sol-gel dip coated ZnO sample, where refined particles can be clearly observed.

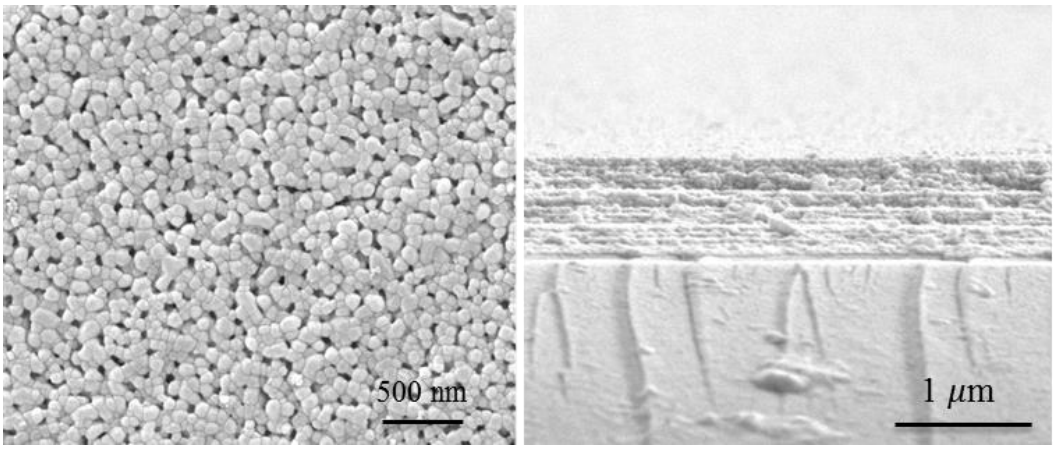

Figure 2.5 Surface and cross-section morphologies of a 15-layer dip coated ZnO film on silica glass substrate. (unpublished data from the author)

2.1.2 Chemical vapour deposition

CVD is a widely used process for the fabrication of thin film materials on a substrate, which involves the dissociation and/or chemical reactions of gaseous reactants in an activated (heat, light, plasma) environment, followed by the formation of a stable solid products.[22]

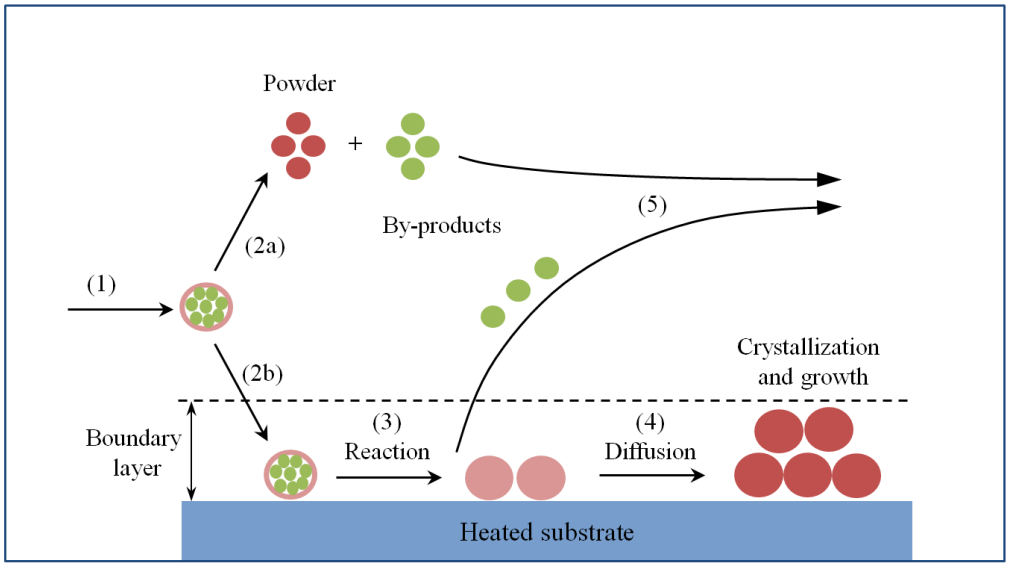

Figure 2.6 A schematic illustration of the CVD steps during deposition.[17]

The sequence of events taking place during a CVD reaction is shown in Fig. 2.6 and can be summarized as follows:[17]

1) Evaporation and transport of the gaseous species into the reaction chamber;
2) Gaseous reactants undergo gas phase reactions forming intermediate species:

a. When the temperature is above the decomposition temperatures of intermediate species, homogeneous gas phase reaction can occur where the intermediate species undergo decomposition and/or chemical reaction to form solid powder product. The powder that nucleated from the gas phase will deposit onto the substrate surface and interrupt the surface nucleation and growth, leading to a powdery coating with poor adhesion. The by-products in the gas phase are transported away from the deposition chamber.

b. When the temperature is below the intermediate phase dissociation temperature, diffusion or convection of the intermediate species across the

boundary layer occurs. These intermediate species subsequently undergo steps (3) to (5).

3) Absorption of gaseous reactants onto the heated substrate, and then the heterogeneous reaction occurs, which produces the deposit (*i.e.* mobile atoms) and by-product species.
4) The mobile atoms will diffuse to the preferred sites on the heated substrate surface to form crystallisation centre. Growth will occur by the addition of adsorbed monomers to sites with lowest free energy to form crystallites.
5) The unreacted gaseous precursors and by-products will be transported away from the deposition chamber.

2.1.2.1 Thermodynamics and reaction kinetics in CVD

A CVD reaction is governed by both the thermodynamics and the kinetics. The former is the driving force which indicates the direction of the reaction is going to proceed, and the latter defines the transport process and determines the rate-control mechanism.[33]

Reaction feasibility

The first step of a theoretical analysis is to ensure that the desired CVD reaction will take place. This feasibility can be determined by calculating the Gibbs free energy ΔG_r of the reaction under the given temperature and pressure using the following equations:[17,33]

$$\Delta G_{\mathrm{r}} = \Delta G_{\mathrm{f}}(\mathrm{products}) - \Delta G_{\mathrm{f}}(\mathrm{reactans}) \quad (2\text{-}10)$$

and

$$\Delta G_{\mathrm{f}}(\mathrm{T}) = \Delta H_{\mathrm{f}}^{\mathrm{o}}(298) + \int_{298}^{T} C_{\mathrm{p}}\mathrm{d}T - TS^{\mathrm{o}}(298) - \int_{298}^{T}(C_{\mathrm{p}}/\mathrm{T})\mathrm{d}T \quad (2\text{-}11)$$

Where ΔG_{f} is the free energy of formation for the individual species of the reactants and the products, $\Delta H_{\mathrm{f}}^{\mathrm{o}}$ and S^{o} are standard enthalpy of formation and entropy at 298 K, respectively, and C_{p} is heat capacity.

Fluid dynamics and boundary layer

The transport phenomena within a CVD reactor are influenced by the complex reactor geometry and large thermal gradient characteristics. Basic fluid mechanics concepts can be applied to CVD to describe the fluid dynamic and mass transfer in the gas phase. The fluid flow in a CVD process can be characterised by Reynolds number (R_{e}) from equation (2-12):[17]

$$R_{\mathrm{e}} = \frac{\rho^{*} UL}{\mu^{*}} \quad (2\text{-}12)$$

Where ρ^{*} is the gas mass density, μ^{*} is the gas viscosity, U is the gas velocity, and L is the characteristic length.

It is empirically found that R_{e} of order 1 corresponds to simple laminar flows; Reynolds of 10's to a few hundred give rise to various sorts of stable re-circulations. R_{e} of some thousands to tens of thousands is usually associated with complex, turbulent flows. Most CVD reactors operate in the laminar regime, since turbulent flows are not conducive to good reproducibility and process control.[34]

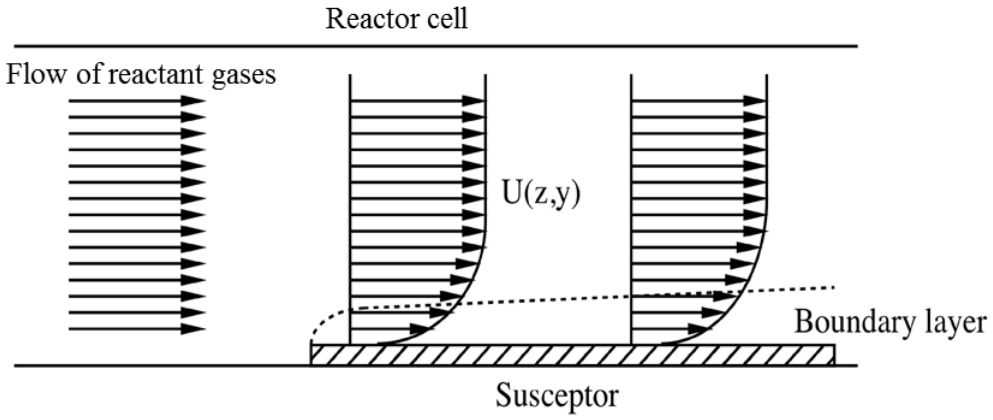

Figure 2.7 Boundary layer in a horizontal CVD reactor.[35]

In the case of laminar flow, the gas velocity of at the beginning of deposition surface is zero. The boundary is defined as the region in which the flow velocity changes from zero at the substrate surface to essentially that of the bulk gas away from the wall. This boundary layer starts at the inlet of the tube and increases in thickness until the flow becomes stabilized, as shown in Fig. 2.7. The reactant gases flowing above the boundary layer have to diffuse through this layer to reach the deposition surface. The thickness of boundary layer, Δ, can be calculated from equation (2-13):

$$\Delta = \sqrt{\frac{x}{R_e}} \tag{2-13}$$

Where x is the distance from inlet in flow direction. This equation shows that the thickness of boundary layer enhances with lower gas-flow velocity and with increased distance from the tube inlet. In real production, the substrate within a CVD reactor can be titled to partially compensate for the increasing boundary-layer thickness.

Reaction rate and rate-limiting steps

In traditional thermal CVD, the film growth rate is governed by several parameters, such as the substrate temperature, the reactor pressure and the composition and chemistry of the gas-phase.[21] The temperature dependent CVD film growth rate, for example, is illustrated in Fig. 2.8.

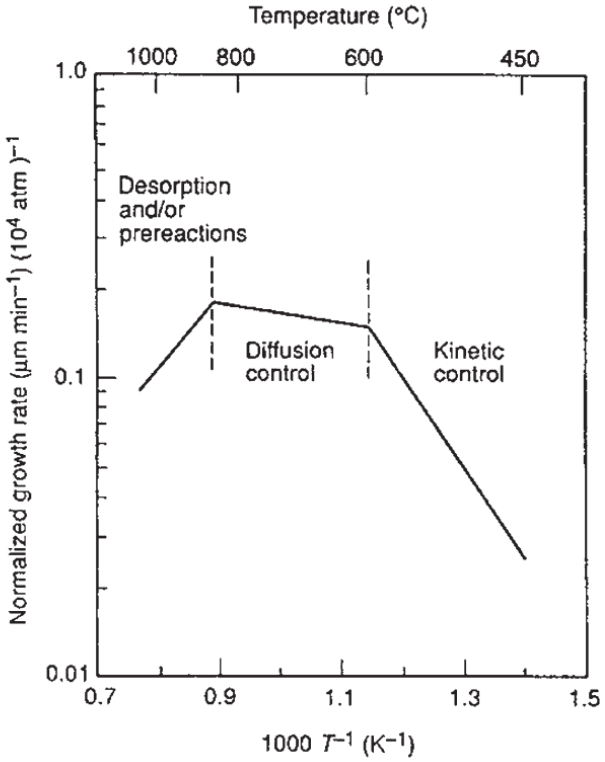

Figure 2.8 The Arrhenius plot of CVD GaAs coating.[21]

It is seen that, at lower growth temperature, the film growth rate increases rapidly with the substrate temperature. This represents the rate-limiting mechanism is surface chemical kinetics and this region is generally termed the region of kinetic growth control. The film growth rate increases exponentially with substrate temperature according to the Arrhenius equation:

$$\text{Growth rate} \propto \exp(-E_A/RT) \quad (2\text{-}14)$$

Where E_A is the apparent activation energy, R is the gas constant and T is the temperature.

As the temperature increases, the growth rate becomes nearly independently of temperature. This is because the reactions occur rapidly at high temperatures, whereby any molecule that reaches the surface would react instantly. Therefore, the reaction rate is controlled by the mass transport of reagents through the boundary layer to the growth surface, and this is termed the region of mass transport or diffusion-controlled growth.

At even higher temperatures, the growth rate tends to decrease. This may relate to the increased desorption of film precursors into the gas phase, which interrupt the growth of coatings and hence the microstructure purity and adhesion.

To summarize the surface reaction rate is the limiting step at lower temperature and diffusion is the rate limiting step at higher temperature. It is possible to switch from one rate-limiting step to the other by changing the temperature.

2.1.2.2 Thin film growth in CVD

The CVD thin film growth process can be divided into 1) nucleation, coarsening, coalescence and 2) structure evolution during film thickening, which are all related to the packing behaviours of the incoming atoms (or film growth model).

Film growth model

CVD thin films are deposited following three types of growth model: the layer by layer growth (Frank-van der Merwe), the island growth (Volmer-Webber) and the mixed growth (Stranski-Krastanov).[36] The predominance of one type of growth over another is explained by the surface energy. If the substrate-vapour surface energy is larger than the total surface energy of film-substrate and film-vapour, the film will wet the surface to lower the system energy and a layered growth would occur. If the total surface energy of the film interfaces is larger than that of the substrate-vapour interface, the material would ball up to minimize interface with the substrate and uneven islands are formed. In the mixed type, the growth is initially produced layer by layer but then changes into island growth after a few monolayers. The three different film growth types are schematically illustrated in Fig. 2.9.

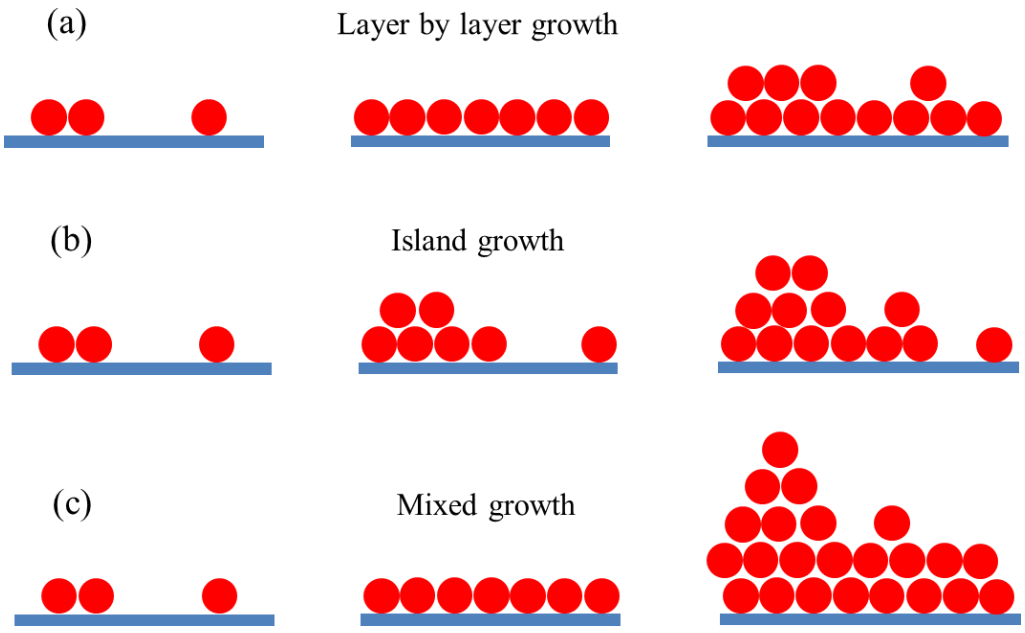

Figure 2.9 CVD film growth types: (a) layer by layer growth, (b) island growth and (c) mixed growth.

Film structure and morphology

Films produced from CVD processes exhibit four main types of structures (see Fig. 2.10): (a) columnar grains with domelike tops, (b) faceted columnar grains, (c) symmetric fine grains and (d) single-crystalline grains (epitaxial growth). The predominance of one structure over another is governed by the thermodynamics and kinetics of the system, which are controlled by the deposition conditions. Fine-grained structures can be produced under low pressure and/or temperatures conditions, where the diffusion of reactants through the boundary layer is limited. At high temperatures, deposits tend to be columnar as a result of continuous grain growth toward the reactant source.

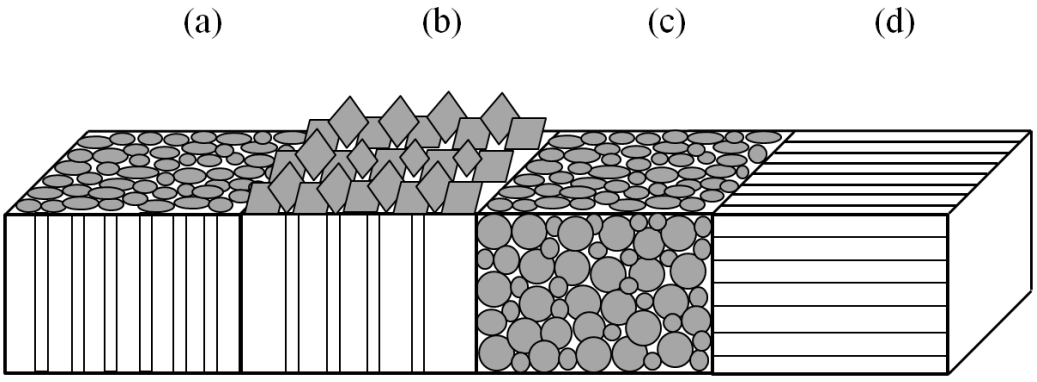

Figure 2.10 Schematic of structures obtained by CVD: (a) columnar grains with domed topes, (b) faceted columnar grains, (c) symmetric fine grains, (d) single-crystalline grains.

The columnar grain structures, which are developed during the film thickening process, are favourable for materials that require high electrical conductivity. This structure could develop in two different ways, as illustrated in Fig. 2.11.

If the grain boundaries formed through island impingement are immobile, the grain structure resulting from the nucleation, growth, and coalescence processes is retained at the base of the film. Subsequent thickening occurs though epitaxial growth on these grains and columnar grain structures develop in which the in-plane grain size becomes small compared with the grain size as measured in the film thickening direction. Since the grains at the base of the film grow into the parent phase, competitive growth processes lead to an increasing in-plane grain size at the top of film surface.

If grain boundaries are mobile, the grain structure of a film evolves during the coalescence process and continues to evolve during film thickening. This often results in a more equiaxed structure in which the in-plane grain size tends to be approximately the same as the scale with the film thickness. The average in-plane grain size is therefore uniform across the film.

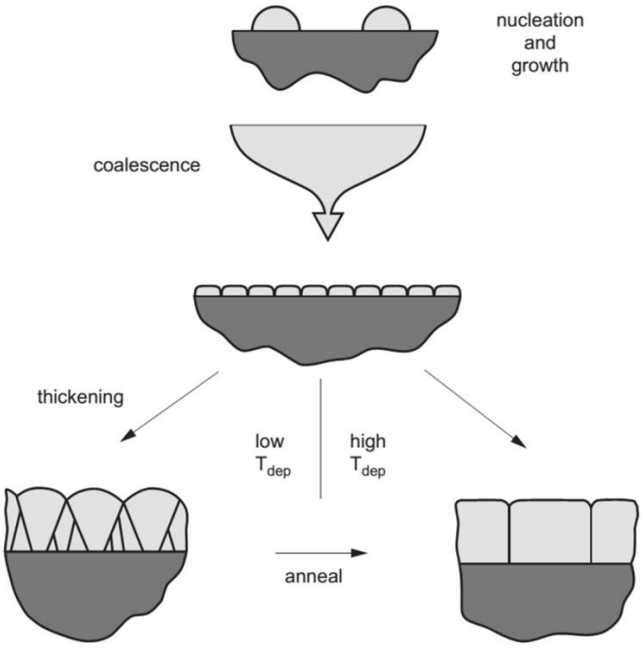

Figure 2.11 Overview of grain structure evolution during CVD of polycrystalline films.[32]

In addition to the grain structures, the surface morphology of a film is also essential to its physical characteristics and usefulness. The layer morphology is determined by surface diffusion and nucleation processes during deposition, which in turn are significantly influenced by CVD process parameters such as growth temperature, partial pressures of gaseous species and the total pressure of the system.

2.1.2.3 Aerosol assisted chemical vapour deposition

CVD has gone through wide-ranging developments over the decades. Some commonly-used variations of CVD are metal-organic CVD (MOCVD), plasma enhanced CVD (PECVD), atmospheric pressure CVD (APCVD), LPCVD and ultrahigh vacuum CVD (UHVCVD).[33] In recent years, the CVD process based on the use of aerosol precursors known as AACVD has attracted wide attention.[22]

AACVD involves the atomization of a liquid precursor solution into fine sub-micrometer-sized aerosol droplets that are distributed throughout a gaseous medium. The aerosol is subsequently transported to the CVD reactor, where the solvent undergoes rapid evaporation once reaches the substrate. Then desired products can be synthesized via decomposition or other chemical reactions of the vaporized precursor.[22,37] A schematic diagram of AACVD is shown in Fig. 2.12. In this modified CVD system, the chemical precursors need not necessarily be volatile, but merely soluble in any solvent from which an aerosol is generated.[37] As a result, many involatile chemicals, such as metal acetate or acetylacetone, can be readily utilized to fabricate CVD products. Also the precursor delivery stage is much

simplified since different chemical source can be transported through a single line instead of separately, thus potentially reducing set-up and maintenance costs.[5,38]

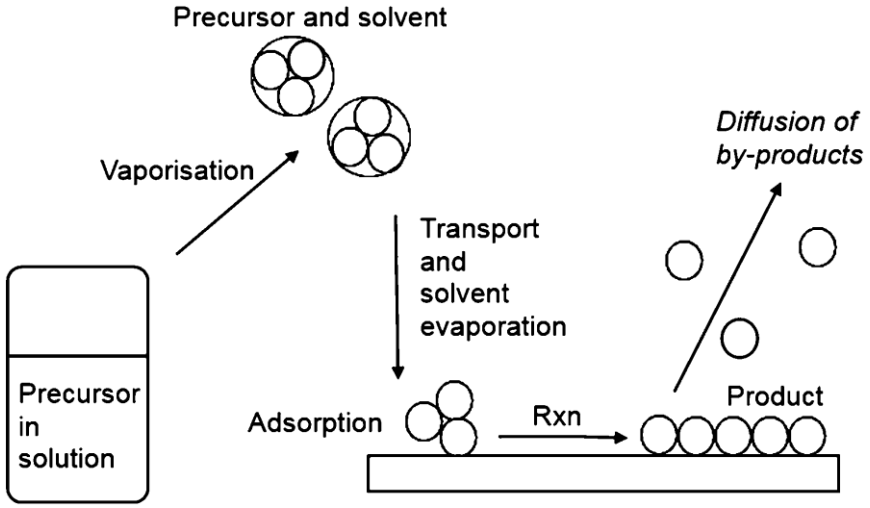

Figure 2.12 The schematic illustration of the process involved in AACVD.[22]

Specifically, the aerosol entering the reaction chamber would undergo four different processes depending on the substrate temperature, which are illustrated in Fig. 2.13.

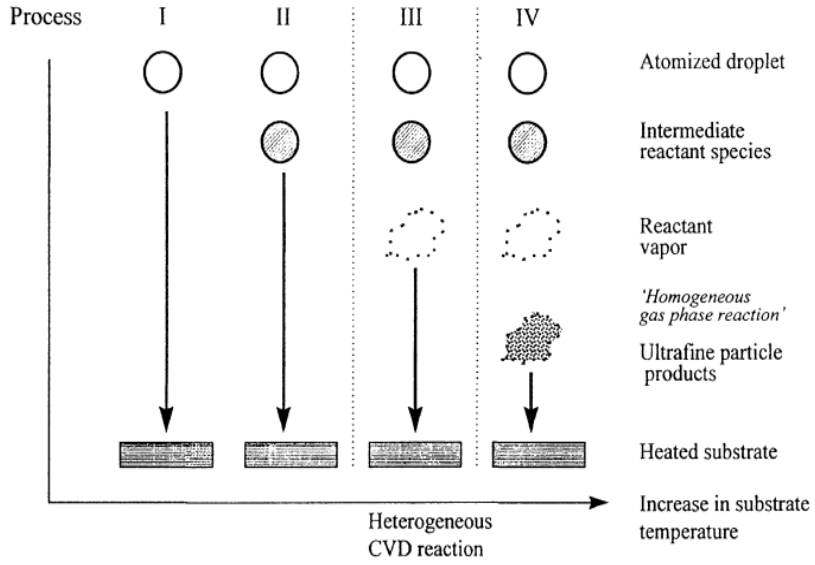

Figure 2.13 Influence of the temperature of the aerosol assisted deposition process.[17]

I. The aerosol precursor droplets are sprayed directly onto a heated substrate, followed by the removal of the solvent through evaporation and decomposition of the precursor to the finished product;

II. The solvent is evaporated prior to arriving onto the substrate surface, and the precursor precipitated is subsequently deposited onto the heated substrate and decomposed and/or undergoes chemical reactions to yield the desired materials;

III. The solvent is evaporated while approaching the substrate surface, and the precursor precipitate subsequently undergoes volatilisation near the vicinity of the substrate surface and adsorption of the vapour onto the heated substrate surface, followed by the decomposition and/or chemical reactions to yield dense films with excellent adhesion;

IV. At very high the deposition temperature, the decomposition and/or chemical reaction occur in the vapour phase, leading to homogeneous nucleation and formation of stable fine particles in the gas phase. The particles are then sintered on the heated substrate, resulting into the formation of porous films with poor adhesion.

2.1.3 Other deposition methods

In addition to the sol-gel and CVD techniques discussed, many other deposition methods, such as physical vapour deposition and spray pyrolysis, have been utilized to fabricate thin film materials. Obviously each methodology has its own advantages and disadvantages.

2.1.3.1 Physical vapour deposition

Physical vapour deposition processes are atomistic deposition processes in which material is vaporized from a solid or liquid source in the form of atoms or molecules and transported in the form of a vapour through a vacuum or low pressure gaseous (or plasma) environment to the substrate, where it condense. PVD processes are used to deposit films with thicknesses in the range of a few nanometres to thousands of nanometres.[19] Films produced from PVD normally exhibit higher purity and better-controlled composition, but this process requires high equipment investment and also suffers from the relatively low production rates.[39]

2.1.3.2 Spray pyrolysis

In spray pyrolysis, a solution of metal complexes is sprayed directly or via aerosol formation onto the substrate. Complicated reactions between precursors and molecules of the solution occur finally before forming the deposit. Spray pyrolysis is a low-cost thin film deposition technique but the resulting films have been found to be less consistent.[39,40] It is noteworthy that the borderline between spray pyrolysis and aerosol CVD is not strictly defined. From my understanding, AACVD is more controllable than the spray technique for large area coating because it can be readily incorporated into the existing commercial CVD systems.

In conclusion, to choose a deposition method for a specific thin film material, the quality, manufacture cost and lifetime of the resulting coatings should all be taken into account.

2.2 Fundamentals for solar energy materials

Solar energy materials work on the basis of controlling the flow (absorption, transmission and reflection) of ambient radiation in our environment.

2.2.1 Blackbody radiation and solar spectrum

The most fundamental property of ambient radiation stems from the fact that all matter sends out electromagnetic radiation. This leads to the concept of an ideal blackbody (an opaque and non-reflective body), whose emitted spectrum can be described through Planck's radiation law as a function of body temperature:[41]

$$E(\lambda, T) = \frac{2hc^2}{\lambda^5} \cdot \frac{1}{e^{hc/\lambda kT} - 1} \tag{2-15}$$

Where h is the Planck's constant, k is the Boltzmann's constant, c is the speed of light, λ is the wavelength, T is the body temperature.

The wavelength for which the maximum radiation intensity is reached can be determined by Wien's displacement law:[42]

$$\lambda_{max} T = 2.898 \cdot 10^{-3} \tag{2-16}$$

Fig. 2.14(a) depicts the blackbody radiation spectra for four temperatures from -50 ℃ to 100 ℃. These radiations could come from every object around us, *i.e.* hot tea or cold ice cream, and their spectra are confined to 2-100 μm. The peak in the spectrum is displaced toward shorter wavelength with increasing temperature, as explained by equation (2-16).

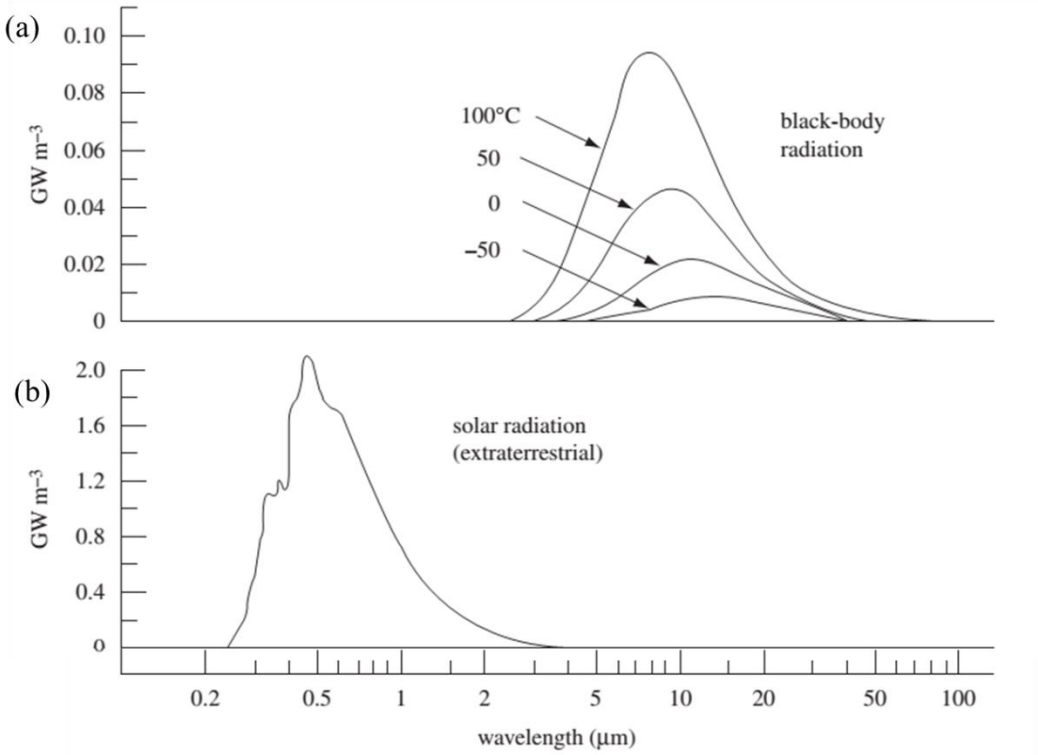

Figure 2.14 Spectra showing (a) black-body radiation for four different temperatures, (b) solar radiation outside the earth's atmosphere.[43]

Fig. 2.14(b) shows the solar radiation spectrum reaching the surface of the earth. The spectrum lies in the range of 0.25-3 μm, making it is possible to have surfaces with entirely different properties with regard to blackbody and solar radiation. The solar spectrum is often divided into three wavelength intervals:[44]

1. 300 nm < λ < 380 nm: the ultraviolet radiation (UV) carries about 7 % of the solar energy;
2. 380 nm < λ < 780 nm: the visible light (Vis) has about 53 % of the solar energy;
3. 780 nm < λ < 2500 nm: the near infrared radiation (NIR) carries about 40 % of the solar energy.

2.2.2 Absorbance, transmittance and reflectance

When electromagnetic radiation impinges on a material one fraction can be transmitted, a second fraction is reflected, and a third fraction is absorbed. Energy conservation yields, at each wavelength, that:

$$A(\lambda) + R(\lambda) + T(\lambda) = 1 \quad (2\text{-}17)$$

Where T, R, and A denote transmittance, reflectance, and absorptance, respectively.

Depending on the applications, it is possible to selectively transmit/reflect/absorb the solar radiation by use of appropriate solar energy materials. In the next two sections, two distinct types of solar energy materials, transparent conducting oxides and organometallic halide, will be introduced.

2.2.3 Transparent conducting oxides

Transparent conducting oxides are a unique class of solar energy materials based on metal oxides that exhibit both optical transparency and electrical conductivity simultaneously.[45] The most widely used TCO material is ITO, but due to the scarcity of indium, the development of alternative materials has attracted great attention.[46] Among them, zinc oxide has been extensively studied and regarded as the new generation of low-cost TCO materials.

2.2.3.1 Zinc oxide

As a direct and large-band-gap material, ZnO is emerging as a material of interest for a variety of electronic and optoelectronic applications.[47]

Crystallographic structure

Zinc oxide is a compound semiconductor which crystallizes in the hexagonal wurtzite structure. The structure can be simply described as a number of alternating planes composed of tetrahedrally coordinated O^{2-} and Zn^{2+} ions, stacked alternately along the *c*-axis, as shown in Fig. 2.15(a).[48]

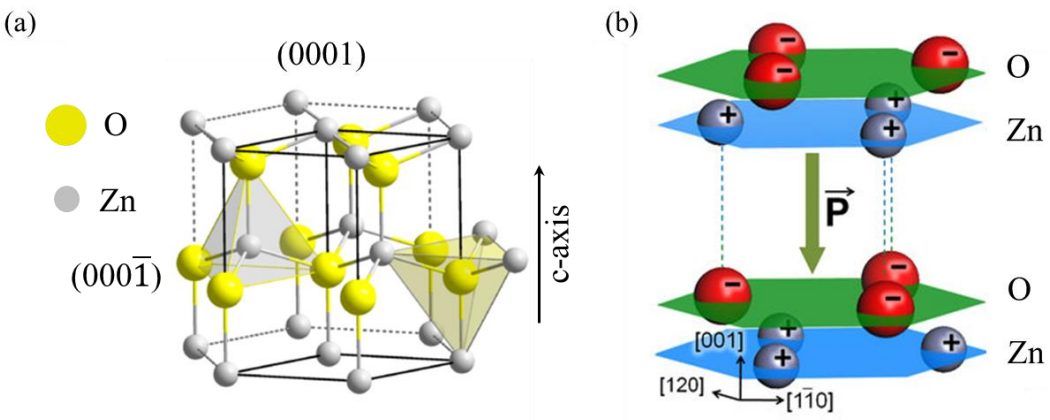

Figure 2.15 (a) The wurtzite structure model of ZnO.[49] **(b) ZnO has a noncentrosymmetric crystal structure that is made up of alternate layers of positive and negative ions, leading to spontaneous polarization.**[50]

Another important characteristic of ZnO is polar surfaces. The oppositely charged ions produce positively charged Zn-(0001) and negatively charged O-(000$\bar{1}$) surfaces, resulting in a normal dipole moment and spontaneous polarization along the *c*-axis as well as a divergence in surface energy (see Fig. 2.15(b)).[48] The other two most commonly observed facets for ZnO are {10$\bar{1}$0} and {10$\bar{1}$1}, which is nonpolar and semipolar surface, respectively, and have lower energy than the {0001} facets.[51]

Band structure

Zinc oxide is a direct semiconductor with a band gap of 3.4 eV.[45] The band structure of ZnO has been calculated by density-functional theory (DFT) models and a typical band structure is shown in Fig. 2.16. It is seen that the calculated band structures confirm the experiment in that the valence band maximum and the conduction band minimum both occur at the Γ point k = 0, which means that ZnO is a direct semiconductor.[45]

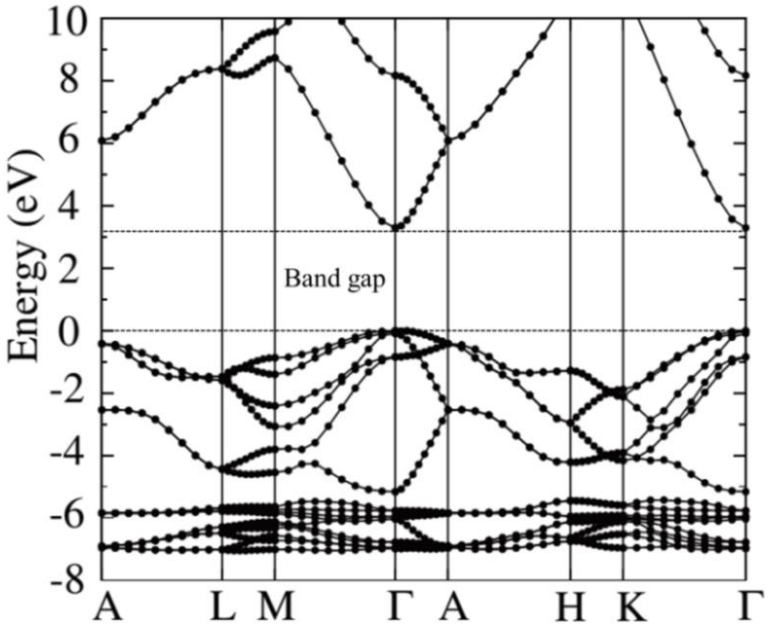

Figure 2.16 The calculated band structure of ZnO.[52]

Electrical conductivity and doping

The electrical conductivity (σ) of a material is normally evaluated by its sheet resistance (R_S) or resistivity (ρ). Their relationship is expressed as follow:

$$\sigma = 1/\rho = 1/R_s t \qquad (2\text{-}18)$$

Where *t* is the thickness of the sample.

The sheet resistance of a semiconductor thin film can be measured by use of four-point probe technique. But in order to obtain more specific electric property information, such as identify the type of the semiconductor and the number of the charge carriers, a Hall Effect study is usually required. The resistivity is then determined by the carrier density (N) and carrier mobility (μ) from equation (2-19):

$$\rho = 1/Ne\mu \qquad (2\text{-}19)$$

Where *e* is the electron charge.

As an n-type semiconductor, intrinsic ZnO is relatively resistive at room temperature, with resistivity varies in the order of 0.1-10^3 Ω cm depending on the preparation conditions.[45] To meet the electric requirement in various opto-electronic applications (see Fig. 2.17), ZnO film conductivity needs to be largely improved and this can be fulfilled by two approaches:

- Generation of intrinsic donors by lattice defects (*i.e.* oxygen vacancies or interstitial zinc atoms);
- Introduction of extrinsic dopants (either metal with oxidation number three on substitutional metal lattice sites or halogens with oxidation number minus one on oxygen lattice sites).[45,52]

Figure 2.17 Sheet resistance range required for transparent conducting materials in various opto-electronic application.[53]

Intrinsic doping of ZnO

The first possibility for intrinsic doping in ZnO can be realized during the deposition by carefully adjusting oxygen partial pressure and deposition rate. The other more common way is partial reduction of the oxide film after deposition, for instance by annealing in vacuum or in a hydrogen containing atmosphere. The ZnO film resistivity after intrinsic doping could reduce to 10^{-2} to 10^{-3} Ω cm.[45]

Extrinsic doing of ZnO

In order to lower the ZnO film resistivity value to a range of 10^{-4} Ω cm or even 10^{-5} Ω cm, extrinsic doping is an important and indispensable route. The group-III elements B, Al, Ga and In are the most common dopant in ZnO, which act as shallow donors when substituted on the Zn sites. The extra valence electron of these impurities is loosely bound and occupies effective-mass states near the conduction

band minimum at low temperatures. As the temperature rises this extra electron is excited to the conduction and is free to move.[52] The schematic of this phenomenon is illustrated in Fig. 2.18.

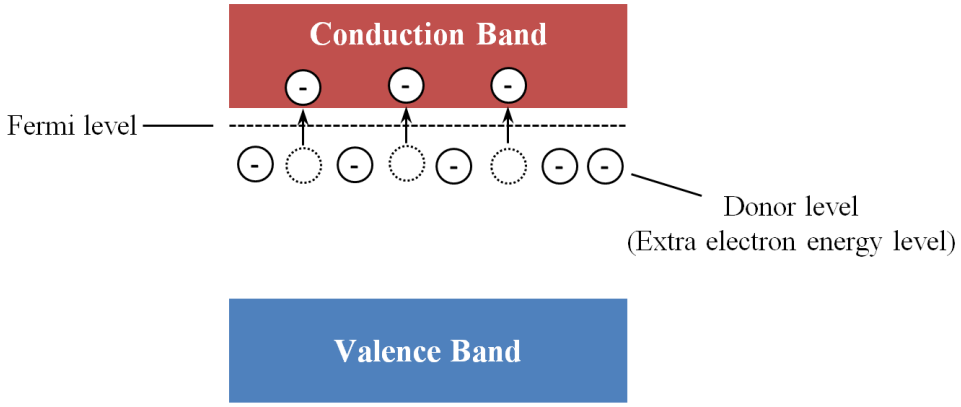

Figure 2.18 Zinc oxide doped with a group-III element results in a new filled level near the conduction band.

The conductivity of ZnO films can be tremendously improved after doping with group-III elements, as shown in Table 2.1. It is worth mentioning that, among these impurities, gallium is regarded as a better choice because its ionic and covalent radii (0.62, 1.26 Å) is closer to those of zinc (0.74, 1.31 Å) than to those of aluminium (0.5, 1.26 Å) or indium (0.81, 1.44 Å), so the lattice distortion under a high doping input can be minimized.[54,55] In addition, Ga is relatively oxidation resistant, so the formation of non-conductive gallium oxide in ZnO can be suppressed.[56]

Table 2.1 Electrical properties of group-III elements doped ZnO films produced by CVD techniques.

Element	Carrier concentration	Carrier mobility	Resistivity	Sheet resistance	Fabrication method
	[cm^{-3}]	[$cm^2 V^{-1}s^{-1}$]	[Ω cm]	[Ω sq^{-1}]	
B	1.5×10^{20}	10.6	1.4×10^{-3}	10	MOCVD [57]
Al	7.8×10^{20}	18.1	4.5×10^{-4}	6.4	APCVD [58]
Ga	10.6×10^{20}	24.6	2.4×10^{-4}	3.6	APCVD [59]
In	9.0×10^{20}	8	1.2×10^{-3}	-	APCVD [60]

Carrier transport in ZnO

The movement of charge carriers within crystalline semiconducting materials is controlled by a variety of electrical scattering mechanisms. In doped ZnO, the carrier mobility is mainly determined by the ionized impurity scattering, neutral impurity scattering and grain boundary scattering effect.[61] The schematic view of electrons scattered by impurities and grain boundaries is shown in Fig. 2.19.

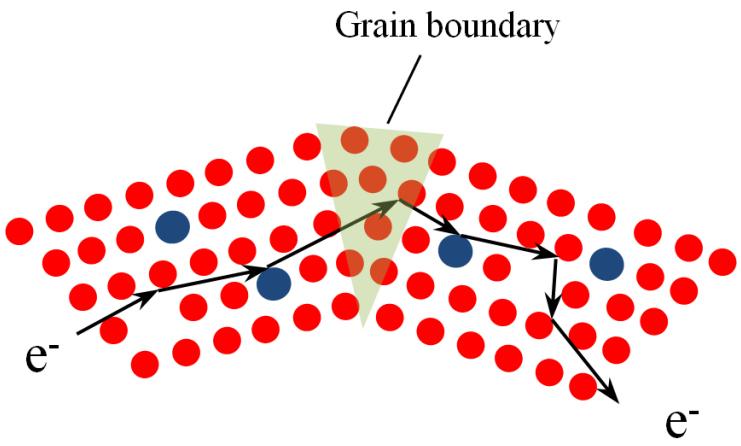

Figure 2.19 Schematic of electron scattering from impurities and grain boundaries.

Among all the impurities in the crystal, the greatest effect on the scattering of the carriers is produced by ionized impurities. This is because the electrostatic field due

to such impurities remains effective even at a great distance.[39] The mobility due to ionized impurity scattering can be given by equation (2-20):[62]

$$\mu_{\mathrm{IIS}} = \frac{4e}{h}\left(\frac{\pi}{3}\right)^{1/3} N_{\mathrm{I}}^{-2/3} \tag{2-20}$$

Where N_{I} is the concentration of ionized impurities.

The scattering of carriers by a neutral impurity atom in the crystal lattice is similar to the scattering of slow electrons by hydrogen atoms. The mobility due to neutral impurity scattering is given by Erginsoy formula:[62]

$$\mu_{\mathrm{N}} = \frac{m^* e^3}{20\hbar^3 \varepsilon_{\mathrm{o}} \varepsilon_{\mathrm{s}} N_{\mathrm{n}}} \tag{2-21}$$

Where m^* is the effective mass of the charge carriers, $\hbar$ is the reduced Planck's constant which equals to $h/2\pi$, ε_{o} is the permittivity of free space, ε_{s} is the permittivity of the semiconductor, and N_{n} is the concentration of neutral impurities.

Polycrystalline films exhibit a vast amount of grain boundaries. These grain boundaries generally contain high densities of interface states, which trap free carriers from the bulk of the grain and scatter carriers by virtue of the inherent disorders and the presence of trapped charges, resulting in a charge depletion region on both sides of grain barriers. An energetic barrier (Φ_{b}) is then formed and it is related to the carrier density both in the bulk of grains (N) and in the grain boundaries (N_{g}):[45]

$$\Phi_{\mathrm{b}} = kT\ln\left(\frac{N}{N_{\mathrm{g}}}\right) \tag{2-22}$$

and the grain boundary limited mobility is given by equation (2-23):

$$\mu_{\mathrm{G}} = el(2\pi m^{*}kT)^{-1/2}\exp(\frac{-e\Phi_{\mathrm{b}}}{kT}) \quad (2\text{-}23)$$

Where *l* is the grain size.

The overall carrier mobility in doped ZnO thin films therefore can be written as:

$$\frac{1}{\mu} = \frac{1}{\mu_{\mathrm{IIS}}} + \frac{1}{\mu_{\mathrm{N}}} + \frac{1}{\mu_{\mathrm{G}}} \quad (2\text{-}24)$$

It is noteworthy that, for high carrier densities (N > 10^{20} cm^{-3}), additional tunnelling through the barriers can take place, which increases the current flow between the ZnO grains.[45] In this case, the grain boundary scattering effect become less profound compared to the ionized and neutral impurity scattering.

Optical properties

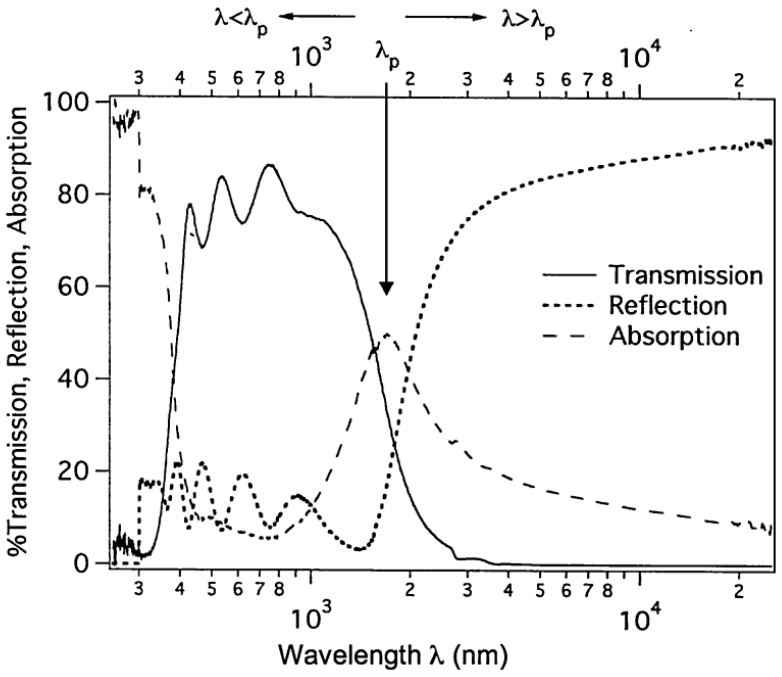

Figure 2.20 Transmission, reflection, and absorption spectra of a typical TCO film.[63]

The optical performance of doped ZnO films is similar with other TCO materials. Fig. 2.20 shows the optical spectra of a typical TCO film. In addition to its good

visible transparency, a decrease in transmission and increase in reflection can be observed at longer wavelengths (> 1500 nm). This transition, corresponding to a maximum in absorption, is referred to as the plasma wavelength (λ_p), where the frequency of the light is the same as the frequency of the collective oscillation of electrons in the material. The electrons oscillating in phase with the electric field component of the light result in absorption. When $\lambda < \lambda_p$ the wavefunction is oscillatory and radiation can propagate, resulting in a transparent material. When $\lambda > \lambda_p$ the wavefunction decays and no radiation can propagate, resulting in reflection.[63] The resonance wavelength is primarily influenced by the electron concentration according to the Drude theory:[39]

$$\lambda_p \propto (1/N)^{1/2} \quad (2\text{-}25)$$

Thus, the plasma wavelength in TCO materials can be tuned by control of doping to meet different optical requirements.

In the solar UV radiation region (300-380 nm), the TCO film transmission drops sharply due to the onset of fundamental absorption by an interband transition.[64] The absorption edge is related to the film band-gap energy, which can be determined by constructing Tauc plots using the $(ahv)^2$ relation:[65,66]

$$(\alpha h\nu) \propto (h\nu - E_g)^{1/2} \quad (2\text{-}26)$$

Where

$$\alpha = 2.302A/t \quad (2\text{-}27)$$

Where α is the absorption coefficient, hv is the photon energy, E_g is the bandgap, A is the film absorbance and t is film thickness.

2.2.4 Organometallic halide

As a new type of solar energy materials, organometallic halide has been extensively investigated as the light absorber in solar cells since 2009. Within a span of six years, the certified power conversion efficiency of organometallic halide based perovskite solar cells has rapidly increased from 3.8 % to 21.0 %, and further efforts are being made to push this value toward and beyond that of crystalline silicon (25 %).[13,67,68]

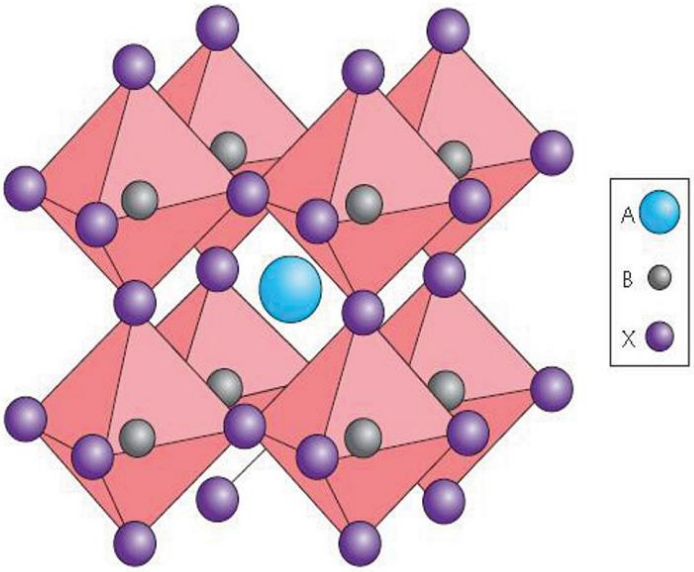

Figure 2.21 Unit cell of basic ABX_3 perovskite structure.[69]

Perovskites are a large family of compounds that share the same chemical formula ABX_3. 'A' and 'B' denote cations, where A is much larger than B, and 'X' an anion (shown in Fig. 2.21).[70] The organometallic halide perovskites offer the chemical

and structural diversity that can be obtained by 1) mixing in various halides (Br or Cl), 2) replacing the methylammonium with other organic species (*i.e.* formamidium) or inorganic constitutions (*i.e.* caesium), and 3) substituting the lead citations with tin. As a result, their band gaps, crystalline phase transitions, and hole-electron diffusion lengths can all be tuned.[71–73] The band gap tuning in organolead halide perovskites, taken as an example, is illustrated in Fig. 2.22.

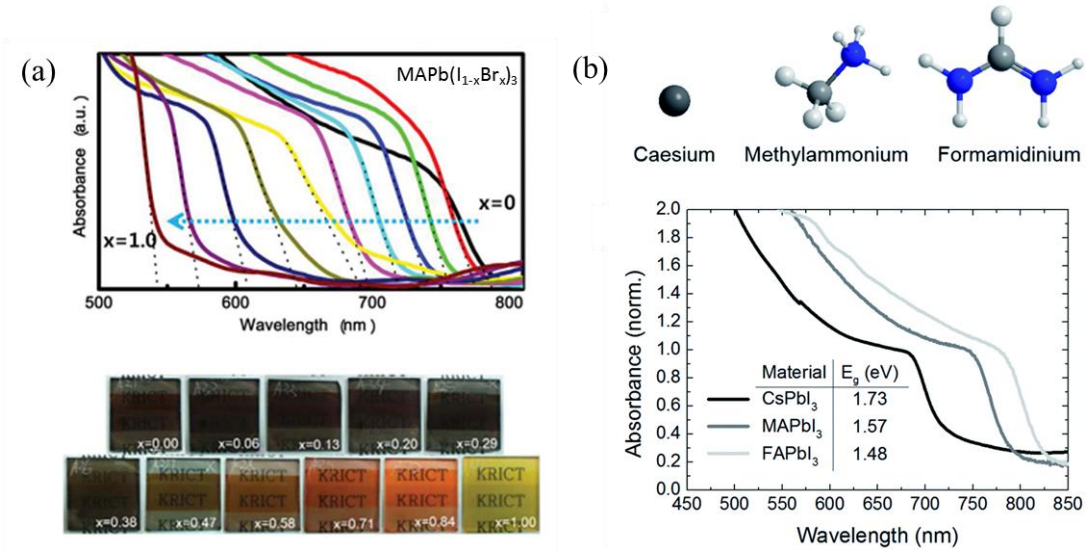

Figure 2.22 Tubing perovskite band gap by (a) mixing halides and (b) replacing A cation.[72,74]

2.2.4.1 Methylammonium lead iodide

Methylammonium lead iodide is the first and the most studied organometallic halide in perovskite solar cells. $MAPbI_3$ is a semiconducting pigment with a direct band gap of 1.55 eV, a high optical absorption coefficient (α = 10^4-10^5 cm^{-1} in 300-780 nm), and a long electron/hole diffusion (exceeding 1 μm in polycrystalline film), which makes this material an ideal light harvester in solar cells.[15]

Reaction mechanism

The formation of $MAPbI_3$ is normally fulfilled by reacting PbI_2 and MAI:

$$PbI_2 + MAI \rightarrow MAPbI_3 \quad (2\text{-}28)$$

It has been observed that the reaction kinetics of this perovskite phase formation is ultra-fast. During the transformation into the perovskite lattice, spaces are formed between the layered $[PbI_6]$ octachedral that share crystal facets in PbI_2 to create $[PbI_6]$ octahedral that share only vertices in $MAPbI_3$.[75] This lattice transformation process is schematically illustrated in Fig. 2.23.

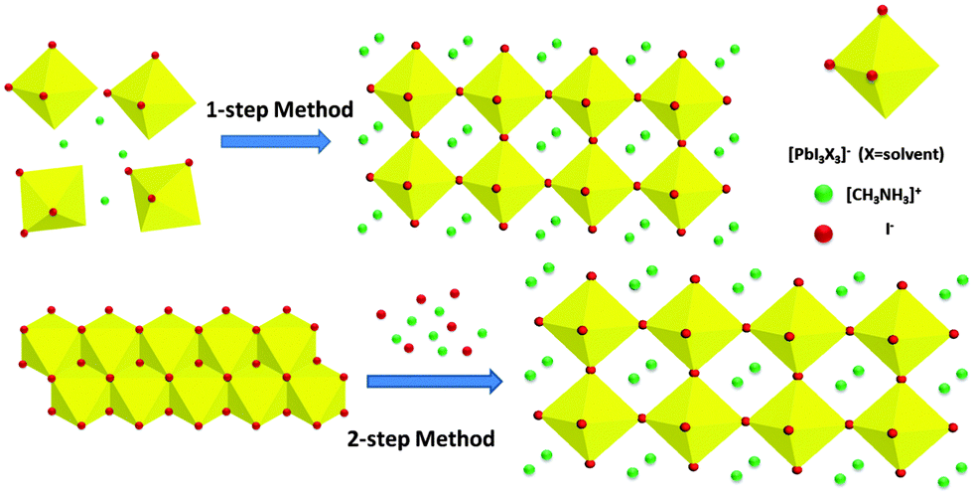

Figure 2.23 The growth scheme of $MAPbI_3$ perovskite by one-step and two-step methods.[76]

Band structure

Fig. 2.24 shows a typical calculated electronic band structure of $MAPbI_3$. It is seen that the electronic states at the top of the valence bands are of halide *p*-character, while those at the bottom of the conduction band are mainly derived from the metal *p* states. The calculated bandgap of $MAPbI_3$ (1.55 eV) is direct at Γ.[77]

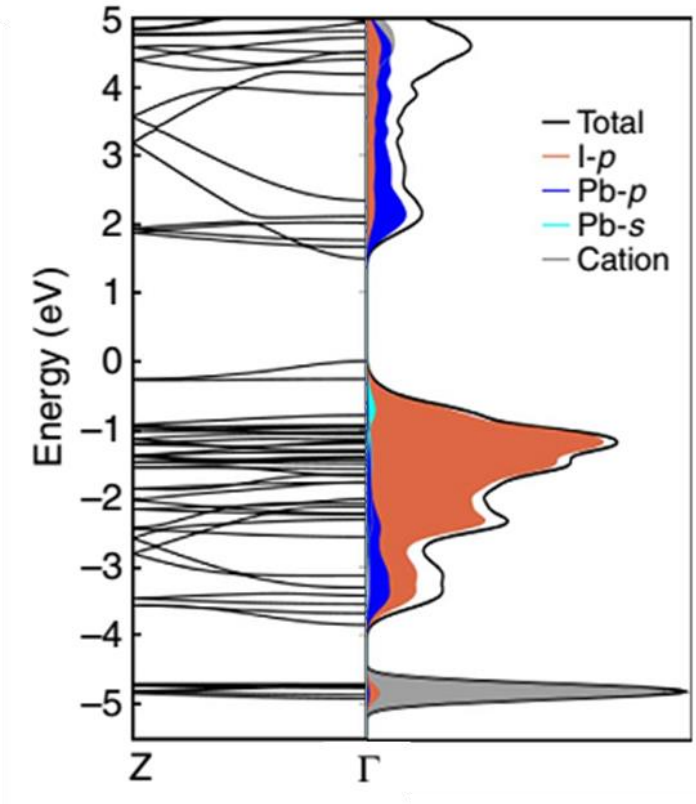

Figure 2.24 The band structure of $MAPbI_3$ calculated by DFT.[77]

Absorption coefficient

An ideal solar cell material should combine good optical absorption characteristics with efficient charge-transport properties.[78] Fig. 2.25(a) presents the absorption coefficient spectra of a $CH_3NH_3PbI_3$ film prepared on quartz substrate. The calculated α is 4.3×10^5 cm^{-1} at 360 nm, 1.3×10^5 cm^{-1} at 550 nm and 4×10^4 cm^{-1} at 750 nm. These coefficient values are comparable to or even higher than in many direct-bandgap III-V semiconductors, for instance GaAs, which is illustrated in Fig. 2.25(b). Due to the reasonably high absorption coefficient of $MAPbI_3$ in the visible region, it is possible to form a sufficiently thin yet strongly absorbing film, which is crucial to a bilayer device.[79]

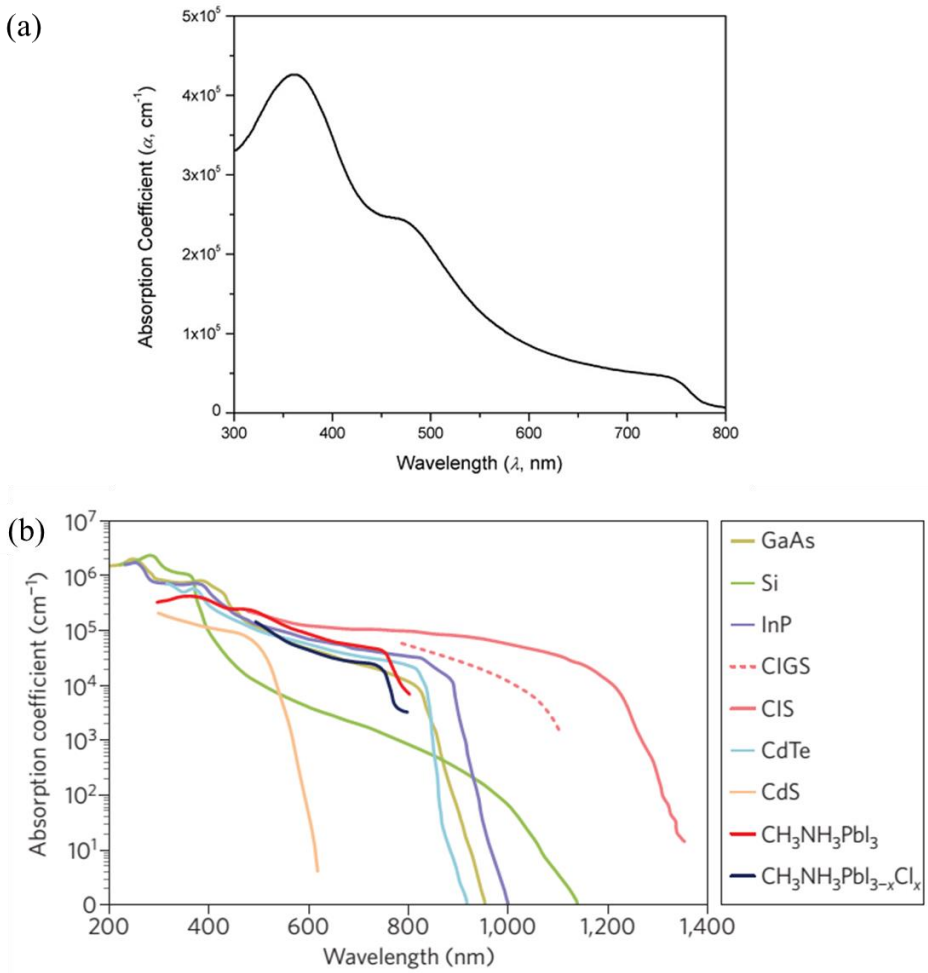

Figure 2.25 (a) Absorption coefficient spectra of $MAPbI_3$ film on quartz substrate;[80] **(b) The comparison of $MAPbI_3$ absorption coefficient with other solar cell materials.**[69]

Electron-hole diffusion length

The carrier diffusion within $MAPbI_3$ is sensitive to defects. Point defects in $MAPbI_3$, such as PbI_2 and CH_3NH_3I vacancy, do not make a trap state, but a large density of charge traps has been broadly observed at the grain boundaries and surfaces of $MAPbI_3$ polycrystalline films.[81,82]

Originally, it has been widely accepted that the effective charge diffusion length in polycrystalline $MAPbI_3$ films can reach as long as 300 nm since most best-forming

devices have a perovskite thickness of around 300 nm.[78,83,84] This idea was revised in August 2014 by Z.G. Xiao *et al*., where the carrier diffusion length was found to be larger than 1.0 μm in $MAPbI_3$ films containing large continuous grains.[85] In March 2015, the diffusion length value was further enhanced to above 3.5 μm by forming crystalline $MAPbI_3$ grains with very large size (up to 3.0 μm).[86] In the $CH_3NH_3PbI_3$ single crystals, the electron-hole diffusion lengths had been demonstrated to be larger than 175 μm, which greatly exceeded the absorption depth of photons with energy larger than the band gap of perovskites. This implied that internal quantum efficiencies of essentially 100 % can be achieved under the low internal electric fields under working device condition.[82] Therefore there is increasing interest to fabricate perovskite solar cells using $MAPbI_3$ single-crystals or $MAPbI_3$ films with large crystal grains.

2.3 Solar energy related applications

2.3.1 Energy efficient windows

Untreated glass is a poor heat insulator whereby windows become a major heat transfer path between the inside and outside of buildings, resulting in unwanted heat loss or input.[6] This is especially true in modern architecture, where a larger proportion of the exterior wall is designed and constructed with glass façades to be aesthetically pleasing and space efficient, but this also provides an additional challenge to its thermal efficiency.[4]

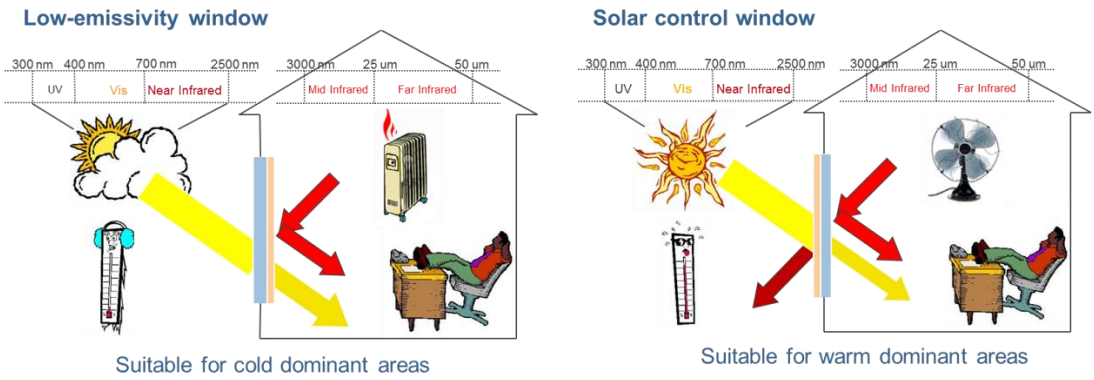

Figure 2.26 Schematic view of low emissivity and solar control windows.

Low emissivity (low-E) and solar control windows are two types of widely used energy efficient glazing, specifically designed for cold and warm climate dominant areas, respectively. Windows with low thermal emittance are produced by depositing spectrally selective coatings on the glass surface, which is able to maintain high transparency in solar wavelength (0.3 to 2.5 μm) and reflective in blackbody radiation range (3.0 to 50 μm). For solar control glazing, the coatings are ideally required to be highly reflective across the whole infrared range (0.8 to 50 μm) and also transparent to the visible light (0.4 to 0.8 μm), as illustrated in Fig. 2.26.

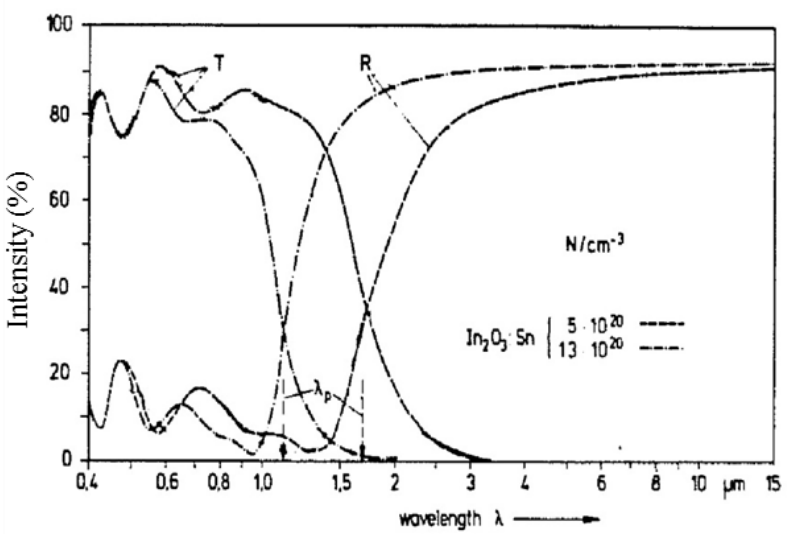

Figure 2.27 Transmittance and reflectance spectra of sprayed ITO films.[87]

Transparent conducting oxides can be used as energy efficient coatings if they 1) have a wide band gap (usually greater than 3 eV) which enables them to transmit light in the visible spectrum and 2) have a high carrier density (10^{20} to 10^{21} cm^{-3}) that can induce plasma reflection at the beginning (for solar control application) or middle (for low-E application) range of near infrared light. Two typical examples are ITO and FTO, which have already been very successfully utilized by glazing industry (such as NSG-Pilkington K-Glass). The carrier density in ITO coatings is easy to be tuned between 10^{20} and 10^{21} cm^{-3} to meet low-E or solar control applications (see Fig. 2.27). However, the scarcity of indium limits its further application. Alternatively, FTO coatings produced by APCVD on a float glass production line are popular in low-E glazing but not for solar control window, since the carrier concentration in FTO are difficult to increase beyond 10^{21} cm^{-3}. As a result, in recent years, doped ZnO becomes a promising candidate for new energy efficient coatings due to its tuneable carrier density (10^{20}-10^{21} cm^{-3}) as well as other unique properties, such as low-cost, high chemical and thermal stability, non-toxicity and ease of fabrication.[7,88]

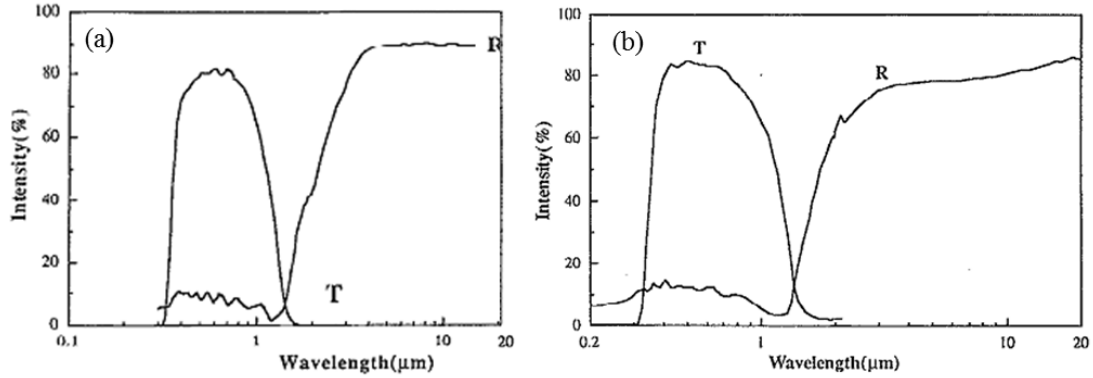

Figure 2.28 The transmittance and reflectance spectra of (a) Al-doped and (b) Ga-doped ZnO films prepared by APCVD.[58,59]

High quality group-III elements doped ZnO films have been fabricated by CVD techniques since the early 1990s. J. Hu *et al.* first prepared Al-doped and Ga-doped ZnO from APCVD method, whereby the films exhibit high carrier density (up to 10.6×10^{20} cm^{-3}), visible transmittance (> 80 %) and infrared reflectance (up to 90 % in the far infrared range).[58,59] The optical spectrum of two representative samples are shown in Fig. 2.28. However, the precursor they used, such as diethyl zinc and dimethyl zinc, are pyrophoric and quite expensive, so few studies followed on APCVD ZnO after that. In 2012, D.S. Bhachu *et al.* prepared ZnO:Al films by AACVD reaction of diethyl zinc and trimethylaluminium. It was found that the carrier concentration could reach 4.35×10^{20} cm^{-3} combined with moderate visible transmittance (~76 %) and infrared reflectance (35 % at 2500 nm).[89] High carrier density based Al-doped ZnO films (up to 1.85×10^{20} cm^{-3}) have also been produced by sol-gel methods, while there hardly have studies concerned about the film reflectance performance.[90]

2.3.2 Solar cells

Solar cell is an electronic device which directly converts sunlight into electricity. This photovoltaic energy conversion consists of two essential steps. First, absorption of light and generate an electron-hole pair. The electron and hole are then separated by the structure of the device, where the electrons will move to the negative terminal and holes will head to the positive terminal, thus generating electrical power.[91] The schematic view of a solar cell is illustrated in Fig. 2.29.

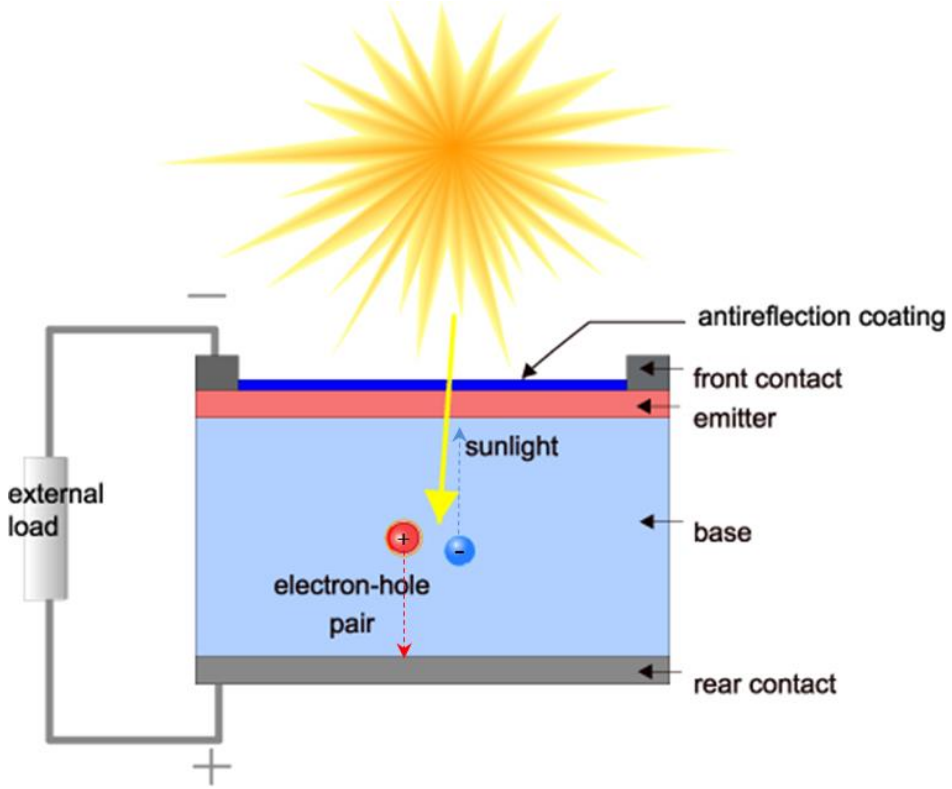

Figure 2.29 Schematic structure of a solar cell.[92]

Most currently installed PV arrays consist of crystalline or polycrystalline silicon (first generation solar cells); in second generation thin-film architectures, light is absorbed and charge generated in a solid layer of semiconductor, such as amorphous silicon (*a*-Si), cadmium telluride/cadmium sulfide (CdTe/CdS) and copper indium

gallium selenide (CIGS). Thin-film PV provides potentials for cost reduction in the manufacturing process due to the large materials savings. The third generation solar cells include nanocrystal based solar cells, polymer based solar cells, dye sensitized solar cells and the latest hybrid organic-inorganic perovskite solar cells.[71,93] Since PV technology has the potential to play a major role in future electricity supply, continuous efforts are being made by global researchers to develop low-cost, stable, efficient new generation solar cells.[71]

2.3.2.1 Thin film solar cells with textured TCO coatings

One important application for transparent conductive oxides is function as electrical electrodes in thin-film solar cells.[94] This is especially true when the TCO layer is surface textured because a rough surface can bring efficient light scattering inside the solar cell and, therefore, enhances light absorption along the longer scattering path (see Fig. 2.30), leading to an increase of the photo-generated current.[8,9] Highly surface-textured FTO and ZnO coatings have been successfully incorporated into a variety of photovoltaic devices, such as silicon thin film solar cells,[95] Cu_2O solar cells,[96] polymer solar cells,[97] and dye-sensitized solar cells.[98]

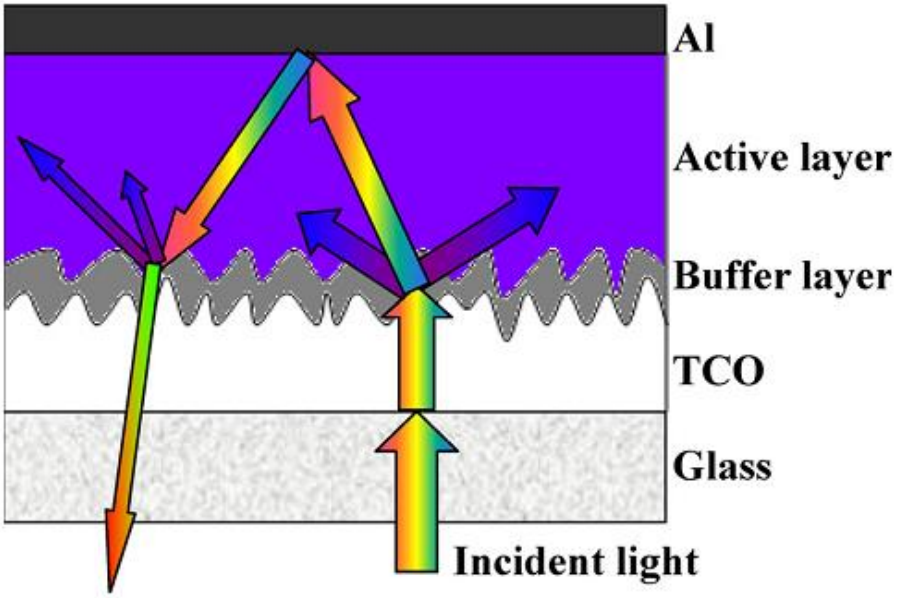

Figure 2.30 Device schematic with textured electrodes. Such textured electrodes with rough surface in combination with reflective back contacts provide efficient light-trapping by light scattering and multiple reflections to increase the length of the light.[97]

The light scattering ability can be quantified by haze factor, which is determined by the ratio between film diffuse transmittance (T_{diffuse}) and total transmittance (T_{total}):

$$\text{Haze} = T_{\text{diffuse}}/T_{\text{total}} = (T_{\text{total}} - T_{\text{direct}})/T_{\text{total}} \quad (2\text{-}29)$$

Where the total transmittance and direct transmittance of a film can be measured directly from a spectrometer, as illustrated in Fig. 2.31.

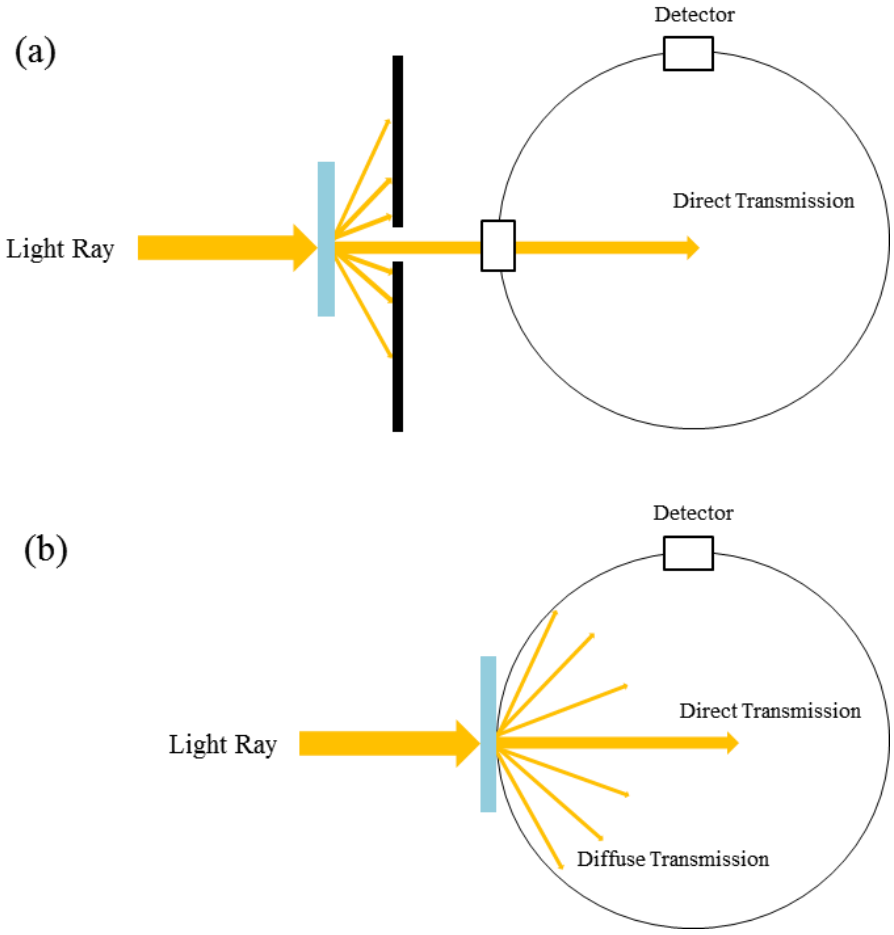

Figure 2.31 Schematic of (a) direct transmittance and (b) total transmittance measurement for TCO film.

In order to obtain high haze TCO thin films, two approaches, including the employment of controlled micro-/nano-structures and pre-/post- deposition chemical etching, are mainly investigated.[9,96] The latter is actually less favourable to be used since the additional process would increase the manufacturing cost considerably, and thus the deposition of intrinsically-textured TCO coatings has attracted greater attention. A proven example is the growth of transparent conductive B-doped ZnO films with random pyramidal texture by means of low pressure chemical vapour deposition, which has already been successfully employed in commercial thin-film

silicon solar modules with record performance.[10,99] Unfortunately, the zinc precursor used in the LPCVD process is diethylzinc. Therefore, continuous efforts are being made by the CVD community to explore novel cost-effective techniques and precursors for textured ZnO materials. The surface morphologies and haze performance of two representative textured ZnO coatings are shown in Fig. 2.32.

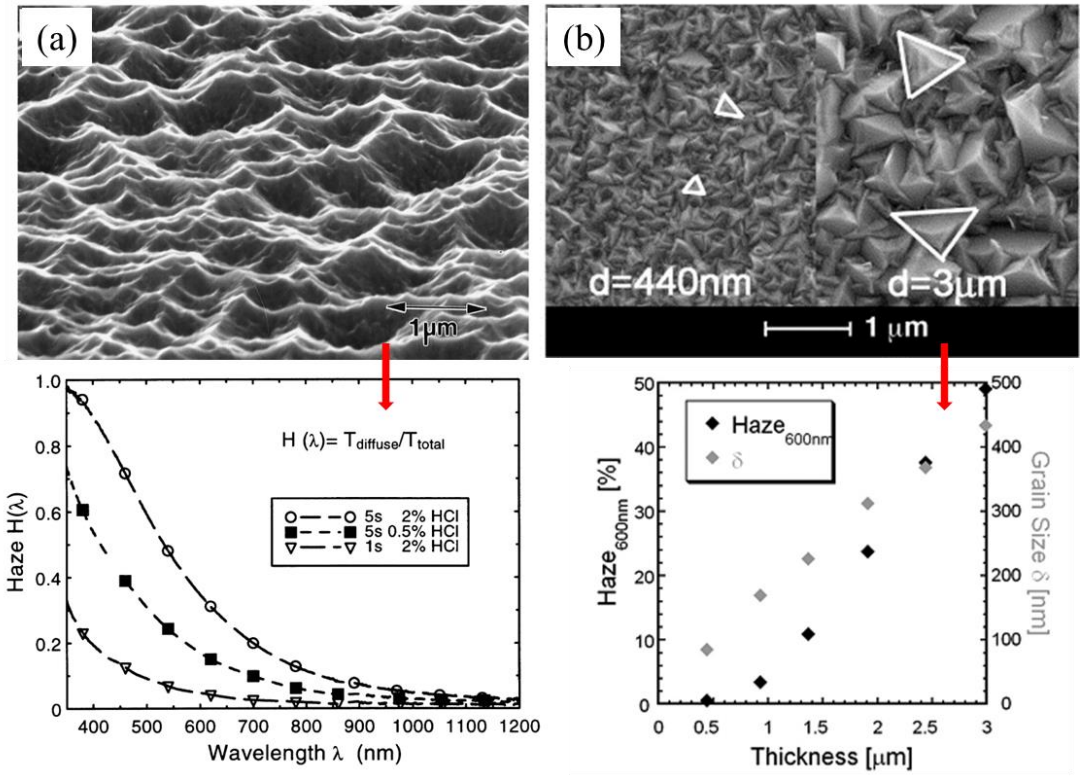

Figure 2.32 Surface morphologies and haze factors of (a) sputtered ZnO:Al film after etching and (b) ZnO:B film produced by LPCVD.[9,100]

It is noteworthy that, in addition to the large haze factor, the optical transmission and electrical conductivity of the TCO coatings should fulfil the requirements of electrical electrodes in solar cells (normally T_{vis} > 80 % and R_s < 20 Ω sq^{-1}).

2.3.2.2 Perovskite solar cells

During the past several years, organometallic halide based perovskite solar cells have emerged as a leading next-generation photovoltaic technology.[14] The first reported perovskite solar cells were devices equivalent to conventional dye sensitized solar cells in which the dye was replaced by $MAPbI_3$. Later it was found that $MAPbI_3$ has a very large carrier diffusion length and that indeed a TiO_2 semiconducting scaffold is not strictly needed.[101]

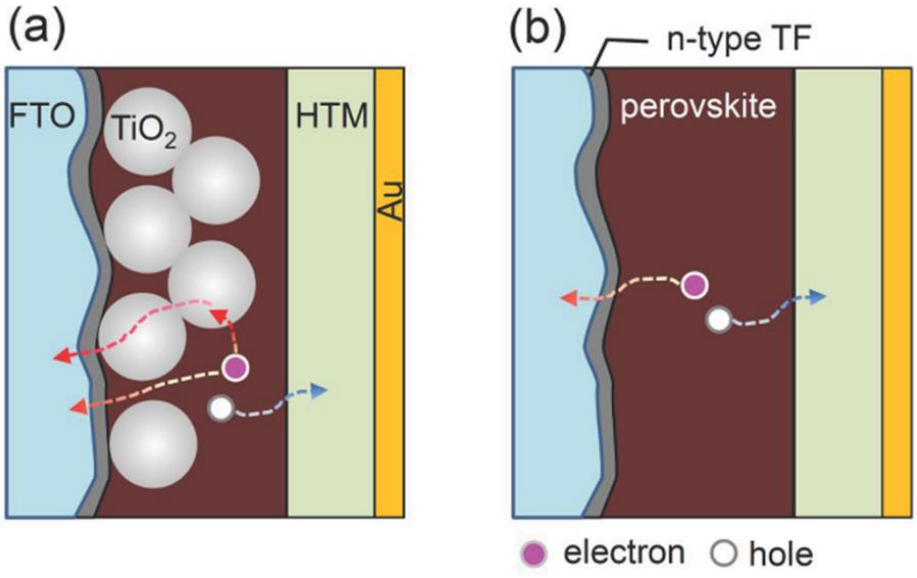

Figure 2.33 Device structures of (a) mesoscopic and (b) planar perovskite solar cells. In the mesoscopic structure, electrons can be collected directly and/or via mesoporous oxide layer, as in DSSC.[102]

The performance of perovskite solar cells is highly dependent on their architecture.[103] At present, devices based on a porous (also called mesocopic, Fig. 2.33(a)) or planar architecture (Fig. 2.33(b)), are the main focus of research and both structures could yield PCEs greater than 15 %. In the mesoscopic architecture, the organometallic halide can either be introduced as a thin layer (working as sensitizer)

that will just adequately cover the oxide scaffold with the pores in the scaffold infiltrated with charge transporting material, or it can form an overlayer on top of the completely infiltrated oxide scaffold.[103] A more straightforward planar architecture was developed afterwards and has enjoyed great popularity because removal of the mesoscopic layer significantly simplify device preparation and reduce materials cost.[83] The good performance in planar devices originates from the high crystalline nature of organometallic halide and their low trap densities, recombination within the perovskites thus being limited. As a result, the long-lived electrons and holes can be collected by electron and hole acceptor layers before making their way out of the solar cells as photocurrent.[78]

As the core part of perovskite solar cells, the morphology and crystal structure of the perovskite absorbers are key parameters for maximizing device efficiency, both being strongly influenced by the deposition techniques used. So far six main deposition methods have been reported including the solution-based one-step precursor deposition, sequential deposition process, two step spin-coating deposition; and the vapour-based dual source vacuum deposition, sequential vapour deposition, vapour-assisted solution process (shown in Fig. 2.34).[83,84,104,105] Among all, devices fabricated using either solution or vapour methods have yielded PCEs of over 15 %.

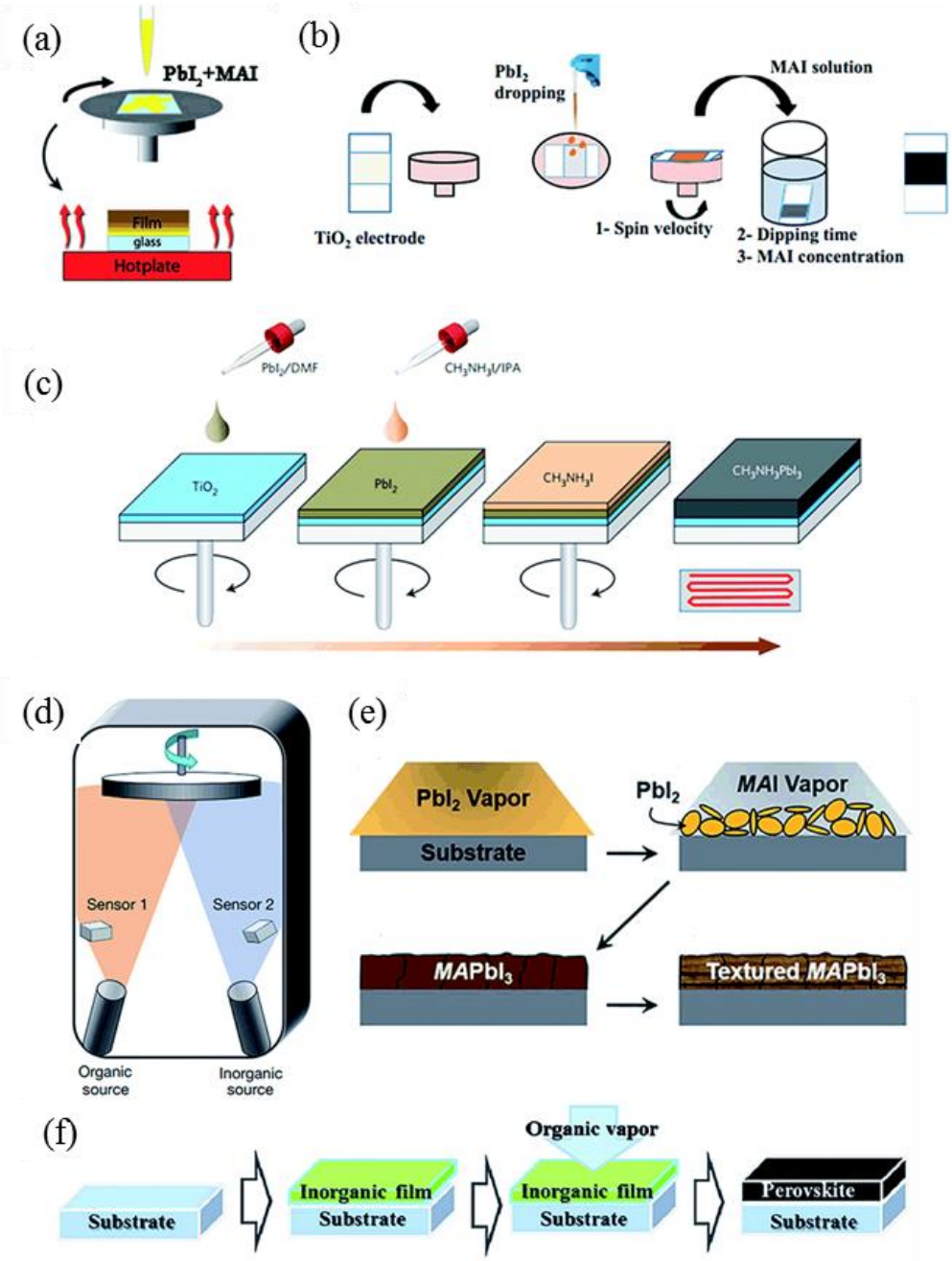

Figure 2.34 Six representative methods to prepare perovskite active layers: (a) one-step precursor deposition, (b) sequential deposition method, (c) two step spin-coating deposition, (d) dual-source vapour deposition, (e) sequential vapour deposition, (f) vapour-assisted solution process. [106,107]

While exciting efficiency values have been achieved for laboratory scale devices, the preparation of large-scale organometallic halide materials using cost-effective techniques is still a significant challenge for the PV industry. The solution-based sol-

gel spin coating process, although widely used among the research community due to its simplicity, is hard to scale up because it is extremely difficult to get uniform spin-coated hybrid perovskite films over a large glass substrate. Current vapour-based techniques could overcome the sample size limit but the requirement of high vacuum systems makes them expensive to scale up.[108] Thus the industrial-scale manufacturing of perovskite solar cells urgently calls for a new method that is suitable to coat high-quality perovskite films over a large area.[109]

Chapter 3 Experimental and Characterisation

3.1 Introduction

This chapter describes the experimental techniques used for the results shown in Chapter 4-7. Likewise, the equipment and methods used for characterisation and assessing functional properties are also presented.

3.2 Synthesis techniques

3.2.1 Sol-gel dip coating

Sol-gel dip coating process was performed on a dip coater, modified from a commercial syringe pump (Sage Instruments Model 341A). Fig. 3.1 shows the schematic view of the dip coater.

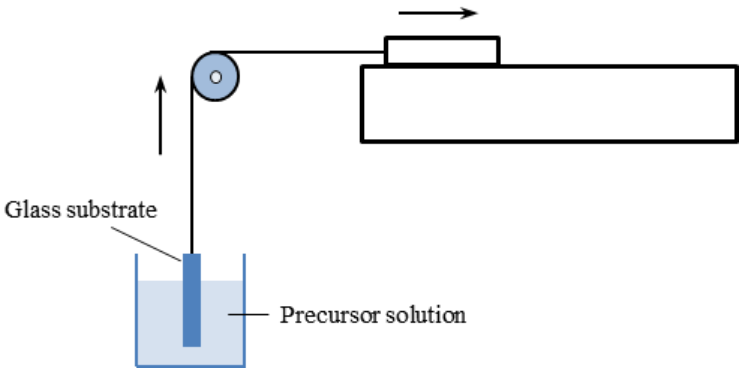

Figure 3.1 The schematic of sol-gel dip coater used for thin film deposition.

The glass slides were immersed into and withdrawn from the precursor solutions at a controlled speed. The as-deposited gel films were immediately transferred to a heated chamber furnace (Carbolite Type ELF 11/6B) to be dried and then cooled to the room temperature in the air for next dip. The procedures from coating to drying

were repeated for different times in order to obtain the films with desired thickness. The final heat treatments for the sol-gel samples were conducted in the same chamber furnace under air ambient and/or in a tube furnace (Lenton Type 3216CC) with selected gases (*i.e.* argon and hydrogen).

3.2.2 Aerosol assisted chemical vapour deposition

AACVD was performed on a horizontal bed cold-walled tubular reactor with dimensions of 6 cm diameter and 17 cm length. The schematic of a typical AACVD rig is illustrated in Fig. 3.2.

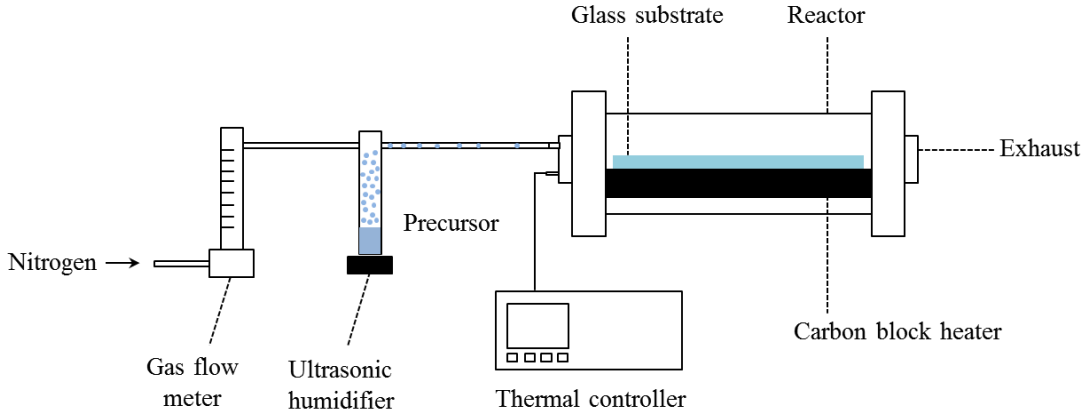

Figure 3.2 The schematic of AACVD set up used for thin film deposition.

The pre-mixed precursor solution was loaded into a glass flask, whereby the aerosol mist was generated using an ultrasonic humidifier (240 V, 50 Hz) bellow the flask and delivered to the reaction chamber with nitrogen gas (BOC, 99.9 %). The flow rate was controlled by a gas flow meter. The temperature of the reactor was set by heating a graphite block containing a Whatman heating cartridge, which was controlled by a Pt-Rh thermocouple.

3.3 Characterisation techniques

3.3.1 Scanning Electron Microscope (SEM)

The surface and cross-section morphologies of the films were studied using a FEI Inspect F Field Emission scanning electron microscope (FESEM) at an accelerating voltage of 10 keV and beam spot size of 3.5 nm. The elementary compositions of the samples were analysed using attached energy-dispersive X-ray spectrometer (EDS) at an accelerating voltage of 20 keV and beam spot size of 5.0 nm. All film thickness were determined by the SEM analysis.

3.3.2 Transmission Electron Microscope (TEM)

The microstructures of the films were further investigated by using a FEI Tecnai F30 high resolution transmission electron microscope (HRTEM) at an accelerating voltage of 300 keV.

3.3.3 X-ray Diffraction (XRD)

The crystal structures of the films were analysed using a Panalytical X'Pert Pro diffractometer in glancing incidence ($\alpha = 3°$) mode with CuKα radiation source ($\lambda = 1.542$ Å). The diffraction patterns were collected over 5-70° with a step size of 0.03° and a step time of 1.7 s per point. The XRD data were phase matched and processed using X'Pert Pro software. Glancing incidence model was selected instead of the conventional $\theta/2\theta$ scanning model because the XRD measurements of thin films using conventional method generally produces a week signal from the film and an intense signal from the substrates.[110]

3.3.4 X-ray Photoelectron Spectroscopy (XPS)

The surface compositions of the films were analysed by Thermo K-Alpha and Perkin Elmer Φ 5600ci X-ray photoelectron spectroscopy.

Thermo K-Alpha XPS analysis was conducted for the ZnO:Ga films (Chapter 4 and Section 5.4 in Chapter 5) and the $MAPbI_3$ films (Chapter 7) with monochromated Al-Kα radiation (1486.6 eV). In Chapter 4, the film surface information was collected without etching. In Section 5.4 and Chapter 7, the samples were etched by an Argon gun using a high current and energy of 3000 eV (corresponding to an approximate etch rate of 2.3 nm s^{-1} on a Ta_2O_5 standard). The data were analysed by using CASAXPS and calibrated to the C 1s signal at the binding energy (BE) of 284.6 eV, attributed to adventitious carbon.

Perkin Elmer Φ 5600ci XPS analysis was performed for the ZnO:Ga films (Section 5.3 in Chapter 5) at a pressure lower than 10^{-8} mbar with a non-monochromatized MgKα excitation source (1253.6 eV). The spectrometer was calibrated by assigning to the Au $4f_{7/2}$ line the binding energy of 84.0 eV with respect to the Fermi level and charging effects were corrected assigning to the C 1s line of adventitious carbon a value of 284.8 eV. Sputtering treatments were carried out by Ar^+ bombardment at 3.5 kV, with an argon partial pressure of $\approx 5\times10^{-8}$ mbar. Atomic composition (at.%) was estimated using sensitivity factors provided by Φ V5.4A software.

3.3.5 Atomic Force Microscopy (AFM)

The surface topographies of the films were characterized by a NT-MDT NTEGRA atomic force microscopy. Semicontact mode imaging was performed under air ambient conditions using silicon tips (Acta-20-Appnano ACT tapping mode with aluminium reflex coating, Nanoscience instruments) with a resonant frequency of 300 kHz and a spring constant of 40 N m^{-1}. Film surface roughness (root mean square roughness, R_{RMS}) was calculated with the Nova AFM software.

3.3.6 Electrical testing

The electrical properties of the films were examined by an Ecopia HMS-3000 hall measurement system and a four-point probe tester (Multi Height Probe with RM3000 Test Unit).

The bulk resistivity (ρ), carrier concentration (N) and carrier mobility (μ) of the ZnO:Ga films (Chapter 4-5) were studied by the van der Pauw method at room temperature using hall measurement system. Square-cut samples (1 cm × 1 cm) were subjected to a 0.58 T permanent magnet and a current of 0.1-1.0 mA during the tests. The sheet resistance (R_S) of the surface-textured ZnO films (Chapter 6) was measured by four-point probe technique.

3.3.7 UV-Vis-NIR Spectroscopy

The absorption, transmission and reflection spectra of the films were obtained by a Perkin-Elmer Fourier Transform Lambda 950 UV-Vis-NIR spectrometer.

UV/Vis/near IR total transmission and reflection spectra of the ZnO:Ga films (Chapter 4-5) were recorded in the range of 300 to 2500 nm. UV/Vis direct and total transmittance (T_{direct} and T_{total}) spectra of the surface-textured ZnO films (Chapter 6) were recorded in the range of 380 to 780 nm. The transmission spectra background was taken against an air background. UV/Vis absorbance spectra of the $MAPbI_3$ films (Chapter 7) were recorded in the wavelength range of 300-1000 nm using FTO glass as a reference to exclude the substrate contribution in the spectrum.

The average visible light transmittance of the films $T_{\lambda 380-780}$ was computed using equation (3-1) according to the British Standard EN 673:

$$T_{\lambda 380-780} = \frac{\sum_{\lambda=380\ \text{nm}}^{780\ \text{nm}} D_\lambda T(\lambda) V(\lambda) \Delta\lambda}{\sum_{\lambda=380\ \text{nm}}^{780\ \text{nm}} D_\lambda (\lambda) V(\lambda) \Delta\lambda} \tag{3-1}$$

Where D_λ is the relative spectral distribution of illuminant D_{65}; $T(\lambda)$ is the spectral transmittance of the glazing; $V(\lambda)$ is the spectral luminous efficiency for photopic vision defining the standard observer for photometry; $\Delta\lambda$ is the wavelength interval. Table 3.1 indicates the values for $D_\lambda V(\lambda)\Delta\lambda$ for wavelength intervals of 10 nm. The table has been drawn up in such a way that $\sum D_\lambda V(\lambda)\Delta\lambda = 1$.

Table 3.1 Normalized relative spectral distribution D_λ of illuminant D65 multiplied by the spectral luminous efficiency $V(\lambda)$ and by the wavelength interval $\Delta\lambda$.

λ nm	$D_\lambda V(\lambda)\Delta\lambda \cdot 10^2$	λ nm	$D_\lambda V(\lambda)\Delta\lambda \cdot 10^2$
380	0	590	6.3306
390	0.0005	600	5.3542
400	0.003	610	4.2491
410	0.0103	620	3.1502
420	0.0352	630	2.0812
430	0.0948	640	1.381
440	0.2274	650	0.807
450	0.4192	660	0.4612
460	0.6663	670	0.2485
470	0.985	680	0.1255
480	1.5189	690	0.0536
490	2.1336	700	0.0276
500	3.3491	710	0.0146
510	5.1393	720	0.0057
520	7.0523	730	0.0035
530	8.799	740	0.0021
540	9.4427	750	0.0008
550	9.8077	760	0.0001
560	9.4306	770	0
570	8.6891	780	0
580	7.8994		

3.3.8 Photoluminescence (PL) Spectroscopy

The PL spectra of the films were obtained on a photoluminescence spectroscopy at room temperature using a micro-Raman system in co-ordination with a He:Cd CW laser Triax 320 (325 nm exciation, 1200/1 mm grating, 30 mW output power).

Chapter 4 Sol-Gel Dip Coating of Gallium Doped Zinc Oxide Films

The following chapter describes the deposition of gallium doped zinc oxide films on silica glass substrates by using sol-gel dip coating method. To my dismay, these sol-gel ZnO:Ga films are unable to be employed as energy efficient glazing coatings due to insufficient charge carriers generated. However, it is still worth showing and discussing the ZnO structural and functional property variations as a function of deposition parameters from the perspective of a fundamental opto-electronic study.

4.1 Introduction

In the preparation of thin films by the sol-gel method, the thermal treatment process has a significant influence on the appearance and properties of the final film.[111] Traditional thermal process for the sol-gel deposited ZnO films can be divided into preheating and annealing in ambient air and post-annealing in a reducing atmosphere or under vacuum. The nucleation and grain growth during preheating and annealing govern the microstructural characterisation in ZnO films, *i.e.* film morphology, grain size and texture formation, while the post-annealing treatment determines the film conductivity to a large extent.[25,112] This is because the annealing in air not only promotes ZnO film crystallization, but also introduces extra defects, such as chemisorbed oxygen atoms, at grain boundaries or at the film surface, which act as electron trapping sites and form potential barriers. The oxygen desorption after annealing in reducing atmosphere or vacuum helps remove these tapping centres and

release trapped electrons, resulting in a higher electron mobility and concentration.[113–115] The hydrogen treatment may also promote the generation of oxygen vacancies inside ZnO grains, which produce intrinsic donors and increase the charge carrier density.[113]

It is worth noting that the chemisorbed oxygen absorption or desorption and the oxygen vacancy generation are all heat-activated processes. Thus both the heating temperatures have direct effect on the oxygen content and state in the final films, which determines the electric properties. However, previous sol-gel ZnO:Ga studies have mainly been concerned about the doping content and/or annealing temperature dependent film electronic performance.[116–118] No attempt has been made to link the annealing and post-annealing temperatures with the ZnO:Ga film properties at the same time. Moreover, in order to further improve the conductivity of ZnO:Ga coatings, the use of oxygen-deficient annealing atmosphere, for example argon, would be helpful since the amount of unwanted chemisorbed oxygen can be minimized to a large extent.

Thus, in this sol-gel study, I have adopted a variety of deposition parameters, including film thickness (230-480 nm), heating temperature (400-600 ℃) and atmosphere (Air/Argon), to optimize the final ZnO:Ga film structural and opto-electronic properties.

4.2 Experimental

The coating solution was prepared using zinc-acetate-dihydrate (ZAD; ≫ 99.0 %, Sigma-Aldrich), gallium-acetylacetonate (99.99 %, Aldrich), isopropyl alcohol (IPA; 99 %, Fisher Scientific) and monoethanolamine (MEA; ≫ 99.0 %, Sigma-Aldrich). The Zn concentration was 0.5 mol L^{-1} and the molar ratio of MEA to ZAD was maintained at 1.5. The amount of Ga, defined as 100 [Ga]/[Zn], was kept at 1.0 at.%, because earlier sol-gel ZnO studies showed that a 1.0-2.0 at.% Ga/Zn ratio in the precursor solutions could bring the best film electric performance.[117,119] The solution was stirred at 60 °C for 1h to yield a lucent and homogeneous mixture, and served as the coating solution after aging for more than 72 hours.

Silica coated float glass (30 mm × 60 mm × 2 mm, Pilkington NSG) was used as the substrate material. The glass slides were cleaned in an ultrasonic bath for 10 min with acetone, ethanol and deionized water, respectively, and dried under nitrogen. Then the coatings were created by dip-coating, the withdrawal rate was set as 2.8 cm min^{-1}. Each as-coated film was dried at 300 ℃ in air for 10 min. The procedures from coating to drying were repeated for different numbers in order to obtain the films with desired thickness. Under the traditional thermal process, after the deposition of the last layer, the films were annealed in air at 500 ℃ or 600 ℃ for 1 h in a muffle furnace. A separate post-annealing treatment was used to improve the film conductivity, all samples were annealed in a reducing atmosphere (95 % N_2 + 5 % H_2) at 400 ℃ or 500 ℃ for 1h in a tube furnace with a gas flow rate of 1 L min^{-1} before unassisted cooling. The modified thermal process included a 600 ℃ annealing in

argon for 1 h and a subsequent 500 ℃ post-annealing in reducing atmosphere for 1 h in the tube furnace. Both gas flow rate were determined as 1 L min^{-1}. Table 4.1 lists the experimental conditions for the studied sol-gel ZnO:Ga films.

Table 4.1 Experimental conditions for the preparation of ZnO:Ga film in sol-gel process.

Sample I.D.	Coating layers	Annealing temperature [℃]	Annealing atmosphere	Post-annealing temperature [℃]
A1	6	500	Air	400
A2	9	500	Air	400
A3	12	500	Air	400
A4	6	600	Air	400
A5	9	600	Air	400
A6	12	600	Air	400
A7	6	600	Air	500
A8	9	600	Air	500
A9	12	600	Air	500
A10	12	600	Argon	500

4.3 Results and discussion

Film composition

The surface elemental analysis of sol-gel ZnO:Ga films was carried out by using XPS and the spectra of three representative samples (A3, A6 and A9) are presented in Fig. 4.1. Their survey spectra indicate the presence of carbon, oxygen, zinc and gallium photoelectron signals. No other elements were detected in appreciable amounts. Fig. 4.1 also displays the high-resolution Zn 2p and Ga $2p_{3/2}$ XPS photoelectron signals for these samples. The peak positions of Zn $2p_{1/2}$ (BE ≈ 1045.5 eV) and Zn $2p_{3/2}$ (BE ≈ 1022.4 eV) agree well with the position expected for Zn in a ZnO lattice.[120,121] Regarding gallium, the Ga $2p_{3/2}$ peak position in A3 (BE ≈ 1119.2 eV) could indicate the presence of Ga(III) in an oxide environment,[122,123] but in A6 and A9 their peak signals almost disappear into the

background levels. The latter indicates that an increase of annealing temperature to 600 ℃ may prevent the substitution of gallium atoms into the ZnO lattice sites, such as segregating at grain boundary areas and form non-conductive gallium oxide. The gallium atomic percentage in A3 and A6 film surfaces can be calculated at 0.64 at.% and 0.14 at.%, respectively, while the content was unmeasurable in A9.

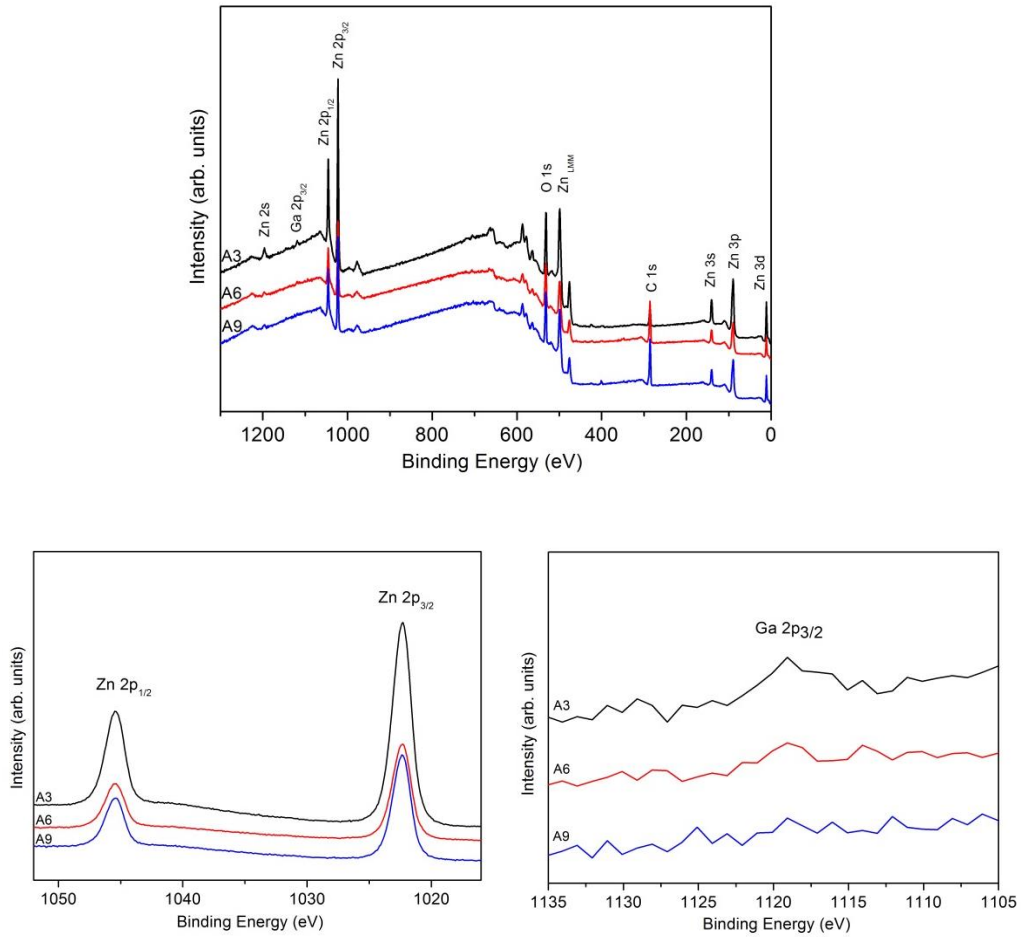

Figure 4.1 Wide-scan and high resolution XP spectra of three representative sol-gel dip-coated ZnO:Ga samples.

Structural properties

Fig. 4.2 shows the XRD patterns of sol-gel Ga-doped ZnO films prepared with different film thickness and heating temperatures. All the diffraction peaks in the

patterns correspond to the reflection of ZnO hexagonal wurzite structure (JCPDS 36-1451).[124] It is also seen that the (002) peak dominates in all patterns, which indicates that the ZnO:Ga films are composed by highly *c*-axis oriented growth polycrystals. Preferred orientation effects are common in zinc oxide films, and the crystallites tend to pack in the *c*-direction along the (002) plane. But there also has been a long discussion in the literature about the dominant mechanism of this texture formation should be a preferred nucleation or selective film growth.[25] Further investigation on the observed texture phenomenon will be discussed.

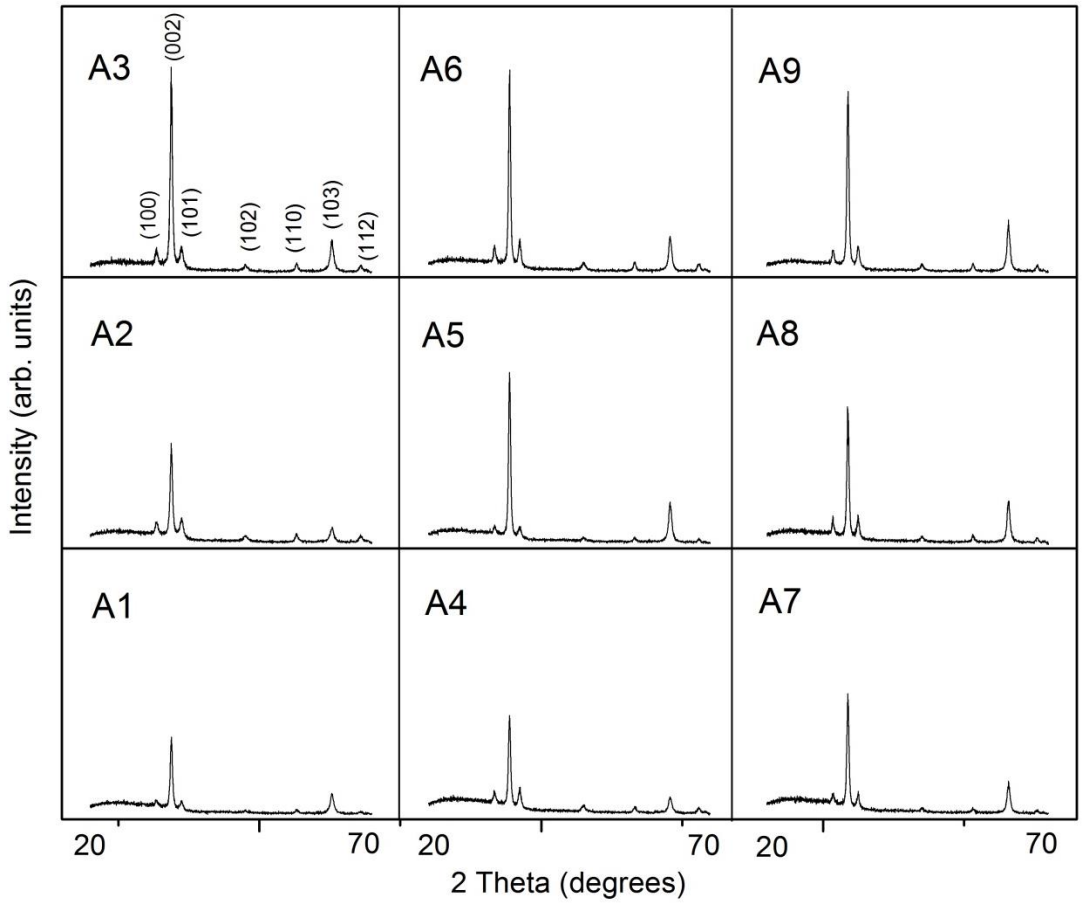

Figure 4.2 XRD patterns of sol-gel dip-coated ZnO:Ga films prepared over various film thickness, annealing and post-annealing temperature.

The (002) diffraction angle for the studied ZnO:Ga films are listed in Table 4.2. It can be seen that the 2θ values for the 500 °C annealed samples are all higher than those 600 °C annealed ones. According to Bragg's law ($2d\sin\theta = n\lambda$), the increase in diffraction angle corresponds to a reduction in the interplanar spacing (d_{002}). As the Ga^{3+} has a smaller ionic radius with respect to Zn^{2+}, the substitution of Zn^{2+} with Ga^{3+} at lattice sites should decrease the lattice constant [125] and shift of the diffraction peaks toward greater angles. Thus, the larger diffraction angles and lower interplanar distance in A1-A3 results from more substituted dopant atoms.

Moreover, it is observed that the (002) peak intensity, especially in samples annealed at 500 °C, is enhanced with increasing film thickness, representing the system crystal quality is being improved and crystallite size becoming larger. This thickness dependent film crystallinity can also be revealed by their SEM micrographs in Fig. 4.3. Among A1-A3, the particle size in A1 is relatively small (average grain size ~27 nm) and the connectivity between the particles is poor, representing a less crystalline film. The increase of film thickness helps improve the microstructure, and larger uniform granular particles can be observed in sample A2 (~35 nm in diameter). After the number of coating layer comes to 12, it appears that the small particles start to agglomerate with each together (agglomerate size 50-100 nm). This coalescence process could cause major grain growth but also result in microcracks which can be observed in the SEM image of A3 and in the literature.[126] For the films annealed at 600 °C, agglomerated particles are observed in all samples ranging from 6 to 12 layers. This indicates a higher heat input could promote grain growth and

coalescence process, so the thickness dependent crystal quality becomes less significant. In general, the crystallite size increases with film thickness and heating temperatures amongst the studied coatings, as illustrated in Table 4.2.

Table 4.2 Structural, electrical and optical properties of sol-gel dip-coated ZnO:Ga films prepared over different film thickness and thermal process.

Sample I.D.	Position of (002) peak	Crystallite size $d_{(002)}$ †	Thickness	Carrier concentration	Carrier mobility	Resistivity	Resistance ‡	$T_{\lambda 380-780}$
	[Deg.]	[nm]	[μm]	[$\times 10^{19}$ cm^{-3}]	[cm^2 $V^{-1}s^{-1}$]	[$\times 10^{-2}$ Ω cm]	[KΩ sq^{-1}]	[%]
A1	34.374	20.5	0.25	1.16	2.7	20.20	8.10	81.2
A2	34.368	19.5	0.36	1.95	1.4	22.80	6.35	87.9
A3	34.370	21.0	0.48	2.44	1.6	16.29	3.40	87.7
A4	34.347	21.5	0.23	0.91	5.4	12.78	5.60	79.2
A5	34.357	23.0	0.35	0.68	9.0	10.21	2.90	85.5
A6	34.358	24.0	0.46	0.67	13.7	6.78	1.50	83.2
A7	34.358	22.5	0.26	1.23	12.9	3.92	1.50	83.9
A8	34.363	23.0	0.38	1.18	15.2	3.48	0.90	83.2
A9	34.362	23.5	0.47	1.07	21.0	2.78	0.60	87.3
A10	34.352	14.0	0.48	3.38	15.7	1.18	0.25	87.0

† The crystallite size $d_{(002)}$ was determined by using Scherrer equation $d = 0.94\lambda/\Delta(2\theta)\cos\theta$, where λ is the wavelength of X-ray, θ is the diffraction angle for (002) peak, and $\Delta(2\theta)$ is t he full width at half maximum of (002) diffraction peak.

‡ The sheet resistance R_s is calculated by using equation (2-18).

Figure 4.3 Plane-view SEM micrographs illustrating the morphology changes of sol-gel dip-coated ZnO:Ga films with different film thickness, annealing and post-annealing temperature. The insets show cross-sectional images for each sample.

Annealing temperature	Post-annealing temperature	Coating layers		
		6	9	12
500 ℃	400 ℃	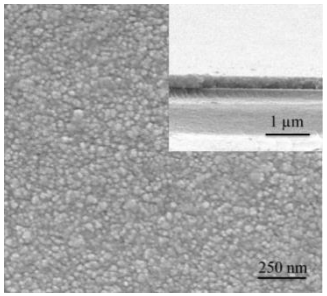	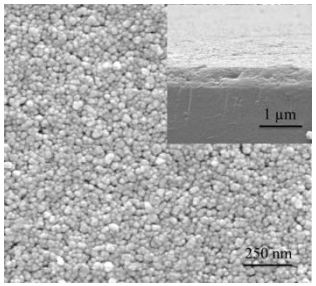	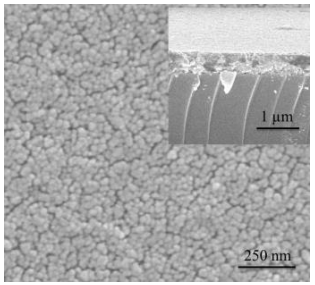
600 ℃	400 ℃	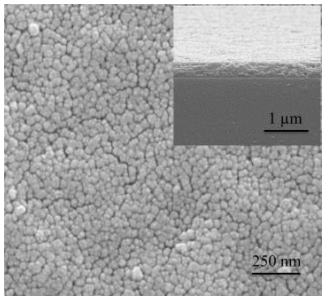	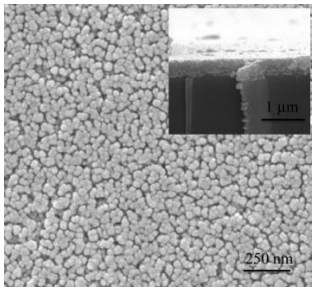	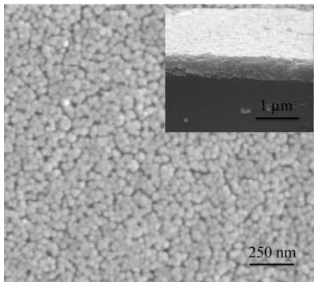
600 ℃	500 ℃	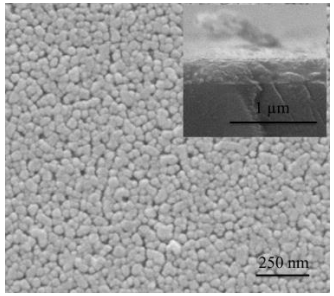	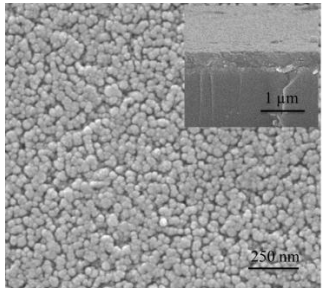	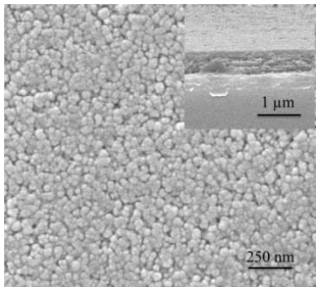

The crystallization process of thin films can be divided into three steps: the nucleation process, the initial growth process and the ensuing coalescence process.[7] The poor connected microstructure in A1 represents that the rate of nucleation and grain growth are limited under the given film thickness and annealing temperature. The presence of impurities, *i.e.* dopant atoms, from either solute or precipitate drag could reduce the grain growth rate,[32] so the particles stop growing before they come into direct contact. This is also the reason for the much smaller grain size in sol-gel doped ZnO film with respect to the undoped case.[127] Moreover, in the thin film growth, it is generally observed that the grain size increases with film thickness,[128] but the mechanism behind this varies as a function of the deposition method. In the sol-gel process, the increase of film thickness is fulfilled by adding the number of coating layers and prolongs the preheating time accordingly, which helps eliminate more solvent and organics in the existing layers and promote nucleation. This can be verified by the XRD patterns of the ZnO:Ga films prior to annealing, where the peak intensity increases continuously from 6 layers to 12 layers in Fig. 4.4. Thus, in a thicker film, the nucleation rate could be higher and grains are easier contact each other after the initial grain growth, and then coalescence process could happen. As a result, the particle size increases in A2 and agglomerated particles can be observed in A3. Also, when the films are annealed under a higher temperature, ZnO grains will gain more energy to grow up and coalescence process is already happened in A4 with only 6 coating layers. This thickness and temperature dependent film microstructure change is illustrated in Fig. 4.5.

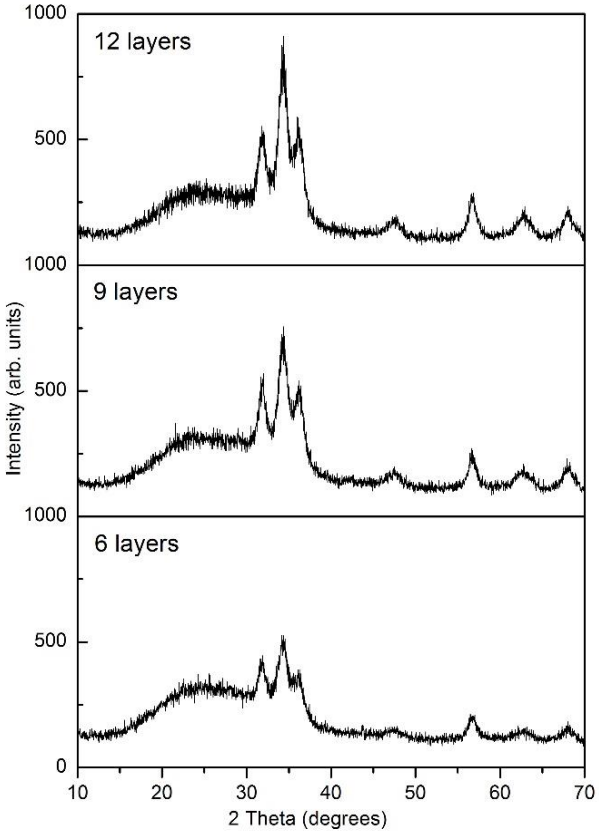

Figure 4.4 XRD patterns of sol-gel dip-coated ZnO:Ga films with different coating layers prior to annealing.

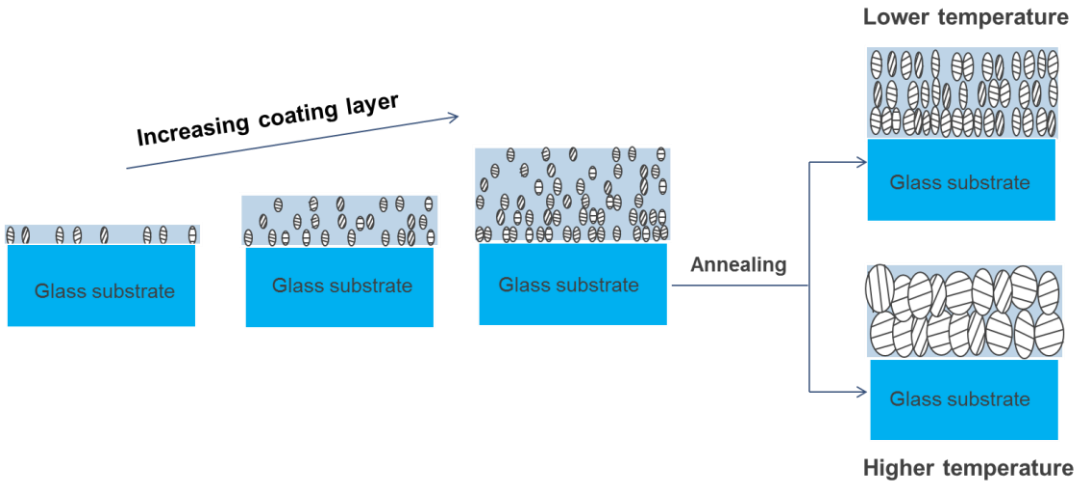

Figure 4.5 Schematic view of the thickness and temperature dependent sol-gel ZnO film microstructure change.

In addition, since a preferred orientation already exists in the as-deposited films (prior to annealing), I could conclude that the *c*-axis oriented texture in present ZnO:Ga coatings should result from a preferred nucleation in the early growth stage. This idea can be further supported by the existence of an obvious texture in the diffraction pattern of A1 as its initial growth is incomplete and no coalescence evidence is observed. The grain growth could reduce the non-crystalline area and improve the film crystallinity, so the relatively (002) peak intensity in A2 is a little higher compared with A1. Moreover, the coalescence process after nucleation and initial grain growth could play an essential role in forming a strong texture. This can be explained in two ways: on the one hand, agglomerated particles could further minimize the non-crystalline boundary areas; on the other hand, those crystallites with higher surface energy will be overgrown by the lowest ones during this process. As a result, highly *c*-axis oriented crystallites are observed in sample A3.

Electrical properties

Table 4.2 presents the Hall measurement data for the sol-gel ZnO:Ga films prepared under traditional thermal process (A1-A9). It is seen that all the studied coatings are n-type semiconductors and the specimen resistivity shows an overall decrease with film thickness and heating temperatures, with a minimum resistivity of 2.78×10^{-2} Ω cm obtained in A9. The film resistivity is a little higher than previously reported values for spin-coated 1 at.% Ga-doped ZnO film ($\sim5.0\times10^{-3}$ Ω cm) under similar thermal process,[119] but compared with those vacuum-deposited ZnO:Ga coatings, whose resistivity could reach an order of 10^{-4} Ω cm,[129,130] these sol-gel samples are much less conductive. The relatively inferior electric performance for the present films could relate to their refined open-packed nanocrystal grains (as shown in the SEM images, Fig. 4.3), which brings a large amount of unfavourable

grain boundary defects. J.M. Stiegler *et al.* studied the free-carrier distribution in ZnO crystals and they found that the grain boundaries are easy to trap and scatter charge carriers, leading to lower film conductivity.[131] By comparison, the vacuum-deposited films often exhibit pronounced columnar grains and such defects can be minimized, but accordingly the ultra-high vacuum systems they used require much higher instrument investment and maintenance costs. The non-crystalline grain boundary areas in sol-gel derived ZnO coatings can be reduced by using rapid thermal annealing techniques,[117] while it also increases the manufacturing costs since high power density lamps or lasers are used.

In addition, at an annealing temperature of 500 ℃, the carrier concentration increases with the film thickness and a maximum value of 2.44×10^{19} cm^{-3} can be obtained; while for the samples annealed at 600 ℃, the carrier density is obviously lower and hardly change with film thickness, but the corresponding charge carrier mobility increases continuously from 5.4 to 21.0 $cm^2 V^{-1}s^{-1}$. Furthermore, comparing the samples with identical coating layers between A4 to A6 and A7 to A9, it is shown that a higher post-annealing temperature could help raise both the carrier concentration (from $0.67\text{-}0.91\times10^{19}$ cm^{-3} to $1.07\text{-}1.23\times10^{19}$ cm^{-3}) and the mobility (from 5.4-13.8 $cm^2 V^{-1}s^{-1}$ to 12.9-21.0 $cm^2 V^{-1}s^{-1}$) to some degree.

The charge carriers in the studied ZnO:Ga films include free electrons generated by Ga doping and oxygen vacancies formed during post-annealing process. The number of oxygen vacancies in ZnO decrease with the improvement in crystallinity,[132] thus in A1 to A3, the increased carrier number from 1.16×10^{19} cm^{-3} to 2.44×10^{19} cm^{-3} with film thickness should originate from a higher Ga doping efficiency with improved film crystallinity (or reduced grain boundary areas). A higher annealing temperature will enhance the absorption of oxygen to the

film,[133] this oxygen concentration increase is favourable to the formation of certain nonconductive gallium-containing oxide,[134] which degrades the doping efficiency and traps free electrons although the amount should be limited and cannot be detected in the XRD pattern. Also the reduction of these oxide phases during post-annealing is more difficult because they are better crystallized.[134] As a result, an obvious decrease in the carrier concentration is observed in A4 to A6 ($0.67\text{-}0.91\times10^{19}$ cm^{-3}). In spite of this, the enlarged crystallite size after higher temperature annealing helps enhance the charge carrier mobility and the film conductivity is improved. Moreover, the increase in post-annealing temperature could accelerate removing the free electron trapping centres and generating oxygen vacancies. Thus, both the concentration and mobility of free charge carrier in A7 to A9 show a minor improvement compared with the corresponding samples in A4 to A6, and the most conductive sample is obtained in A9 (2.78×10^{-2} Ω cm).

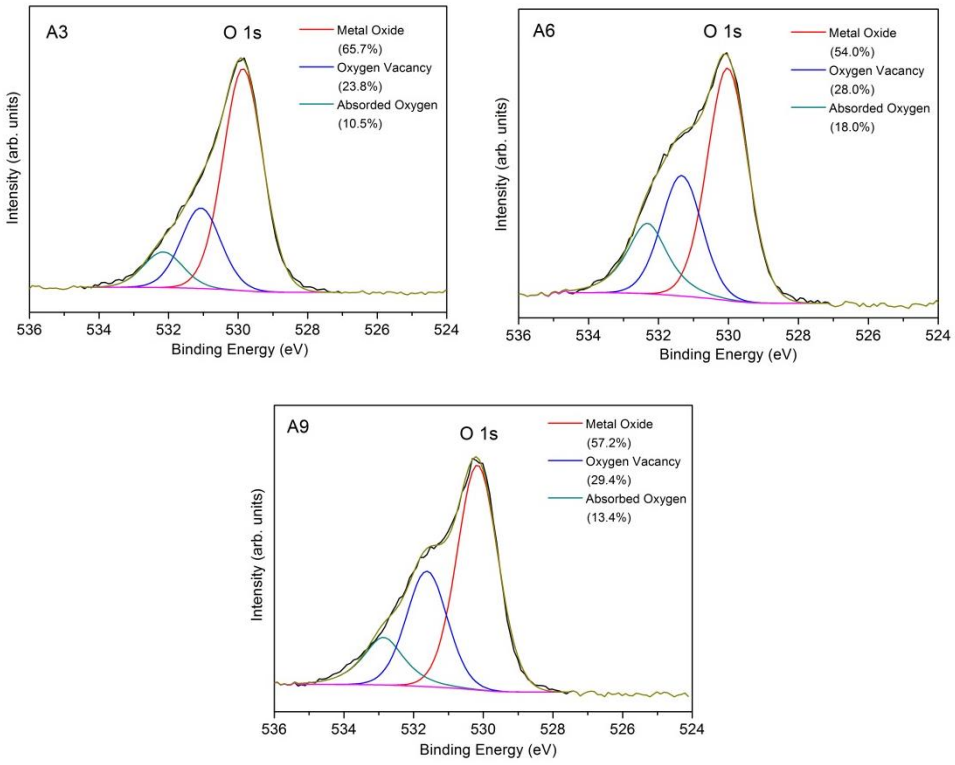

Figure 4.6 High resolution O 1s XP spectra of sample A3, A9 and A9.

The above explanations can be further supported by the narrow scan O 1s photoelectron signals of three representative samples A3, A6 and A9. As shown in Fig. 4.6, the O 1s peaks that were fitted using Gaussian fitting were cantered at 530.2 eV, which represents the oxygen bonds from metal oxide, 531.3 eV, which is related to the oxygen bonds with oxygen vacancy, and 532.4 eV, which is attributed to the chemisorbed oxygen.[135–137] The atomic ratio of different oxygen bonds are calculated and inserted in the corresponding figure. It is seen that the concentration of chemisorbed oxygen is enhanced greatly from 10.5 % in A3 to 18.0 % in A9, resulting in a reduced doping efficiency. The existence of more substituted gallium atoms in A3 can indeed be verified by its lower oxygen vacancy concentration, where the oxygen atoms are boned more strongly with gallium with respect to zinc and the generation of oxygen vacancy is suppressed.[138,139] The rise of post-annealing temperature hardly increases the content of oxygen vacancy but reduces the chemisorbed oxygen content considerably (13.4 % in A9), thus a few more electrons are released.

Improved electrical properties by modified thermal process

Based on the above analysis, under the traditional thermal processing, it is hard to get both the carrier density (> 2×10^{19} cm^{-3}) and carrier mobility (> 10 cm^2 $V^{-1}s^{-1}$) satisfied at the same time for the ZnO:Ga coaings produced via sol-gel route; therefore, a different thermal treatment is required to break the dilemma. In the modified process, the annealing atmosphere of air was replaced by the oxygen-free argon gas and a subsequent post-annealing process was employed instead of previous separated one.

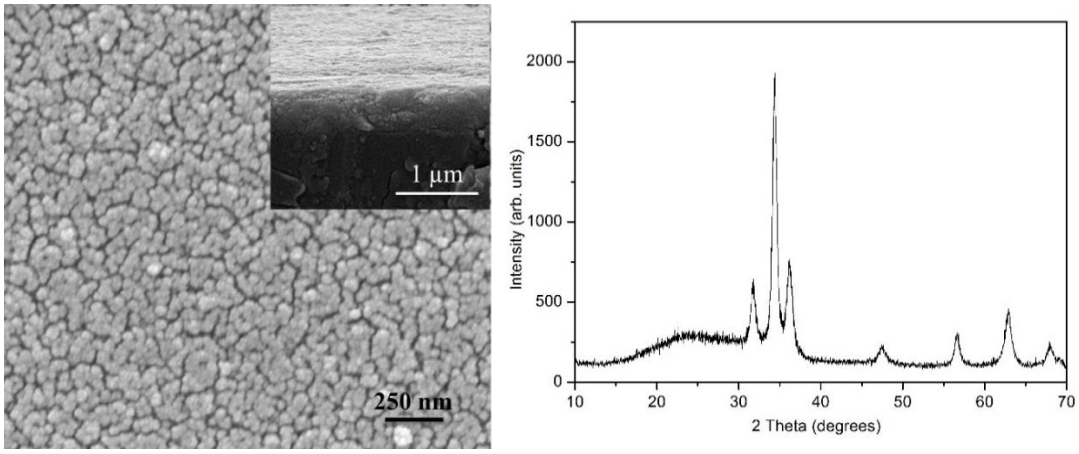

Figure 4.7 SEM images and XRD pattern of sample A10.

The consequent film structural results are shown in Fig. 4.7. The SEM image illustrates that the argon-annealed ZnO:Ga sample is composed of agglomerated particles, but its X-ray diffraction peaks seem less intense compared with previous air-annealed specimens and a small crystallite size of 14 nm is calculated for A10. This indicates the previous air atmosphere could promote ZnO crystallization in a better way, which is not hard to understand because excess oxygen source is provided during ZnO crystal growth. In spite of the smaller crystallites, the new thermal method could still effectively improve the film electrical properties, as shown in Table 4.2. Compared to the most conductive sample A9 above, the resistivity of corresponding sample A10 reduced from 2.78×10^{-2} Ω cm to 1.18×10^{-2} Ω cm with a favourable carrier concentration of 3.38×10^{19} cm^{-3} and mobility of 15.7 cm^2 $V^{-1}s^{-1}$ together. The obtained higher carrier density in A10 is attributed to the large increase of the oxygen vacancy (from 29.4 % in A9 to 51.1 % in A10) and the reduction of chemisorbed oxygen content (from 13.4 % in A9 to 3.4 % in A10) under the oxygen-deficient annealing atmosphere, as illustrated by its O 1s XPS peak in Fig. 4.8. Also the Ga $2p_{3/2}$ peak in A10 is sharper compared with previous ones and its surface gallium atomic percentage is calculated at 0.37 at.%.

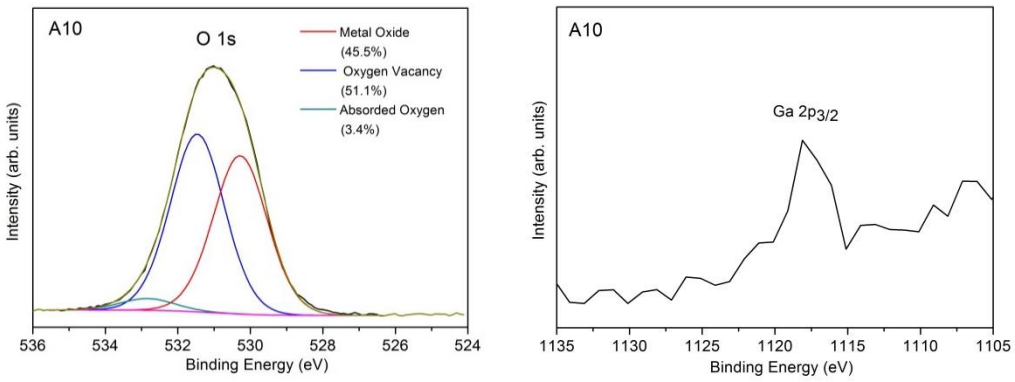

Figure 4.8 High resolution O 1s and Ga 2p XP spectra of sample A10.

Optical properties

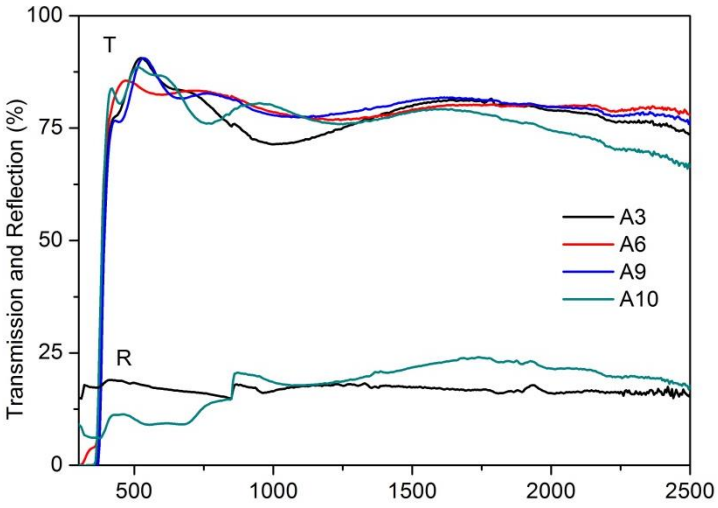

Figure 4.9 UV/Vis/NIR transmission spectra of sample A3, A6, A9 and A10 and reflection spectra of sample A3 and A10.

The optical transmission and reflection spectra (300-2500 nm) of representative sol-gel dip coated ZnO:Ga samples prepared by both traditional and modified thermal processes are shown in Fig. 4.9. It is seen that all films exhibit high transparency across the visible light (with an average value of 80-90 %, as listed in Table 4.2) and near infrared range (> 70 %). Accordingly, no obvious evidence of transmission reduction can be observed and their reflectance values are extremely low (< 25 %), as illustrated by the reflection spectra of sample A3 and A10. This represents the

carrier densities in concerned ZnO:Ga films are insufficient to induce a plasma reflection in the near infrared range and cannot be utilized as energy efficient glazing coatings.

4.4 Conclusions

In this chapter, Ga-doped ZnO films were prepared using the sol-gel dip coating method and the effects of film thickness, heating temperature and atmosphere on the system structural and opto-electronic performances were investigated. The results demonstrated that highly *c*-axis oriented crystals could be easily formed in ZnO:Ga coatings, which originated from a preferred nucleation and got fully developed during structure evolution. An increase in film thickness prolonged the preheating process and promotes nucleation, resulting in a more crystalline film after annealing. Higher temperature annealing (600 °C) in air could degrade the Ga doping efficiency and decrease the carrier concentration, but the enlarged grain size helped enhance the carrier mobility and improve the film conductivity. Under a modified annealing process in argon, favourable carrier density (3.38×10^{19} cm^{-3}) and mobility (15.7 cm^2 $V^{-1}s^{-1}$) were obtained at the same time, resulting in a minimum film resistivity of 1.18×10^{-2} Ω cm. The studied ZnO:Ga coatings kept transparent both in the visible and near infrared light due to the insufficient carrier density.

Chapter 5 AACVD of Gallium Doped Zinc Oxide Films

The following chapter describes the deposition of gallium doped zinc oxide films on silica glass substrates using AACVD method utilising low-cost zinc and gallium acetylacetonates as precursors. The resulting ZnO:Ga films exhibit high visible transparency (> 80 %) and infrared reflection (up to 48.9 % at 2500 nm) together, which is close to the optical requirements for commercial energy saving glazing.

5.1 Introduction

In recent years, aerosol assisted CVD has been increasingly utilized to fabricate TCO materials because it could provide a wider availability of precursors for high quality CVD products.[22,51,140] The architecture of AACVD thin films can be easily tailored by tuning deposition conditions, *i.e.* the physical properties of the carrier solvent, the species of carrier gas, the growth temperature and time (or film thickness).[17,141,142] This is important because the morphology of a film directly influences its optical performance and application, as described in Section 2.3.2.1 (Chapter 2). Moreover, for TCO material deposition, the introduction of doping atoms could also alter film growth processes, resulting in different film structure and spatial organization. As a result, the morphology and bulk properties of TCO films can be modified by adding various type and amount of dopant material. The doping element, including Al, In, F, Cu and Ag, in ZnO film deposition has been reported in earlier AACVD works.[89,143,144] However, to my knowledge, no attempt has been made to introduce gallium into ZnO films via the AACVD route.

Based on the above observations, here I have undertaken a detailed investigation of the effects of doping content, deposition temperature and time on the AACVD

ZnO:Ga film growth behaviour and opto-electronic properties. The main goal of this work was to characterize the film composition, structure, morphology, electrical and optical properties prepared under different conditions, discussing the interplay between the system structural parameters and functional performances.

5.2 Experimental

The precursor solution was made by mixing zinc-acetylacetonate-monohydrate (Aldrich) and gallium-acetylacetonate (99.99 %, Aldrich) in methanol (≫ 99.6 %, Sigma-Aldrich). The mixture was stirred for at least 20 min to ensure the chemicals had dissolved. An aerosol was then generated by using an ultrasonic humidifier and transported to the reaction chamber with a 2 L min^{-1} N_2 flow (99.9 %, BOC). Deposition was carried out on silica coated float glass (150 mm × 45 mm × 4 mm, Pilkington NSG).

ZnO:Ga films prepared with various Ga contents

In this work, the precursor solutions were prepared by dissolving 1.2 g zinc-acetylacetonate-monohydrate and various amount of gallium-acetylacetonate ranging from 0.017 g to 0.168 g (Ga/Zn molar ratio from 0.5 % to 5 %) in 120 mL methanol. The substrate temperature was kept at 350 ℃ and the deposition time was around 90 min. The detailed experimental conditions and corresponding sample I.D. are listed in Table 5.1.

Table 5.1 Experimental conditions for the preparation of AACVD ZnO:Ga films with various Ga contents.

Sample I.D.	Zinc-acetylacetonate-monohydrate	Gallium-acetylacetonate	Methanol	Ga/Zn ratio	Deposition temperature	Deposition time
	[g]	[g]	[mL]	[%]	[℃]	[min]
ZnO	1.2	0	120	0	350	90
ZnO:Ga(0.4)	1.2	0.017	120	0.5	350	90
ZnO:Ga(0.8)	1.2	0.034	120	1.0	350	90
ZnO:Ga(3.0)	1.2	0.067	120	2.0	350	90
ZnO:Ga(2.3)	1.2	0.101	120	3.0	350	90
ZnO:Ga(4.3)	1.2	0.134	120	4.0	350	90
ZnO:Ga(6.1)	1.2	0.168	120	5.0	350	90

ZnO:Ga films prepared over different deposition temperature and time

In this work, the zinc concentration and the Ga/Zn molar ratio was maintained at 1.0 g L^{-1} and 2.0 %, respectively in precursor solutions. Two optimum substrate temperatures, 400 ℃ and 450 ℃, were utilized and the deposition time was set at 45-180 min, respectively to obtain desired film thickness. The detailed experimental conditions and corresponding sample I.D. are listed in Table 5.2.

Table 5.2 Experimental conditions for the preparation of AACVD ZnO:Ga films over different deposition temperature and time.

Sample I.D.	Zinc-acetylacetonate-monohydrate	Gallium-acetylacetonate	Methanol	Ga/Zn ratio	Deposition temperature	Deposition time
	[g]	[g]	[mL]	[%]	[℃]	[min]
B1	0.6	0.034	60	2.0	400	45
B2	1.2	0.067	120	2.0	400	90
B3	1.8	0.101	180	2.0	400	135
B4	2.4	0.134	240	2.0	400	180
B5	0.6	0.034	60	2.0	450	45
B6	0.9	0.054	90	2.0	450	65
B7	1.2	0.067	120	2.0	450	90
B8	1.8	0.101	180	2.0	450	135

Fig. 5.1 presents the image of a typical AACVD ZnO:Ga film on glass surface. The deposited material is optically transparent and electrical conductive. Based on the resistance values roughly measured by a digital voltmeter, the ZnO:Ga coating can be divided into three sectors, which are marked as A, B and C, respectively along

the gas flow direction. It is worth mentioning that, at 350 ℃ and 400 ℃, the films in area B are always the most conductive sector on glass surface, while the samples in area A exhibit lower resistance than that of area B and C when the temperature rises to 450 ℃.

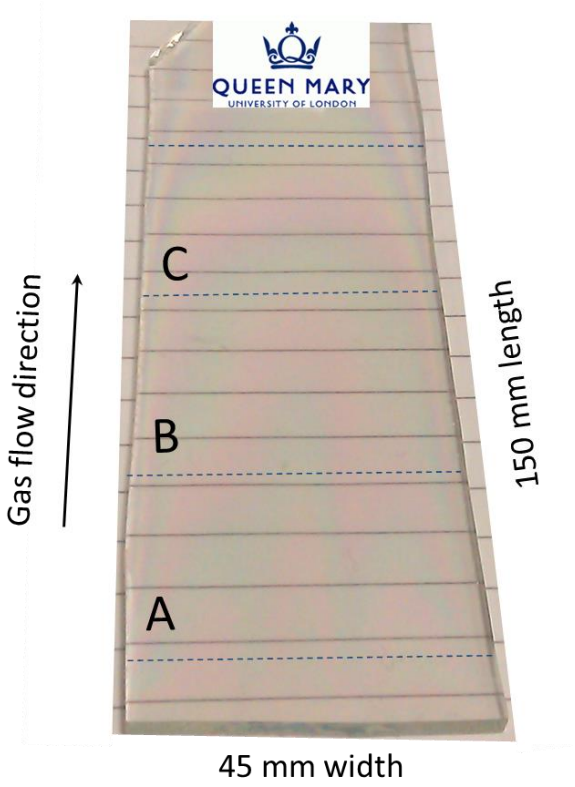

Figure 5.1 Photograph showing transparent ZnO:Ga film grown by AACVD on glass substrate.

In general, two deposition mechanisms, surface reaction kinetics limited or mass transport limited mechanism, exist in CVD process depending on the operating temperature.[33] In the case of control by surface reaction kinetics, the reaction occurs slowly because of the low deposition temperature and the reactants could reach the substrate surface with ease. When the process is limited by mass-transport phenomena, the decomposition occurs more rapidly since the temperature is higher and any molecule that reaches the surface reacts instantly.[17,33] Thus, we could infer that, under a growth temperature of 350 ℃ and 400 ℃, our chemical reaction is

largely surface reaction kinetics limited. So the precursor molecules have sufficient lifetime to migrate to the central part of glass substrate, where it holds an isothermal region in the flowing chamber [145] and could favour the film nucleation and growth, resulting in a less resistant area B. By comparison, the reaction at 450 ℃ could turn into a mass transport limited process, where the gas molecules are absorbed and reacted on the substrate rapidly after they enter into the reactor. As a result, the deposit materials in area A are more conductive than that of the rest on glass surface. In both case, samples on the most conductive areas were selected for materials characterization.

5.3 Results and discussion for ZnO:Ga films prepared with various Ga content

Film composition

The surface elemental analysis of AACVD ZnO and ZnO:Ga films with different Ga content was carried out by using XPS and the spectra are presented in Fig. 5.2. The survey spectra of studied samples indicate the presence of carbon, oxygen, zinc and gallium photoelectron and Auger signals. No other elements were detected in appreciable amounts. After a few minutes of Ar^+ etching, carbon signals were significantly reduced, indicating thus that contamination was mainly limited to the sample surface.

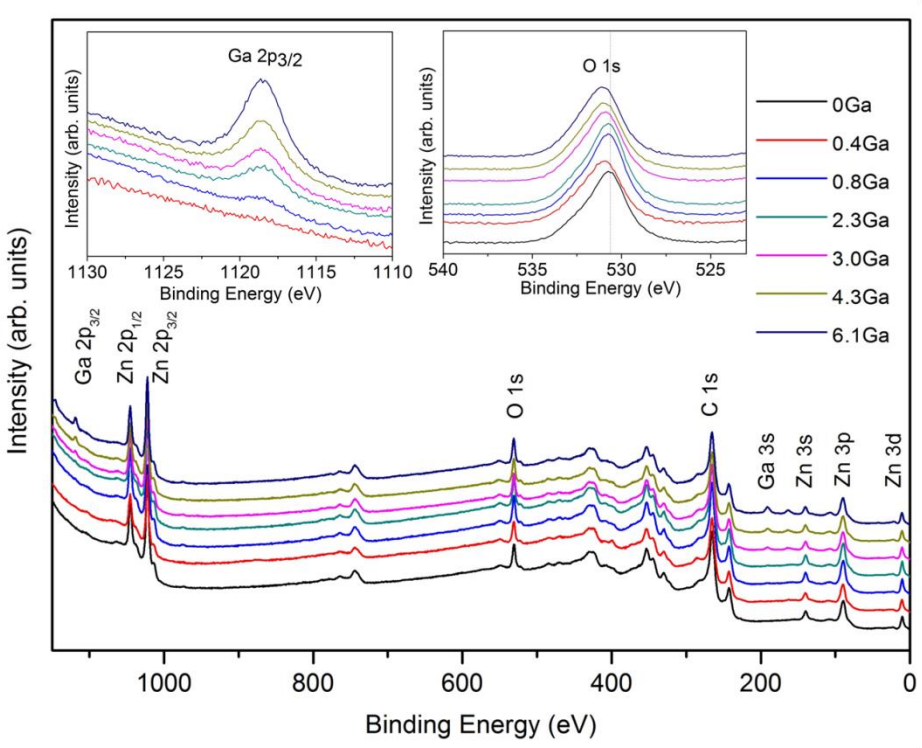

Figure 5.2 Wide-scan XP spectra of AACVD ZnO and ZnO:Ga films with various Ga contents. The insets show the Ga $2p_{3/2}$ and O 1s XP bands.

Irrespective of the specific processing conditions, Zn $2p_{3/2}$ peak positions (average BE = 1021.3 eV) pointed out the presence of Zn(II) in ZnO environment. This indication could be confirmed by the analysis of the Zn LMM Auger signal and the calculation of the corresponding Auger parameters [α_{Zn} = BE(Zn $2p_{3/2}$) + KE(Zn LMM) = 2010.4 eV] further verify this indication.[120,121] The insets of Fig. 5.2 display high-resolution Ga $2p_{3/2}$ and O 1s photoelectron signals. The Ga $2p_{3/2}$ peak position and shape indicate the presence of Ga(III) in an oxide environment.[122,123] In addition, the intensity of the Ga $2p_{3/2}$ signal is monotonically enhanced with an increase of gallium dopant content, indicating a progressive enhancement of Ga content in the obtained systems (compare Table 5.3). Regarding oxygen, the main peak is centred at 530.1 eV, in agreement with the position expected for O in ZnO lattice.[146] The asymmetry of

the O1s signals on the high BE side at ≈531.8 eV suggests the co-presence of hydroxyl groups.[120,121] Moreover, it is seen that an increase in the Ga content in the specimens produced a concomitant chemical shift to higher BEs of the main O 1s component. This phenomenon can be attributed to the fact that Ga atoms are bonded more strongly to oxygen, as the Ga-O covalent bond length is smaller than that of Zn-O.[54,125] Due to the low gallium loading, the Ga $2p_{3/2}$ peak signal in the first doped sample was undetectable by XPS measurement and the Ga atomic content in other five ZnO:Ga films can be calculated at 0.8 at.%, 2.3 at.%, 3.0 at.%, 4.3 at.% and 6.1 at.%, respectively. In spite of this, I can still estimate its content to be approximately 0.4 at.% based on a linear relationship between the nominal Ga/Zn molar ratio in precursor solutions and the final gallium content in films, as illustrated in Fig. 5.3. The details of the film elemental composition are listed in Table 5.3.

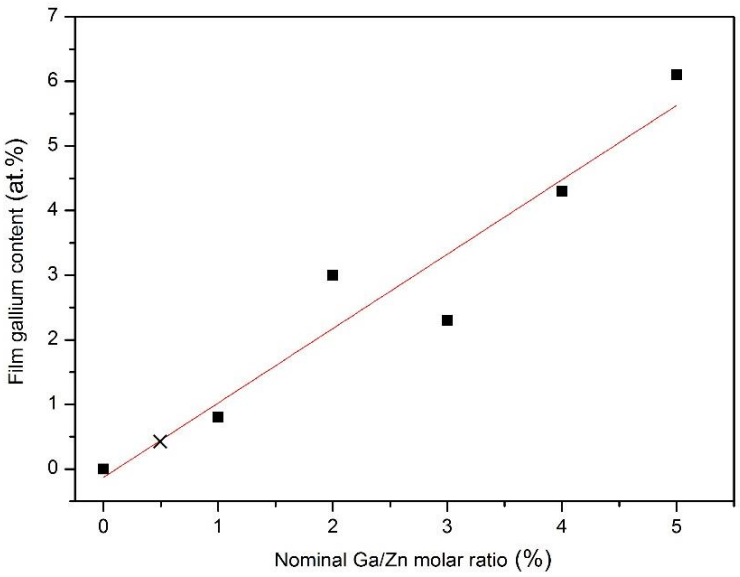

Figure 5.3 Evolution of the film gallium content as a function of the nominal Ga/Zn molar ratio in precursor solution.

Table 5.3 Chemical compositions and structure parameters of AACVD deposited ZnO and ZnO:Ga films with various Ga contents derived from XPS, SEM, XRD and AFM data.

Sample I.D.	Elemental composition by XPS [at.%]			Film thickness	*TC*(*hkl*)					Lattice constant *a*	Lattice constant *c*	Surface roughness
	Zn	O	Ga	[μm]	(002)	(101)	(102)	(103)	(112)	[Å]	[Å]	[nm]
ZnO	46.9	53.1	0	0.76	3.51	0.03	0.30	1.05	0.12	3.2504	5.2082	13.5
ZnO:Ga(0.4)	42.2	57.8	Not detected	0.41	3.01	0.09	0.58	1.03	0.28	3.2501	5.2101	8.2
ZnO:Ga(0.8)	46.1	53.1	0.8	0.49	2.78	0.13	0.77	0.98	0.34	3.2518	5.2107	28.2
ZnO:Ga(2.3)	46.2	51.5	2.3	0.72	2.66	0.14	0.91	0.90	0.39	3.2511	5.2102	36.8
ZnO:Ga(3.0)	45.4	51.5	3.0	0.48	2.01	0.29	1.12	0.94	0.63	3.2504	5.2067	14.1
ZnO:Ga(4.3)	43.9	51.8	4.3	0.51	1.54	0.70	1.36	0.79	0.62	3.2527	5.2063	7.1
ZnO:Ga(6.1)	41.8	52.1	6.1	0.49	0.68	1.27	1.61	0.68	0.76	3.2530	5.1921	4.6

Table 5.4 Electrical and optical parameters of AACVD deposited ZnO and ZnO:Ga films with various Ga contents.

Sample I.D.	Carrier concentration	Carrier mobility	Resistivity	Resistance	Doping efficiency	$T_{\lambda 380-780}$	Plasma wavelength	$R_{\lambda 2500}$	Band gap
	[$\times 10^{20}$ cm^{-3}]	[cm^2 $V^{-1}s^{-1}$]	[$\times 10^{-2}$ Ω cm]	[Ω sq^{-1}]	[%]	[%]	[nm]	[%]	[eV]
ZnO	0.20	25.0	1.28	168.9	-	84.6	-	-	3.14
ZnO:Ga(0.4)	0.80	4.8	1.62	395.6	63.9	85.3	-	-	3.19
ZnO:Ga(0.8)	1.70	2.6	1.42	289.4	68.2	83.4	2440	17.5	3.27
ZnO:Ga(2.3)	3.55	0.9	1.92	266.8	45.0	83.6	1825	41.1	3.39
ZnO:Ga(3.0)	4.22	1.3	1.16	241.9	42.4	84.7	1670	48.9	3.40
ZnO:Ga(4.3)	3.60	0.6	2.97	582.4	25.6	84.5	1920	35.0	3.42
ZnO:Ga(6.1)	1.14	0.1	57.57	11749	5.8	84.7	2380	18.6	3.37

Structural properties

Crystal structures of AACVD ZnO and ZnO:Ga films with various doping contents were analysed by GIXRD. As shown in Fig. 5.4, all the reflection signals can be matched to the standard diffraction pattern of hexagonal wurzite phase ZnO (JCPDS 36-1451).[124] Moreover, the pure ZnO exhibits a very strong *c*-axis texture and the introduction of gallium dopants weakens this texture to some degree. This indicates the growth of (002)-oriented crystals is less favoured in doped samples. The (002) peak still dominates in the patterns of ZnO with Ga content lower than 2.3 at.%. Further addition of gallium atoms to 3.0 at.% results in a reduction of peak intensity associated with emergence of new peaks, such as (100) and (110). The film crystallinity of heavily doped ZnO:Ga(4.3) and ZnO:Ga(6.1) sample is quite poor and the crystallites are more randomly oriented.

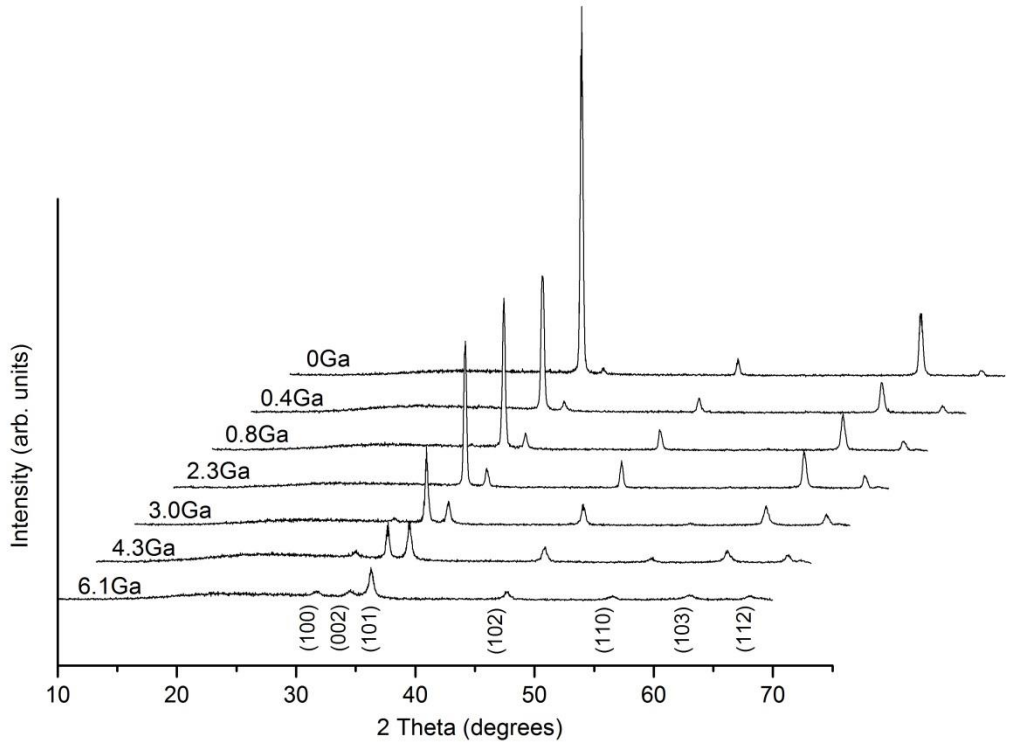

Figure 5.4 XRD patterns of AACVD ZnO and ZnO:Ga films with various Ga contents.

In order to attain a deeper insight into the texturing phenomenon, texture coefficient, *TC*(*hkl*), was introduced to estimate the film orientation degree by using equation (5-1):[147]

$$TC(hkl) = I(hkl)/Io(hkl)]/[\frac{1}{n}\sum_n I(hkl)/Io(hkl)] \quad (5\text{-}1)$$

Where *I*(*hkl*) is the measured relative intensity of (*hkl*) planes, I_0(*hkl*) is the homologous standard intensity of ZnO, *n* is the number of diffraction peaks considered. In general, the crystallites grow preferentially along the (*hkl*) direction only if the corresponding *TC*(*hkl*) value is above 1, and a value greater than 3 is considered to demonstrate significant preferred orientation.[54] The calculated texture coefficient results for present films are summarized in Table 5.3. As observed, pure ZnO exhibits a high (002) texture coefficient of 3.51, representing a significant *c*-axis preferred orientation, and this value decreases continuously from 3.01 in ZnO:Ga(0.4) to 2.01 in ZnO:Ga(3.0), which is mainly compensated by an enhanced texture coefficient in (102) plane. Further increase of Ga atoms would suppress the (002) plane growth greatly and the preferred orientation is changed to (102) in ZnO:Ga(6.1).

The lattice parameters, *a* and *c*, of hexagonal ZnO and ZnO:Ga films are also listed in Table 5.3. Among five strong *c*-axis oriented samples, the *c* value in pure ZnO is lower than that of others except for the ZnO:Ga(3.0). This result might be apparently surprising because Ga^{3+} has a smaller ionic radius with respect to Zn^{2+}, whereby the substitution of Zn^{2+} with Ga^{3+} at lattice sites could decrease the lattice constant.[125] The first possible reason could due to the presence of high oxygen vacancy density in pure ZnO causing lattice distortion and decreasing the interplanar spacing.[148,149] The existence of oxygen vacancies is indeed demonstrated by the

analysis of film electrical properties, where the ZnO obtains a carrier density of 0.2×10^{20} cm^{-3}. The other more likely reason is the existence of interstitial gallium atoms in ZnO lattice, which expands the lattice parameters considerably.[150] Also this kind of defect is hard to avoid under a non-vacuum deposition condition. Therefore, larger *c*-axis lattice constants are observed in ZnO:Ga(0.4) to ZnO:Ga(2.3) compared with pure ZnO. A further increase of Ga content to 3.0 at.% starts suppressing the *c*-axis oriented crystal growth, in other words, the ZnO cells are constrained along *c*-axis, so the lattice parameter *c* decreases to 5.2067 Å. For ZnO:Ga(4.3) and ZnO:Ga(6.1), their *c*-axis oriented crystal growth are heavily inhibited, resulting in a minimum *c* value of 5.1921 Å. Also the general larger lattice parameter *a* in doped samples could due to the reduction of oxygen vacancies and the existence of interstitial gallium atoms.

The interplay between Ga loading and film morphology is illustrated by the SEM images in Fig. 5.5. Fig. 5.5(a) shows that the pure ZnO is composed of uniform regular grains (~100 nm in diameter), with hexagonal faces parallel to the substrate, although not so obvious as those in ZnO nanorods.[151] After adding 0.4 at.% Ga, the hexagonal grains disappear and turn into 60-120 nm granular particles (Fig. 5.5(b)), and then transform into irregularly shaped platelets in ZnO:Ga(0.8) (average grain size ~200 nm, Fig. 5.5(c)). Agglomerated particles exhibit in the sample with 2.3 at.% Ga (average grain size ~150 nm, Fig. 5.5(d)) and the ZnO:Ga(3.0) film morphology is largely wedge-like in shape (200-350 nm in length and 90-150 nm in width, Fig. 5.5(e)). Further Ga addition appears to suppress the grain growth and refined particles (< 50 nm in diameter) are observed both in ZnO:Ga(4.3) and ZnO:Ga(6.1), as shown in Fig 4.5(f)-(g), a phenomenon which correlates with the reduced peak intensities in their XRD patterns. It is also worth mentioning that both

pure ZnO and samples with a low doping level (0.4-3.0 at.%) exhibit typical columnar grain structure, as seen from their cross-section SEM images in Fig. 5.6(a)-(e), while the ZnO:Ga(4.3) and ZnO:Ga(6.1) are more likely thickened by overlapped particles without any evidence of macro-texture (see Fig. 5.6(f)-(g)), indicating that coalescence processes are largely suppressed.

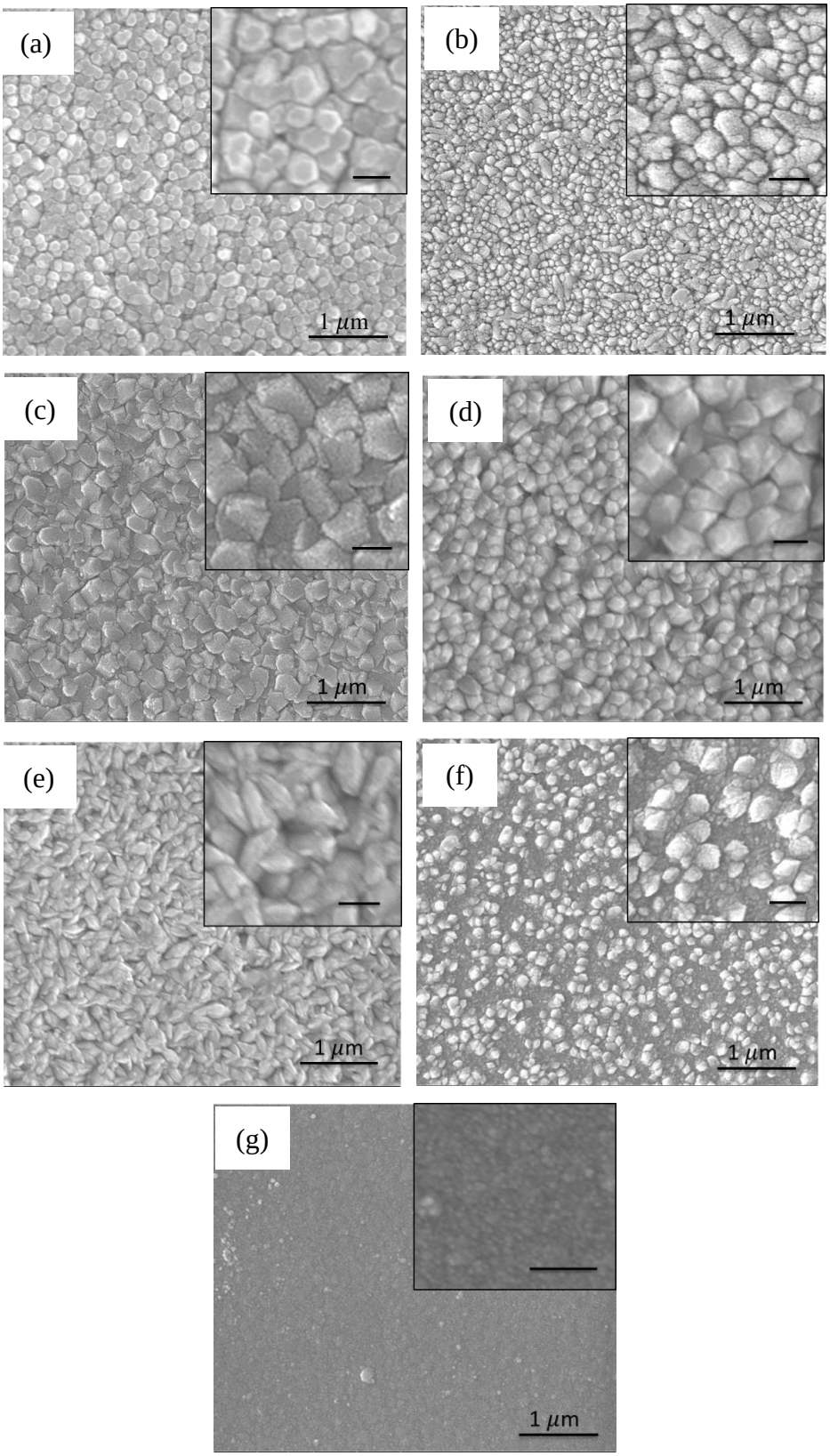

Figure 5.5 Plane-view SEM micrographs of (a) ZnO, (b) ZnO:Ga(0.4), (c) ZnO:Ga(0.8), (d) ZnO:Ga(2.3), (e) ZnO:Ga(3.0), (f) ZnO:Ga(4.3) and (g) ZnO:Ga(6.1) films. The insets show higher magnification images for each sample and the scale bar inside corresponds to 200 nm.

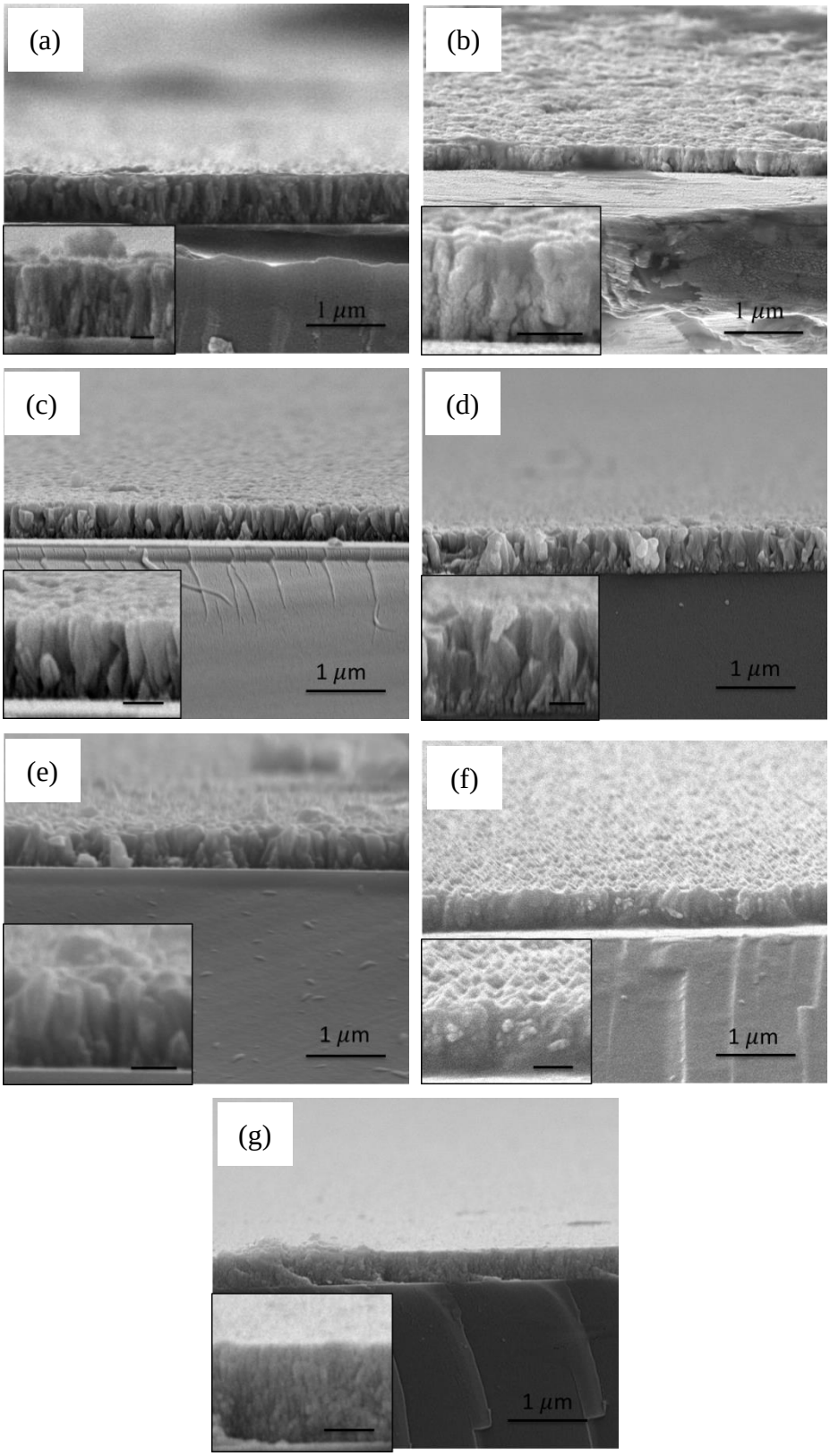

Figure 5.6 Cross-sectional SEM images of (a) ZnO, (b) ZnO:Ga(0.4), (c) ZnO:Ga(0.8), (d) ZnO:Ga(2.3), (e) ZnO:Ga(3.0), (f) ZnO:Ga(4.3) and (g) ZnO:Ga(6.1) films. The insets show higher magnification images for each sample and the scale bar inside corresponds to 250 nm.

The film crystallization likely occurs through sequential nucleation, initial growth and coalescence processes. Texture can be formed already in the first nucleation stage, driven by surface energy minimization, or developed in the subsequent growth because only grains with lower surface energy can survive during the coalescence process.[152] In pure ZnO, the polar (002) planes have higher surface energy, so the fastest crystal growth rate is usually along the *c*-axis to reduce the (002) facet areas as well as the system energy.[153] Moreover, only those [002]-oriented crystallites with their *c*-axis orientation normal or near normal to the underlying substrate could grow all the way upwards, all differently oriented crystals stop their growth at earlier stages, resulting in columnar grain features and strong (002) texture.[154] The surface morphology of crystalline films is also affected by the preferred growth direction but in many cases they are more related to the exposed crystal planes. For instance, *c*-axis oriented ZnO films could preserve a hexagonal surface feature with their (002) planes exposed or exhibit a pyramidal structure by exposing the (101) planes, whose normal direction is 62 ° deviated from that of the basal (002) planes.[96] The introduction of extrinsic doping atoms could greatly influence the ZnO film growth as well as the resulting morphology. On the one hand, the dopant atoms could alter the surface energy of crystallographic planes. For example, Liu *et al.* reported the growth of the *a*-axis-oriented (100) plane is more active than the growth of the *c*-axis-oriented (002) planes in ZnO:F films due to F^- anions filling O vacancies or substituting O sites.[155] This phenomenon would promote the growth of wedge-like grains parallel to the substrate rather than columnar ones.[156] On the other hand, the dopant impurities are prone to segregating at the non-crystalline grain boundary areas, especially when the doping content suppresses its saturation point in

ZnO, and drag the grain boundary movement, which reduce the grain size as well as the film crystallinity.[32,157]

For the pure ZnO sample, its pronounced columnar grains and strong (002) texture represent the microstructure evolution process have been fully developed. Also the observed hexagonal surface feature suggests the growth rate of ingrain and grain boundary areas are identical along the film thickening direction. For the coatings with a low doping level (0.4 at.% to 3.0 at.%), their highly *c*-axis oriented textures in Fig. 5.6 (b)-(e) indicate (i) the (002) planes still hold much higher surface energy and growth rate than the others under the given gallium content, and (ii) the film coalescence processes are also greatly developed in these samples. In spite of this, the enhanced (102) texture coefficient suggests the incorporation of Ga atoms in ZnO lattice may increase the surface energy of (102) facets and populate their growth. A similar phenomenon has also been reported in Ga-doped ZnO nanowires, where the wire growth direction was changed from [001] direction in pure ZnO to [102] in ZnO:Ga samples.[158] Thus, the *c*-axis textures are less significant in doped coatings and also weaken with increasing gallium content. Moreover, the grain boundary growth in ZnO:Ga samples would be retarded compared with the ingrain areas, resulting in the disappearance of hexagonal grains and the exposure of other low-index facets. These non-[002] oriented surfaces, which are formed at the final deposition stage, could successfully avoid to be incorporated into the columnar grain structure. It is likely that Ga will preferentially move to the polar (002) surfaces as a way of charge compensation in the crystal. This will also contribution to the retardation of growth in this direction. But in order to identify which exact facets are exposed in ZnO:Ga(0.4) to ZnO:Ga(3.0), cross-section TEM investigation is required in my future work. When the Ga content exceeds 4.3 at.%, the segregation of gallium

atoms at grain boundaries become pronounced and suppress the grain growth greatly. So the [002]-oriented crystallites can no longer overgrow other crystallites with different orientations during the film thickening, leading to an obvious reduction in (002) peak intensity as well as the disappearance of a columnar texture structure. Also the obtained [102] preferential orientation in ZnO:Ga(6.1) should originate from a preferred nucleation in the early growth stage as the heavy doping inhibits all the crystallites growth significantly and refined grains are observed in this sample. The coarse grain boundaries, with amorphous-like contrast to the grain interiors, in its HRTEM image (Fig. 5.7) could verify the segregation of dopant atoms in ZnO:Ga(6.1). The doping dependent CVD ZnO film growth behavior is schematically illustrated in Fig. 5.8.

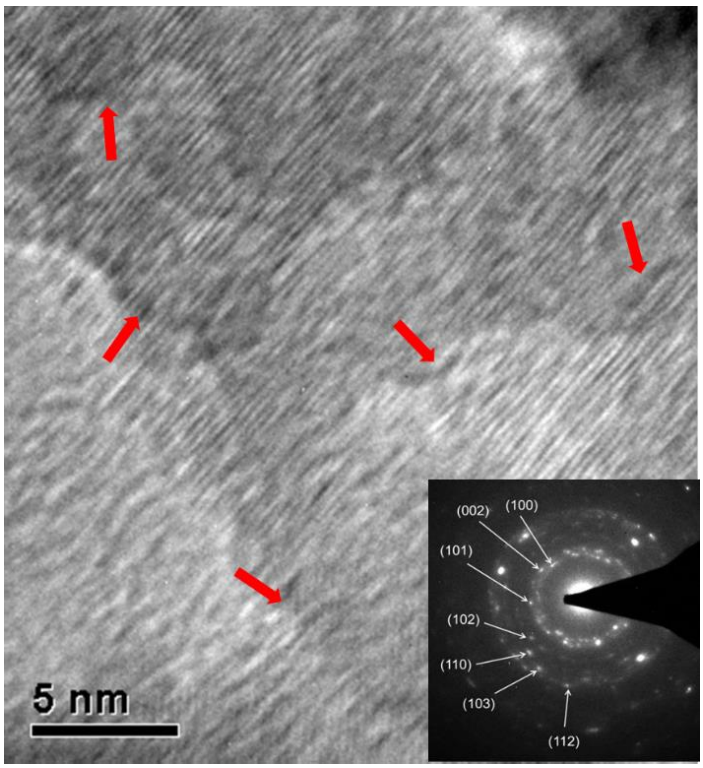

Figure 5.7 Bright field HRTEM images of the nanograins in ZnO:Ga(6.1). The inset shows the selected area electron diffraction pattern and the red arrows refer to grain boundary areas.

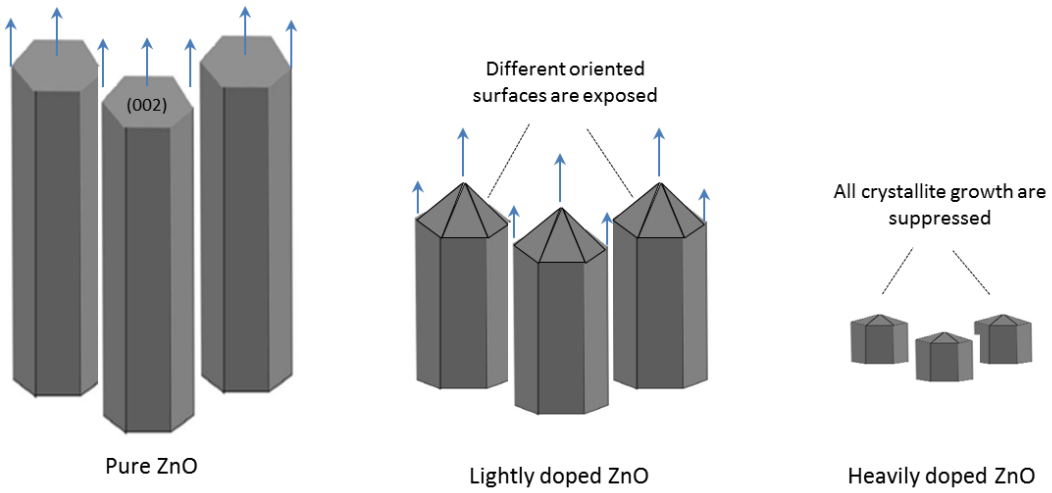

Figure 5.8 Schematic illustration of the growth behaviour in pure and doped ZnO film.

Electrical properties

The electrical parameters, including resistivity, Hall mobility and carrier concentration, of the AACVD ZnO and ZnO:Ga films with doping content ranging from 0.4 at.% to 6.1 at.% were determined by Hall effect measurements *via* the van der Pauw method. The results presented in Table 5.4 show that all the films were *n*-type semiconductors and that Ga introduction has a limited influence on the film resistivity, while a large variation in the carrier density and mobility exists between the undoped and doped ZnO samples.

The pure ZnO film has a carrier concentration of 0.2×10^{20} cm^{-3} and these charge carriers are expected to be oxygen vacancies since the films are deposited under an oxygen-deficient atmosphere. The addition of Ga atoms enhances ZnO carrier density to a range of 10^{20} cm^{-3}. As the Ga content increased, the concentration of charge carriers show a rapid enhancement from 0.8×10^{20} cm^{-3} in ZnO:Ga(0.4) to 4.22×10^{20} cm^{-3} in ZnO:Ga(3.0), and then a gradual decrease to 1.14×10^{20} cm^{-3} at higher Ga loadings. These concentration values are quite high but lower than the previously reported values in APCVD ZnO:Ga films (up to 10.6×10^{20} cm^{-3}).[59] The

electron carriers in gallium-doped ZnO films are generated by substituting Zn^{2+} ions with Ga^{3+} ions, and this substitution efficiency is essential for the film electrical performance because those inactive doping atoms, such as interstitial gallium atoms, cannot generate free electrons but act as electron scattering centres.[156] In equation (5-2), the doping efficiency (η_{DE}) is defined as the ratio of the electron concentration to the Ga atomic concentration in ZnO:Ga films under an assumption that every incorporated Ga cation provides one free electron with substitution of a Zn ion:[156,159]

$$\eta_{\mathrm{DE}} = \frac{N_e}{\rho N_{\mathrm{A}} c/M} \tag{5-2}$$

Where N_e is the electron concentration, ρ is the film density, N_A is the Avogadro constant, c is the Ga atomic ratio, M is the molecular weight. In my calculation, the ZnO:Ga films are assumed to have the density of 5.606 g cm^{-3}, similar to that of the bulk ZnO.[156] The calculated doping efficiency are 51.8 % 53.4 %, 39.6 %, 36.7 %, 22.6 % and 5.3 % respectively in ZnO:Ga(0.4) to ZnO:Ga(6.1), which could be insufficient to guarantee a good carrier mobility performance.

A high carrier mobility of 25.0 $cm^2 V^{-1}s^{-1}$ can be observed in pure ZnO and this is easy to appreciate that scattering by the carriers is limited. After the Ga atoms are introduced, the mobility values decrease dramatically. Upon enhancing Ga content, the mobility in ZnO:Ga samples declines gradually from a maximum value of 4.8 $cm^2 V^{-1}s^{-1}$ in ZnO:Ga(0.4) to a lowest value of 0.1 $cm^2 V^{-1}s^{-1}$ in ZnO:Ga(6.1). It is known that the mobility of free carrier is determined by the electron scattering arising mainly from grain boundaries, ionized impurities and neutral impurities in doped ZnO films.[61] The dominance of the scattering effects varies with the carrier density and the potential barrier at the grain boundary has been considered to be

negligible when the carrier concentration is superior to 10^{20} cm^{-3}.[46] Moreover, the ionized impurity scattering cannot be the only dominant mechanism in my case because even more charge carriers are generated by ionized impurities in APCVD ZnO:Ga films, their mobility (~10-25 $cm^2 V^{-1}s^{-1}$) could still one order higher than my results.[59] Thus, the inferior mobility performance in present samples could mainly result from an insufficient doping efficiency, where many inactive dopant atoms locate in the ZnO lattice as interstitial defects or segregate at grain boundary areas as neutral impurities. In Fig. 5.9, the charge carrier mobility is plotted versus the carrier density and doping efficiency for the studied coatings. It is seen that the mobility values depend linearly on the doping efficiency, and a similar trend is also observed with respect to carrier density, except for the most heavily doped sample ZnO:Ga(6.1). This indicates the dominant electron scattering mechanism is transformed from a combined ionized and neutral impurity scattering in ZnO:Ga(0.4) to ZnO:Ga(4.3) to the neutral impurity scattering only in ZnO:Ga(6.1).

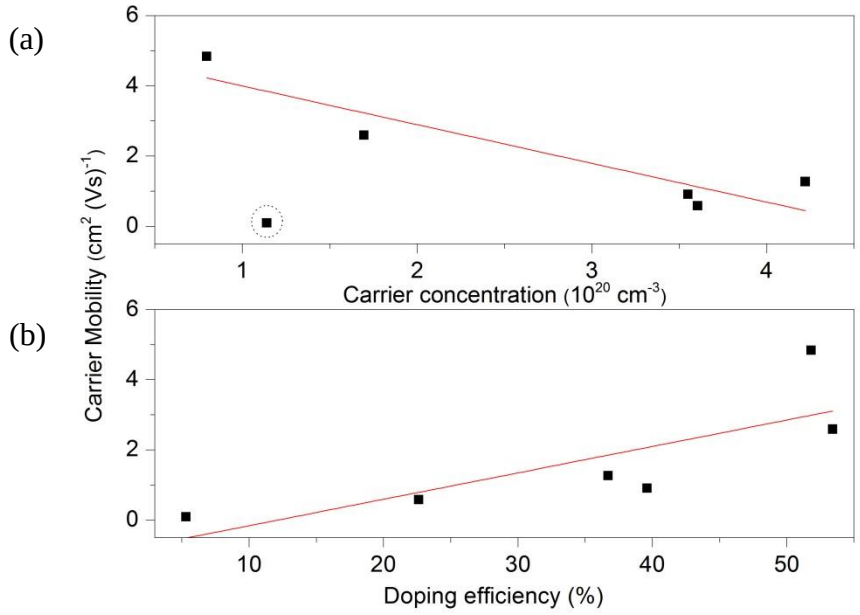

Figure 5.9 The carrier mobility as a function of (a) carrier concentration and (b) doping efficiency for ZnO:Ga films. The dash circle marks the sample deviating from the linear trend.

Through a combination of carrier concentration and mobility, a lowest resistivity value of 1.16×10^{-2} Ω cm was obtained in ZnO:Ga(3.0) film with an estimated carrier density 4.22×10^{20} cm^{-3} and mobility 1.27 cm^2 $V^{-1}s^{-1}$. Due to the inferior mobility performance, my film resistivity is two order of magnitude higher than previously reported highly conductive ZnO:Ga film.[59] In spite of this, these coatings could still have a potential application in energy efficient glazing for which, according to my observation, the carrier density is the most important electric parameter rather than resistivity, though clearly they are related.

Optical properties

Fig. 5.10 shows the optical transmittance of the AACVD ZnO and various ZnO:Ga films from 300 nm to 2500 nm and the reflectance of selected ZnO:Ga samples from 1000 nm to 2500 nm. It is seen that the ZnO:Ga coatings exhibit high transparency across the visible lights (> 80 % transmission including the substrate absorbance, see Table 5.4) and good reflectivity in the near-infrared range (up to 48.9 % reflection at 2500 nm). The films also display prominent interference fringes, which are caused by the multiple reflections at the three interfaces of the air/film/substrate bilayer,[89] and the transmission of doped samples reduces rapidly in the near infrared region, compensated by a continuous reflection enhancement after a certain wavelength.

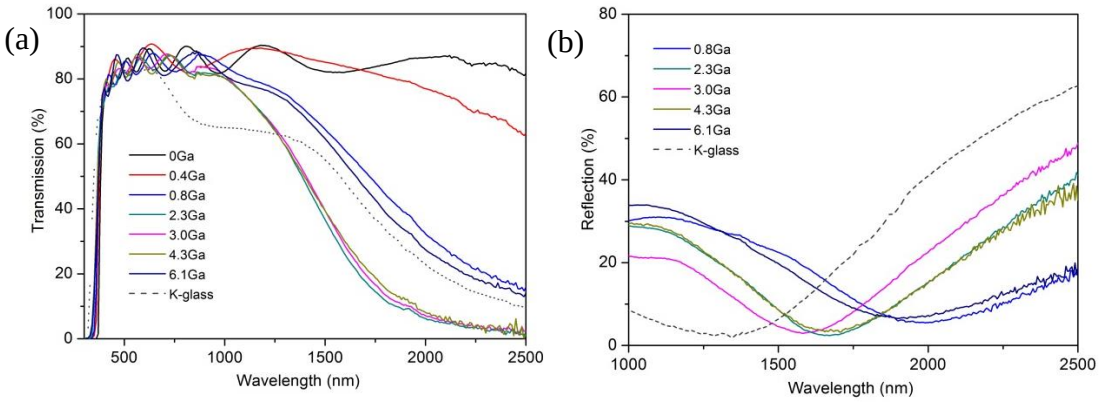

Figure 5.10 (a) Optical transmission spectra of AACVD ZnO and various ZnO:Ga films. (b) Optical reflection spectra of selected ZnO:Ga films.

The calculated average transmittance in the visible light region (380 nm to 780 nm) of pure ZnO and ZnO:Ga films are 84.6 %, 85.3 %, 83.4 %, 83.6 %, 84.7 %, 84.5 % and 84.7 %, respectively, thus a majority of visible light could transmit through the coatings. The minor light loss in TCO films is expected to mainly depend on the light scattering as a function of grain size, surface roughness and the level of defects.[160,161] Among the studied coatings, a high visible transmission value of 84.7 % can be observed in ZnO:Ga(6.1) even though a greater number of boundary areas is existed in this sample because its grain size is much smaller than that of others. This indicates the grain boundary light scattering is unlikely to be the main reason for visible light loss. Furthermore, the transmittance of pure ZnO and ZnO:Ga(3.0) are basically same despite their large difference in carrier density, representing the carrier scattering effect is also limited for present samples. Based on this, the obtained lower transmission values in ZnO:Ga(0.8) and ZnO:Ga(2.3) could be due to their rougher surface. This idea can be directly verified by their AFM images in Fig. 5.11, where the most transparent sample ZnO:Ga(0.4) exhibits a low surface roughness of 8.2 nm and this value in ZnO:Ga(2.3) could reach as high as 36.8 nm.

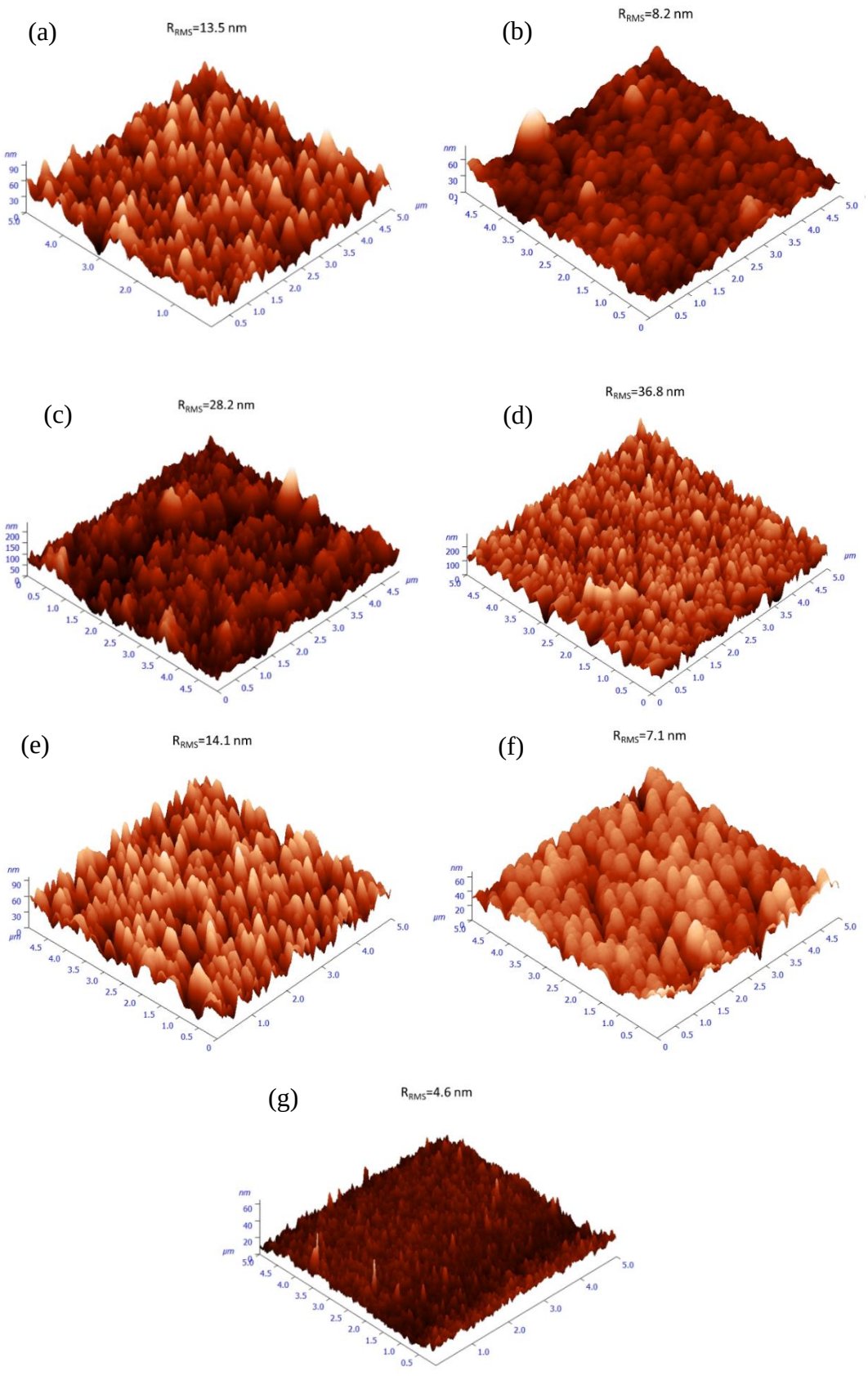

Figure 5.11 AFM images of (a) ZnO, (b) ZnO:Ga(0.4), (c) ZnO:Ga(0.8), (d) ZnO:Ga(2.3), (e) ZnO:Ga(3.0), (f) ZnO:Ga(4.3) and (g) ZnO:Ga(6.1) films.

As discussed in Section 2.2.3.1 (Chapter 2), the reduction of transmittance and increase of reflectivity in near infrared region in ZnO:Ga films are caused by a coherent oscillation of conduction electrons (plasmons) with incident electromagnetic radiation.[162] For low-E application, the plasma wavelength could locate in the middle of near infrared range to avoid influence the visible transmittance (0.4 to 0.8 μm), ensuring at the same time a high reflectance to most thermal infrared radiation (3 to 50 μm). For the fluorine tin oxide coated K-glass, taken as a reference, its plasma wavelength is located around 1860 nm (shown in Fig. 5.12) and a good visible transmittance (82 %) and infrared reflectance (63 % at 2500 nm) are obtained. The plasma wavelength in ZnO:Ga(2.3) to ZnO:Ga(4.3) are 1825 nm, 1670 nm and 1920 nm, respectively, which helps separate the visible and infrared regimes well. Favourable infrared reflectance (35.0 % to 48.9 % at 2500 nm) is also observed in these three high carrier density based samples. This supports the idea again that the coating infrared reflection is mainly governed by the carrier concentration as has been previously noted.[6]

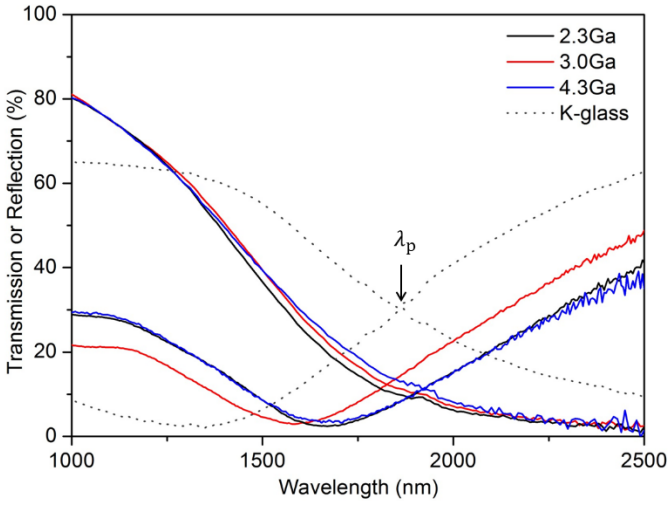

Figure 5.12 Transmission and reflection spectra of ZnO:Ga(2.3), ZnO:Ga(3.0) and ZnO:Ga(4.3) in the near infrared light. The intersection point corresponds to the plasma wavelength.

The optical band gaps of the AACVD ZnO and various ZnO:Ga films were determined by constructing Tauc plots using the $(ahv)^2$ relation.[65] The resulting plots are shown in Fig. 5.13(a) and the corresponding values are listed in Table 5.4. It is seen the band gap of pure ZnO film, 3.14 eV, lower than the reported value of bulk ZnO (3.24 eV) and the introduction of Ga atoms could enhance this band gap obviously with a maximum value of 3.42 eV obtained in sample ZnO:Ga(4.3). Such a band-gap widening phenomenon has been reported in many literatures for doped ZnO and can be explained through the Burstein-Moss effect. Accordingly, the excess free electrons with the addition of donor Ga^{3+} ions would fill the bottom levels of conduction band, thereby leading to an increase in the Fermi level.[7,163,164] This band gap broadening (ΔE_g) is related to the electron concentration N_e through equation (5-3):[165]

$$\Delta E_g = E_F - E_C = \frac{h^2}{8m^*}\left(\frac{3N_e}{\pi}\right)^{2/3} \quad (5\text{-}3)$$

Where $E_F - E_C$ is the energy separation between the Fermi level and the bottom of the conduction band, h is Planck constant. The relationship between $(N_e)^{2/3}$ and ΔE_g for the studied ZnO:Ga films are also ploted in Fig. 5.13(b), where a linear trend can be clearly observed except for the ZnO:Ga(6.1) sample, indicating a corresponding change in the mechanism. It was expected that the bandgap enlargement effect in ZnO:Ga(6.1) should be limited since its carrier density decrease to only 1.14×10^{20} cm^{-3}. The significant bandgap widening occurring for ZnO:Ga(6.1) may relate to its high interstitial gallium concentration, which has been reported to shift the ZnO Fermi level upward into the conduction band.[166]

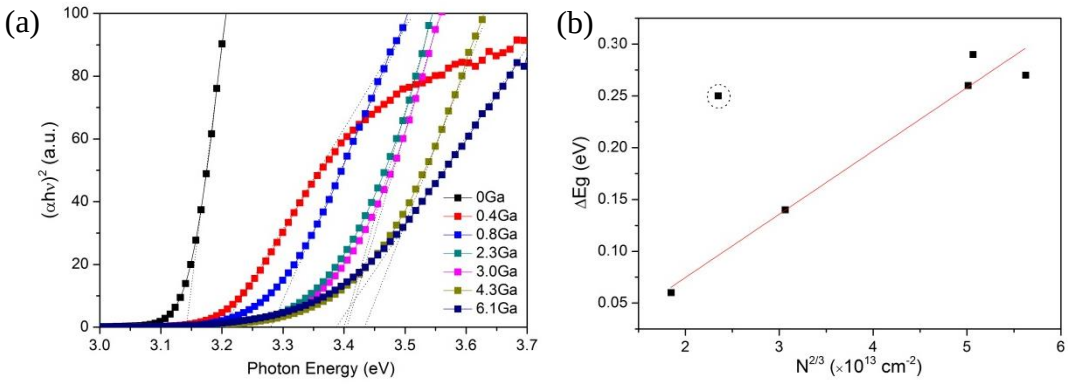

Figure 5.13 (a) Tauc plots of AACVD ZnO and ZnO:Ga films with various Ga contents. (b) The relationship between film carrier concentration and the band gap shift. The dash circle marks the sample deviating from the linear trend.

5.4 Results and discussion for ZnO:Ga films prepared over different deposition temperature and time

Film composition

The surface elemental analysis of ZnO:Ga films prepared over different temperature and thickness was carried out by using XPS and the spectra of two representative samples (B2 and B6) are presented in Fig. 5.14. Their survey spectra indicate the presence of carbon, oxygen, zinc and gallium photoelectron. No other elements were detected in appreciable amounts. Fig. 5.14 also displays the high-resolution Zn 2p, O 1s and Ga 2p photoelectron signals for both samples. The peak positions of Zn $2p_{1/2}$ (BE ≈ 1045.2 eV) and Zn $2p_{3/2}$ (BE ≈ 1022.1 eV) pointed out the presence of Zn(II) in ZnO environment.[120,121] The O 1s main peak is centred at ≈530.4 eV, in agreement with the position expected for O in ZnO lattice,[146] and the Ga 2p peak position indicate the presence of Ga(III) in an oxide environment.[122,123] The Ga atomic content in B2 and B6 are calculated at 0.4 at.% and 2.1 at.%, respectively, representing a higher temperature could absorb more dopant atoms into the deposit.

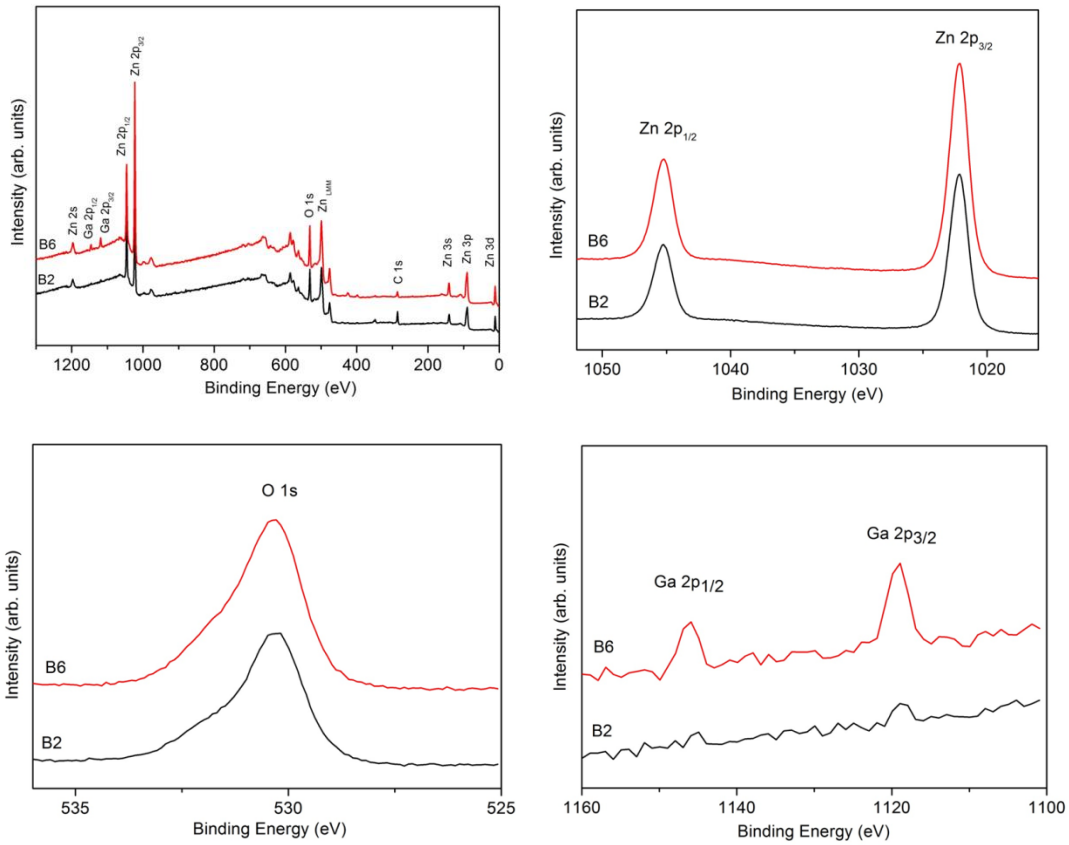

Figure 5.14 Wide-scan and high resolution XP spectra of sample B2 and B6.

Structural properties

Fig. 5.15 shows the XRD patterns of the AACVD ZnO:Ga films prepared with different temperature and thickness. All the diffraction peaks in the patterns correspond to the reflection of ZnO hexagonal wurtzite structure and the (002) peak dominates in all patterns. Moreover, the peak intensity, especially the dominant (002) reflection plane, is enhanced with increasing film thickness. This represents the system crystallinity is being improved. By comparison, the influence of growth temperature on the film quality is less significant.

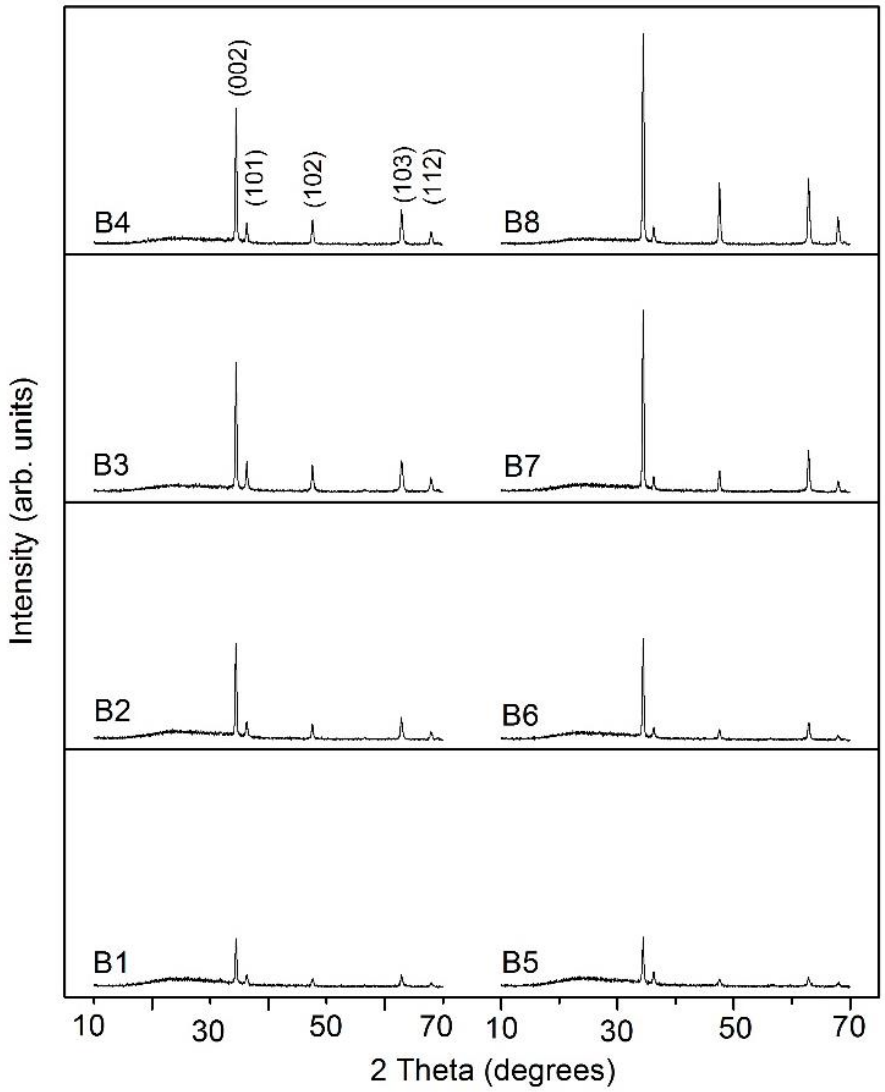

Figure 5.15 XRD patterns of AACVD ZnO:Ga films prepared over different temperature and thickness.

The in-plane and cross-section SEM images of deposited materials are illustrated in Fig. 5.16. At 400 ℃, the film surface morphology are largely wedge-like in shape, with a dimension of 140-350 nm in length and 70-150 nm in width (see Table 5.5). This wedge-shaped crystallites were often observed in atomic layer deposited ZnO, ZnO:Al and ZnO:F films and they were related to *a*-axis growth orientations.[156,167–169] In this case, since no (100) reflection plane is presented in the film XRD patterns, these crystallites could grow along some near *a*-axis orientations, such as [102] or [103]. At a higher deposition temperature 450 ℃, the

film morphology transforms into round-shaped particles, with the average diameter ranging from 100 nm to 250 nm. For thin film deposition, the increase of substrate temperature could speed up the nucleation process to a large extent, so the nucleis have less space to grow and spherical particles are formed in sample B5-B8. Moreover, the size of these nano-structures increases with film thickness, consistent with their improved film crystallinity observed from XRD patterns. The thickness dependent crystallite or particle size has been reported in many ZnO literatures,[7,59,125] which is not hard to understand as the crystallites in thicker films obtain longer growth time. It is noticeable that the thicker ZnO:Ga coatings exhibit pronounced columnar grain structure, as seen from their cross-section images. However, for the thinnest sample B1 and B5, they are more likely thickened by overlapped particles, indicating their microstructure evolution processes have been suppressed. The transition thickness between two growth models is around 280 nm for studied ZnO:Ga coatings.

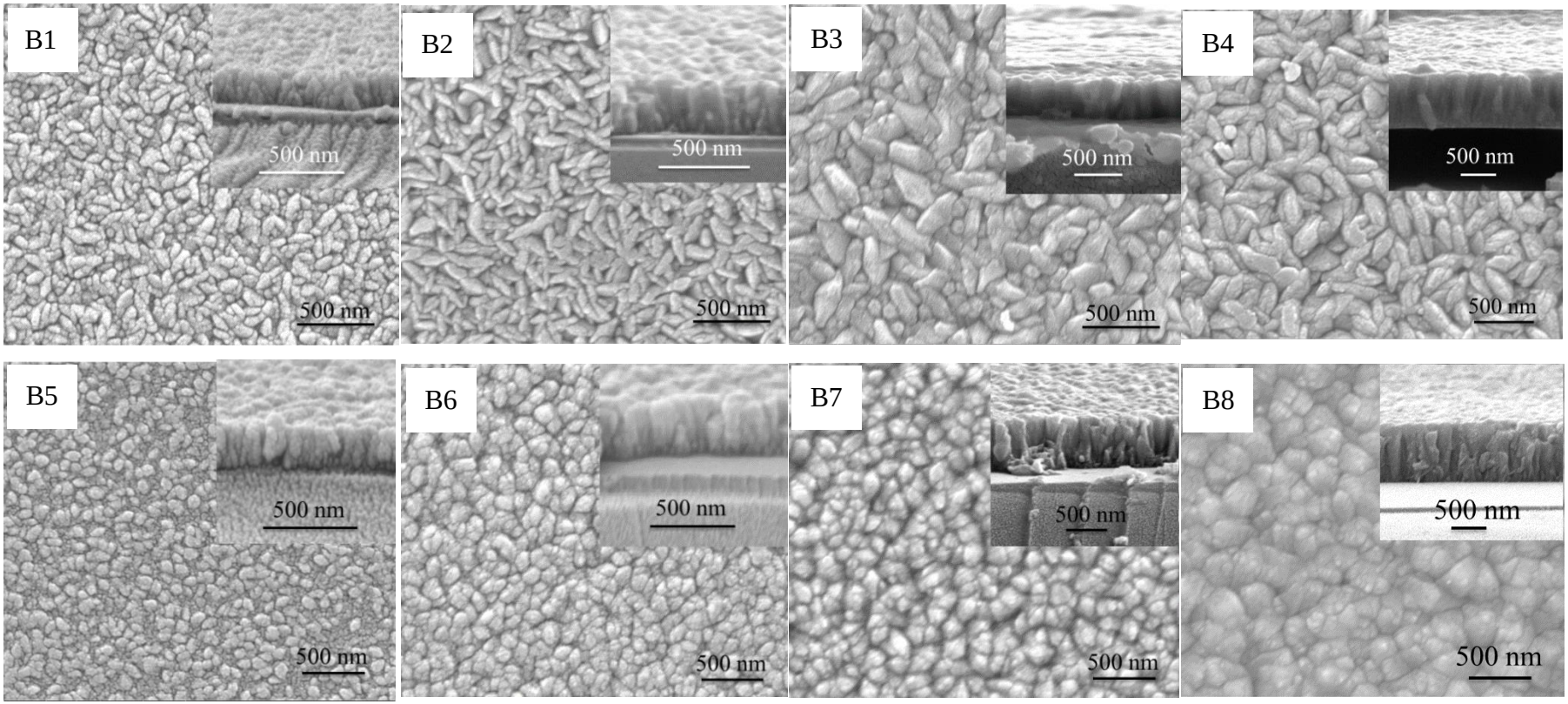

Figure 5.16 SEM images of AACVD ZnO:Ga films prepared over different temperature and thickness.

Table 5.5 Structural, electrical and optical parameters of AACVD ZnO:Ga films prepared over different temperature and thickness.

Sample I.D.	Film thickness	Agglomerate size		Carrier concentration	Carrier mobility	Resistivity	Resistance	$T_{\lambda 380-780}$	$R_{\lambda 2500}$	Surface roughness	Band gap
	[μm]	*L* (nm)	*W* (nm)	[$\times 10^{20}$ cm^{-3}]	[cm^2 $V^{-1}s^{-1}$]	[$\times 10^{-2}$ Ω cm]	[KΩ sq^{-1}]	[%]	[nm]	[nm]	[eV]
B1	0.18	140	70	1.26	0.03	188.6	94.3	88.4	-	7.1	3.31
B2	0.28	210	80	2.52	0.6	4.22	1.50	85.1	-	8.2	3.38
B3	0.50	350	170	2.51	1.6	1.55	0.31	81.5	40.5	15.2	3.38
B4	0.65	340	150	2.79	3.4	0.65	0.10	79.7	42.2	11.6	3.39
B5	0.17	100	100	4.31	0.07	20.8	13.0	82.8	-	6.5	3.42
B6	0.28	120	120	5.28	1.2	1.03	0.38	83.6	-	5.3	3.44
B7	0.51	150	150	4.92	1.3	0.99	0.20	78.9	45.5	14.1	3.42
B8	0.75	250	250	4.10	1.7	0.89	0.12	68.9	37.3	12.7	3.37

Electrical properties

Table 5.5 shows the resistivity, carrier concentration and Hall mobility for the deposited ZnO:Ga coatings. As observed, the film conductivity improves with thickness. The resistivity value in B1 is as high as 1.89 Ω cm and then dramatically decreases to 4.22×10^{-2} Ω cm in B2, followed by a further reduction to a minimum value of 6.5×10^{-3} Ω cm in B4. A similar trend is illustrated in 450 ℃ deposited samples and lowest resistivity is 8.9×10^{-3} Ω cm in B8. In both case, the reduced resistivity with thickness is due to the simultaneous improvement in carrier mobility.

High carrier density, with all values superior to 10^{20} cm^{-3}, is presented in the tested ZnO:Ga coatings. For the samples deposited at 400 ℃, the carrier concentration firstly shows a small increase from 1.26×10^{20} cm^{-3} in B1 to 2.25×10^{20} cm^{-3} in B2 and remains nearly unchanged in the thicker specimen. The initial electron density improvement could be attributed to a large reduction of grain boundary defects, which have been reported to act as electron trap sites in ZnO films.[7] Also the higher electron density in sample B5-B8 (4.10×10^{20} cm^{-3} to 5.28×10^{20} cm^{-3}) indicates a higher heat input could promote the gallium substitution during depositions.

Similarly with the ZnO:Ga samples in Section 4.3, the carrier mobility in the present coatings is still poor, with a maximum value of 3.4 cm^2 $V^{-1}s^{-1}$, which should due to the profound ionized and neutral impurity scattering effects. The mobility is even as low as 0.03 cm^2 $V^{-1}s^{-1}$ and 0.07 cm^2 $V^{-1}s^{-1}$ in B1 and B5, respectively. In these two less crystalline samples, the existence of large non-crystalline areas, such as grain boundaries, brings a huge amount of defects and scattering centres, so their electron mobility is restricted. After the coalescence process happened, the boundary

areas are tremendously reduced and better mobility values (0.6-3.4 cm^2 $V^{-1}s^{-1}$) are observed.

Optical properties

Fig. 5.17 shows the optical transmittance and reflectance of the studied ZnO:Ga films in the solar radiation range (300-2500 nm). It is seen that most coatings exhibit high transparency across the visible light (380-780 nm), with an average transmittance value near or superior to 80 % including the substrate absorbance (see Table 5.5). Moreover, among eight samples, the visible transmission in B8 (68.9 %) is obviously lower than that of others. This may result from its high electron numbers since the surface roughness between concerned ZnO:Ga samples exhibits minor variations (5.3-15.6 nm), as illustrated in Fig. 5.18.

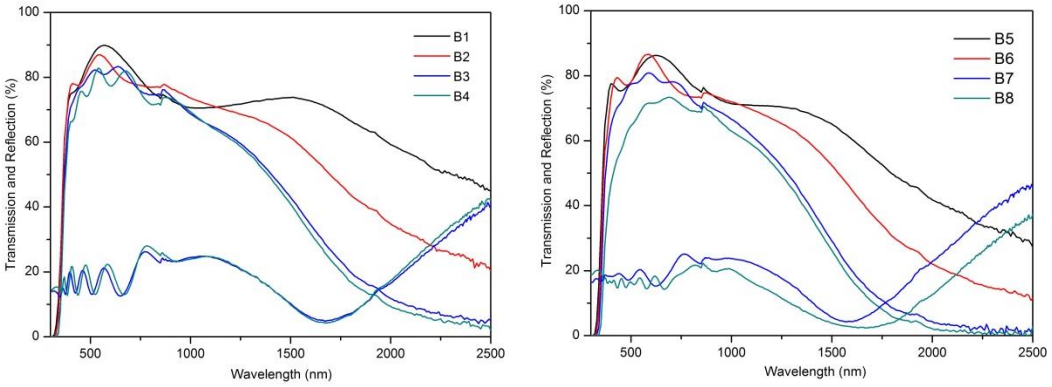

Figure 5.17 Optical transmission and reflection spectra of AACVD ZnO:Ga films prepared over different temperature and thickness.

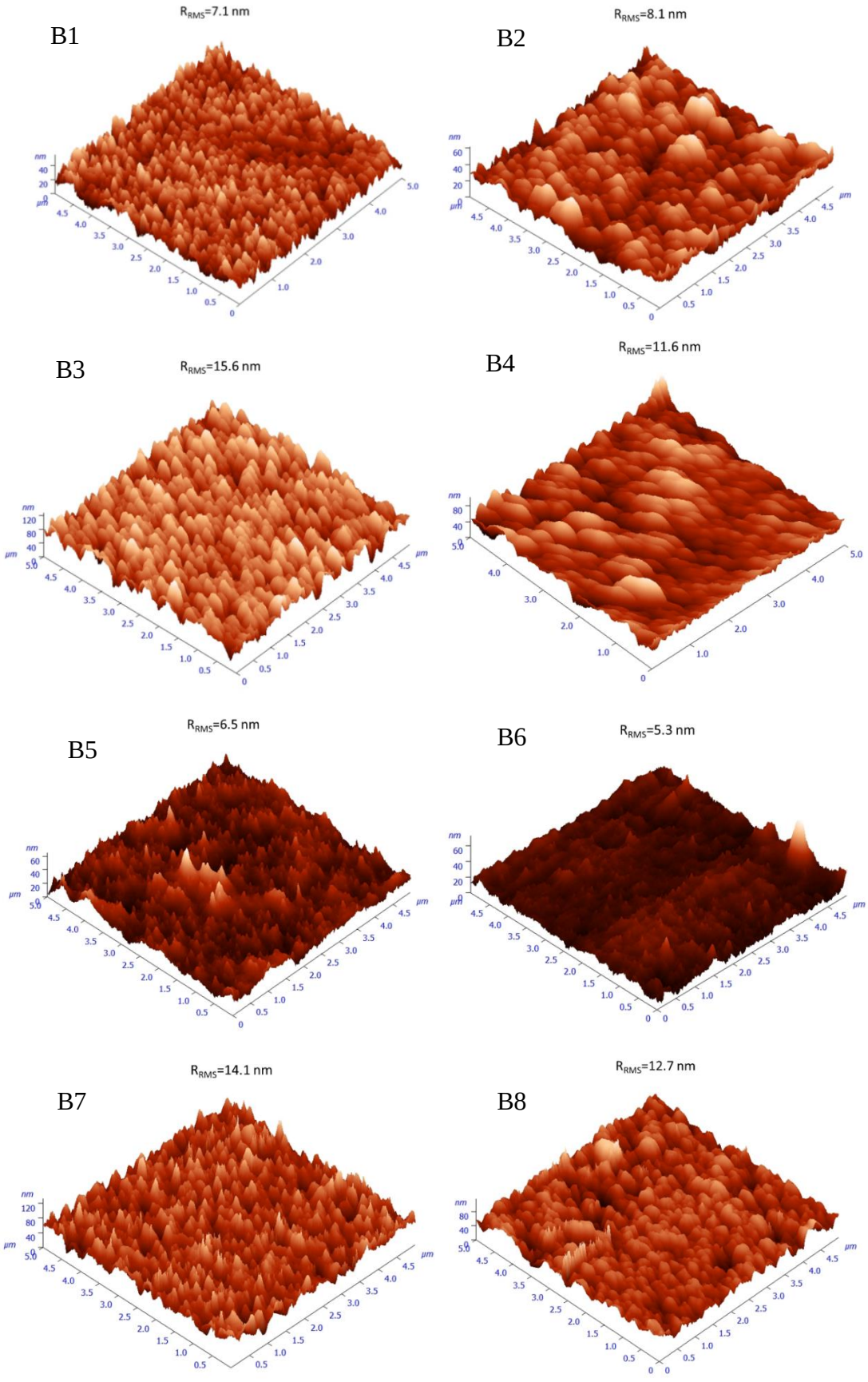

Figure 5.18 AFM images of AACVD ZnO:Ga films prepared over different temperature and thickness.

In the near infrared light region (780-2500 nm), the ZnO:Ga film transmission exhibits a continuous reduction, and this effect is more profound in the thicker samples with their reflectance get enhanced rapidly. According to Table 5.5, even the electron density in B5 could reach 4.31×10^{20} cm^{-3}, it is still unable to induce a rapid plasma reflection in the near infrared region. By comparison, a quick transmittance reduction and reflectance enhancement is observed in B3 and B4, whose carrier densities are obviously lower but hold higher thickness values. Such a thickness dependent reflection phenomenon is also observed in Dong *et al.*'s work, where the 28 nm thick ZnO:Al film remained transparent in the near infrared range (~82 % at 1800 nm) even with carrier concentrations as high as 1.8×10^{21} cm^{-3}. The arising film thickness hardly changed their ZnO:Al carrier density but lowered the infrared transmission. For example, the transmittance values at 1800 nm were ~70 % for the 70 nm coating, ~30 % for the 120 nm film and ~2 % for the 580 nm sample, respectively.[7] These all indicate that high carrier density alone cannot guarantee a good infrared reflectance and the film thickness, more specifically the total number of charge carriers, is also essential. In addition to this, the infrared transmission seems hard to further reduce after the ZnO:Ga thickness surpasses 500 nm, indicating the film reflection cannot linearly increase with the electron numbers after a certain point and then the carrier concentration may turn into the dominant factor.

Finally, the band gap for the present AACVD ZnO:Ga samples were calculated and the corresponding values are listed in Table 5.5. It is seen that all the ZnO:Ga band gaps (3.31 eV to 3.44 eV) are larger than the reported value of bulk ZnO (3.24 eV). The relationship between the bandgap enlargements and the film carrier densities is linearly, as illustrated by the plot in Fig. 5.19. This represents my band gap results can be well explained by the Burstein-Moss theory. [163,164]

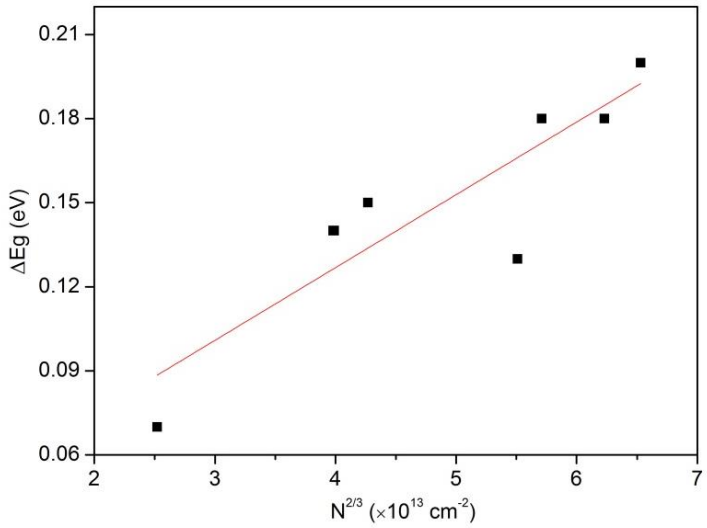

Figure 5.19 The relationship between film carrier concentration and the band gap shift for AACVD ZnO:Ga films prepared over different temperature and thickness.

5.5 Conclusions

In this chapter, Ga-doped ZnO thin films were successfully deposited onto glass substrates by low cost single source AACVD of zinc and gallium acetylacetonates (in methanol). The effects of gallium doping content, deposition temperature and time on the ZnO structural and opto-electronic performances were systematically investigated. The resulting ZnO:Ga coatings exhibited high carrier concentration (up to 5.28×10^{20} cm^{-3}) but limited carrier mobility (< 5 cm^2 $V^{-1}s^{-1}$), and the minimum resistivity value obtained was 6.5×10^{-3} Ω cm. Due to the large band gaps and favourable carrier numbers, high visible transmittance (> 80 %) and infrared reflection (up to 48.9 % at 2500 nm) were observed in these films, which is close to the optical requirements for commercial energy saving glazing. I firstly proved that the film infrared reflectivity was determined by the carrier density and carrier number together.

Chapter 6 AACVD of Surface-Textured Zinc Oxide Films

The following chapter describes the deposition of surface-textured zinc oxide films on FTO and silica glass substrates by using AACVD method utilising inexpensive precursors *i.e.* zinc-acetate-dihydrate, acetic acid and deionized water in methanol. The resulting ZnO films exhibit good visible transparency (~70 %), low sheet resistance (~60 Ω sq^{-1}) and ultra large haze factor (up to 98.5 %), which can be potentially used as the front contact in thin-film solar cells.

6.1 Introduction

In addition to the extraordinary chemical/electrical/optical properties, zinc oxide has been extensively investigated over the last decade because it exhibits unique structural anisotropy, where a variety of extended and oriented nanostructures, such as nanowires, nanorods, nanoplates, nanobelts, nanosheets, *etc.* can be fabricated and incorporated into devices.[146,170] The nonpolar $\{10\bar{1}0\}$, semipolar $\{10\bar{1}1\}$ and polar $\{0001\}$ are three main morphology-related surfaces in wurtzite ZnO. It is well known that zinc oxide tends to grow along the <001> to minimize the polar $\{0001\}$ surface areas and form highly oriented nanowires or nanorods. These one-dimensional ZnO nanostructures are suitable for use in piezoelectric generators,[171] UV photodectors,[172] and solar cells (*i.e.* dye sensitized).[173] In other cases, including gas sensors[174] and photocatalysis,[175] the two-dimensional hexagonal nanoplates with polar $\{0001\}$ surfaces exposed often present higher activity. So the *a*-axis oriented crystal growth is encouraged and this can be fulfilled by introducing organic molecules (*i.e.* citrates) during ZnO crystal growth, which would selectively adsorb on the $\{0001\}$ facets and inhibit the crystal growth along [0001]

directions.[176,177] The surface chemistry of semipolar $\{10\bar{1}1\}$ facets can also be tailored under the presence of ionic liquid, such as a mixture of carboxylic acid and amine, resulting in pyramid shaped ZnO crystals.[153]

In this chapter, I have demonstrated that ZnO thin films with well-shaped hexagonal pyramid and hexagonal plate morphologies can be synthesised on glass substrates by AACVD of zinc-acetate-dihydrate, acetic acid and D.I. water in methanol. These textured ZnO coatings exhibit good visible transparency (~70 %), low sheet resistance (~60 Ω sq^{-1}) and ultra large haze factor (up to 98.5 %), which can be potentially used as the front contact in thin-film solar cells.

6.2 Experimental

All reagents, zinc-acetate-dihydrate (≫ 98 %), acetic acid (≫ 99 %) and methanol (anhydrous, 99.8 %), were purchased from Sigma-Aldrich and used as received without further purification. Deionized water was taken from Vivendi water purification system.

Pyramid-shaped ZnO films prepared by adding various acetic acid contents in precursor solutions

Aqueous solutions for the AACVD of pyramid-shaped zinc oxide films were prepared by dissolving 1.2 g zinc-acetate-dihydrate and 0-8 mL acetic acid in 120 mL methanol. Deposition was carried out on FTO glass (150 mm × 45 mm × 3 mm, NSG-Pilkington TEC 15) at an optimized temperature of 400 ℃ and nitrogen gas flow rate of 1.5 L min^{-1}. The deposition time took around 120 minutes. The detailed experimental conditions and corresponding sample I.D. are listed in Table 6.1.

Table 6.1 Experimental parameters for the AACVD of pyramid-shaped ZnO films.

Sample I.D.	Zinc-acetate-dihydrate	Methanol	Acetic acid	Deposition temperature	Deposition time	Flow rate
	[g]	[mL]	[mL]	[℃]	[min]	[L min^{-1}]
C1	1.2	120	0	400	120	1.5
C2	1.2	120	2	400	120	1.5
C3	1.2	120	4	400	120	1.5
C4	1.2	120	8	400	120	1.5

Plate-shaped ZnO films prepared by adding various acetic acid and D.I. water contents in precursor solutions

Aqueous solutions for the AACVD of plate-shaped zinc oxide films were prepared by dissolving 0.6 g zinc-acetate-dihydrate, 0-1 mL acetic acid and 0-4 mL DI water in 60 mL methanol. Deposition was carried out on silica coated float glass (150 mm × 45 mm × 4 mm, Pilkington NSG) at an optimized temperature of 450 ℃ and nitrogen gas flow rate of 1.0 L min^{-1}. It is worth mentioning that the addition of D.I. water makes the precursor solution harder to aerosolize and hence prolongs the deposition time from around 60 mins to 100 mins. Further addition of D.I. water, *i.e.* 6 mL, into precursor solutions would deteriorate the aerosol mist quality and cannot yield deposit on the substrates. The detailed experimental conditions and corresponding sample I.D. are listed in Table 6.2.

Table 6.2 Experimental parameters for the AACVD of plate-shaped ZnO films.

Sample I.D.	Zinc-acetate-dihydrate	Methanol	Acetic acid	D.I. water	Deposition temperature	Deposition time	Flow rate
	[g]	[mL]	[mL]	[mL]	[℃]	[min]	[L min^{-1}]
ZnO-o	0.6	60	0	0	450	60	1.0
ZnO-a	0.6	60	1	0	450	60	1.0
ZnO-aw	0.6	60	1	4	450	100	1.0

6.3 Results and discussion for the AACVD of pyramid-shaped ZnO films

Fig. 6.1(a) presents the optical images of the AACVD ZnO films on FTO glass surface prepared with various acetic acid contents in precursor solutions. It can be seen that in the cases without or with 2 mL acid, the deposits are highly transparent and then become slightly opaque after 4 mL acetic acid was added. This haze effect is further strengthened when the acid volume is increased to 8 ml. It is worth mentioning that the opaque area only exist at the second half region on glass surfaces. According to my observations, the addition of acetic acid hardly changes the aerosol mist quality and the deposition time, although the density of acetic acid (1.05 g cm^{-3}) is higher than that of methanol (0.79 g cm^{-3}).[178] Thus, the reason for the selectively growth of hazy ZnO films on the second half glass area may not relate to the change of aerosol density and further investigation is needed to explain it.

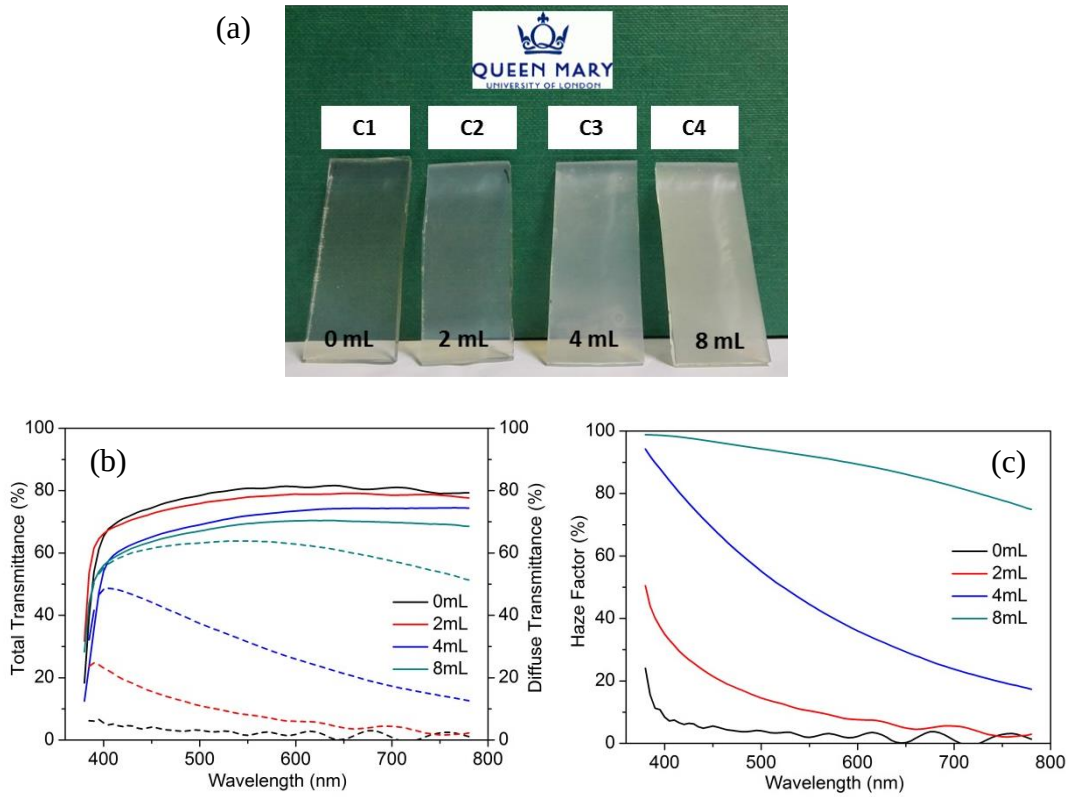

Figure 6.1 (a) Optical appearance of AACVD ZnO films on FTO glass substrates prepared with 0-8 mL acetic acid in precursor solutions. These glass slides (20 mm × 45 mm) were cut from the first half (C1 and C2) and the second half (C3 and C4) area on four individual substrates (150 mm × 45 mm), respectively. (b) UV-Vis total and diffuse transmittance and (c) haze factor spectra for the studied ZnO coatings.

To better characterize the observed optical behaviour, the total and diffuse transmittance as well as haze factor of these ZnO coatings were measured and are illustrated in Fig 6.1 (b) and (c). As observed, all samples exhibit high total transmission across the visible light range (380-780 nm), with an average value of ~70-80 % including the FTO substrate absorbance (shown in Table 6.3). By contrast, the diffuse transmission varies tremendously from less than 5 % in C1 to as high as 63 % in C4; so the latter obtains an ultra-large haze factor ($T_{diffuse}/T_{total}$) of 91.6 % and strong light trapping ability. On the other hand, the enhancing light scattering would also increase the visible light loss, so the film total transmittance reduces gradually from an average value of 80.3 % in C1 to 69.1 % in C4.

Table 6.3 Structural and optical parameters for AACVD ZnO films prepared with various acetic acid contents in precursor solutions.

Sample I.D.	Film thickness	Texture coefficient			$R_{(RMS)}$	T_{total}	$T_{diffuse}$	Haze
	[μm]	(100)	(002)	(101)	[nm]	[%]	[%]	[%]
C1	0.82	3.07	0.13	0.93	12.8	80.3	2.3	2.9
C2	0.90	1.79	0.37	0.95	16.1	77.7	8.1	10.4
C3	0.57	1.44	0.31	1.24	45.1	71.8	30.9	43.0
C4	0.59	0.48	1.82	0.67	103.0	69.1	63.3	91.6

To explain this acid-dependent film optical performance, the morphology of these zinc oxide coatings were examined by SEM and AFM. As seen in Fig. 6.2 and Fig. 6.3, the untreated ZnO is composed by refined spherical grains, with an average grain size less than 50 nm and surface roughness of 12.8 nm. The microstructure then turns into agglomerated particles (~350 nm) after a minor addition of 2 mL acetic acid to the precursor solution. ZnO grains with pyramidal shapes start appearing in C3, in which the angle between two opposite edges was calculated at 63°, only one degree lower than the reported value in $\{10\bar{1}1\}$ faceted pyramids.[96] This pyramidal morphology helps increase the surface roughness to 45.1 nm and so more light is scattered. Moreover, the grains in C3 seem less densely-packed than that in previous two samples, representing a potential decrease of nucleation rate. The ZnO pyramids were further coarsened after the acid content is increased to 8 mL and well-shaped grains with six identical facets are clearly observed. The resulting film surface is relatively-rough, with its R_{RMS} as high as 103 nm, and so strong light scattering effect is observed. Based on these microstructure observations, we could conclude that i) the introduction of acetic acid alters the ZnO grain size and morphology tremendously, and ii) the observed opaque film appearance and light scattering properties is largely related to their pyramidal surface structures.

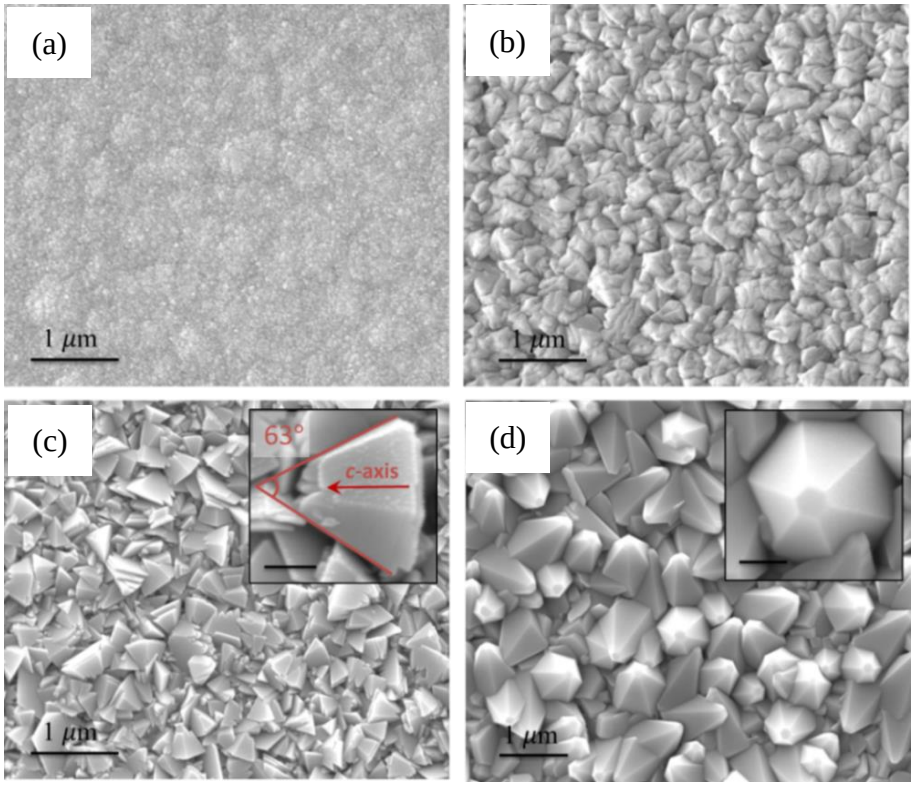

Figure 6.2 SEM images of AACVD ZnO films with (a) 0 mL, (b) 2mL, (c) 4 mL and (d) 8 mL acetic acid added in precursor solutions. The insets show higher magnification images for corresponding sample and the scale bar inside corresponds to 250 nm.

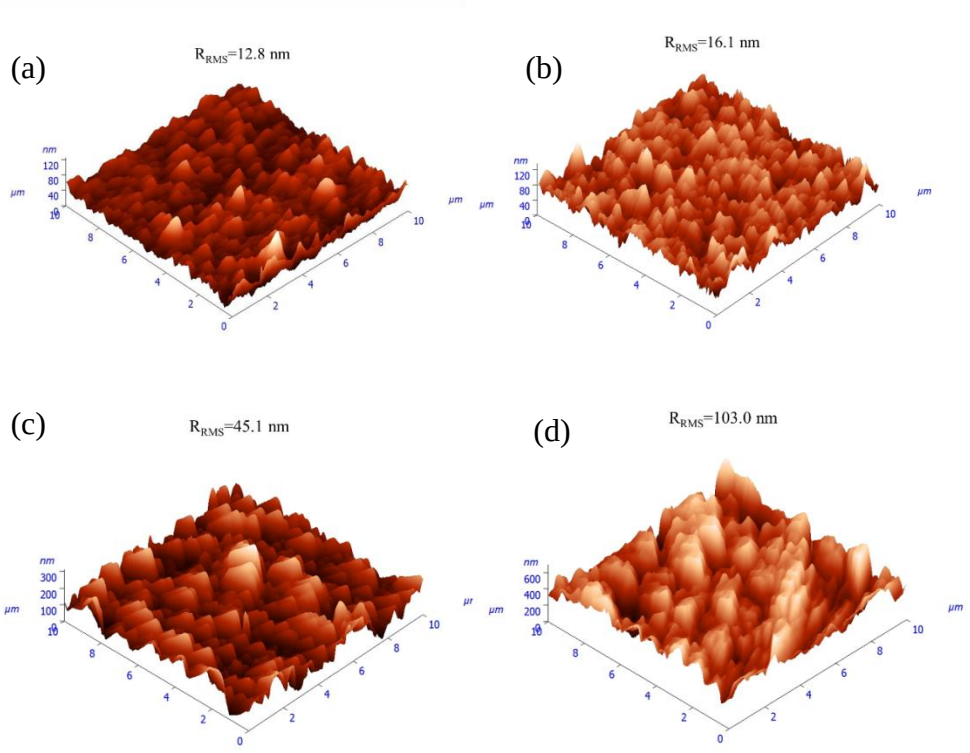

Figure 6.3 AFM images of AACVD ZnO films with (a) 0 mL, (b) 2mL, (c) 4 mL and (d) 8 mL acetic acid added in precursor solutions.

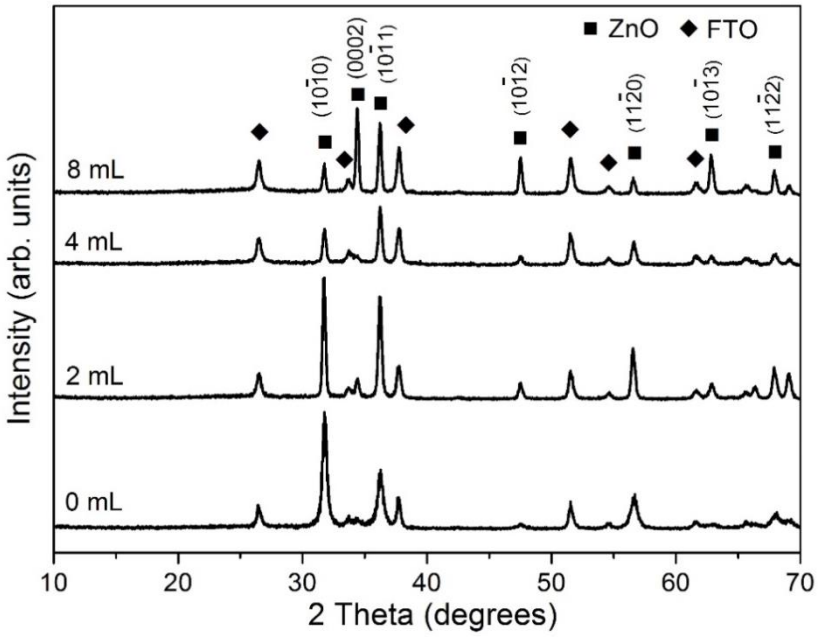

Figure 6.4 XRD patterns of AACVD ZnO films prepared with various acetic acid contents in precursor solutions.

The above morphology change is also reflected by the changes in the XRD patterns for the samples. As shown in Fig. 6.4, besides the diffraction peaks from the substrate SnO_2 layer, all other reflection signals can be matched to ZnO with hexagonal wurzite structure (JCPDS 36-1451).[124] Moreover, the untreated sample C1 exhibits an intense peak along the $(10\bar{1}0)$ crystallographic plane with a high texture coefficient $TC_{(100)}$ of 3.07. This preferential orientation becomes much less significant in C2, whereby the $TC_{(100)}$ reduces to a value of 1.79. The intensity of $(10\bar{1}1)$ peak exceeds that of $(10\bar{1}0)$ in C3 and C4, which is consistent with the XRD results of pyramid-shaped ZnO in previous studies and represents more crystal choose to grow along $[10\bar{1}1]$.[153,179] It is noteworthy that, different with the *a*-axis oriented $(10\bar{1}0)$ and *c*-axis oriented (0001) plane, whose higher XRD peak intensity often means less corresponding surfaces getting exposed, the promotion of $(10\bar{1}1)$ -oriented crystal growth will result in larger surface areas and higher

diffraction signals together due to its unique symmetry. Thus, combined with the SEM details in Fig. 6.2, we could conclude that the side facets in the ZnO pyramids are $\{10\bar{1}1\}$ planes. The other interesting information from the XRD pattern is the (0002) diffraction peak in C3 ($TC_{(002)}$ = 0.31) is hardly observed and then become significant in C4 ($TC_{(002)}$ = 1.82), although both surfaces are pyramidal shaped. This transition may originate from a change of crystal packing direction. For example, as shown in Fig. 6.2(c), the *c*-axis orientations of ZnO pyramids in C3 are parallel to the substrate, so their (0002)-oriented crystalline atoms cannot be diffracted by the incident X-ray beams. By contrast, the *c*-axis in the latter specimen C4 is perpendicular or near perpendicular to its surface and thus the (0002) reflection signals are readily collected.

In general, the crystallization procedure of thin films can be divided into the nucleation and grain growth processes. For the current AACVD reaction of ZnO nanomaterials, a plausible crystal nucleation mechanism is proposed as follows:[180–182]

$$Zn(CH_3COO)_2 \rightleftharpoons Zn^{2+} + 2\,CH_3COO^- \quad (6\text{-}1)$$

$$CH_3OH \rightleftharpoons CH_3^+ + OH^- \quad (6\text{-}2)$$

$$Zn^{2+} + 2OH^- \rightleftharpoons Zn(OH)_2 \quad (6\text{-}3)$$

$$Zn(OH)_2 \rightarrow ZnO + H_2O \uparrow \quad (6\text{-}4)$$

$$CH_3COOH \rightleftharpoons H^+ + CH_3COO^- \quad (6\text{-}5)$$

Initially, under the equilibrium solution state, the Zn^{2+} cations from zinc acetate (eqn (6-1)) would readily react with the OH^- anions from methanol (eqn (6-2)) to form $Zn(OH)_2$ (eqn (6-3)). After the aerosol droplets were transported to the heated

substrate, the $Zn(OH)_2$ would simultaneously decompose into crystalline ZnO and generating nuclei, whereby the by-products will be removed out of the reactor with the flushing nitrogen gas (eqn (6-4)). So the number and size of the ZnO nucleus formed are controlled by the concentration of Zn^{2+} and OH^- in the precursor mixture and the substrate heating temperature, respectively. Take the untreated sample C1 as an example, its small grain size indicates the nucleation rate is extremely high during this deposition. The introduction of acetic acid in precursor solutions would i) bring in excess CH_3COO^- anions (eqn (6-5)) and reduce the Zn^{2+} concentration by promoting eqn (6-1) to proceed to the left side, and ii) introduce the OH^- scavenger, H^+, which both lowers the ZnO nucleation rate and decreases the number of nuclei sites. Thus, the crystals in acid-treated ZnO samples could obtain more lateral space to grow up and their grains are getting increasingly bigger.[180] But on the other hand, since less nucleus could form on the substrate especially under a high acid input, the film thickening process in C3 and C4 will be considerably retarded. So these two samples become thinner compared to C1 and C2, as illustrated by their cross-section images in Fig. 6.5.

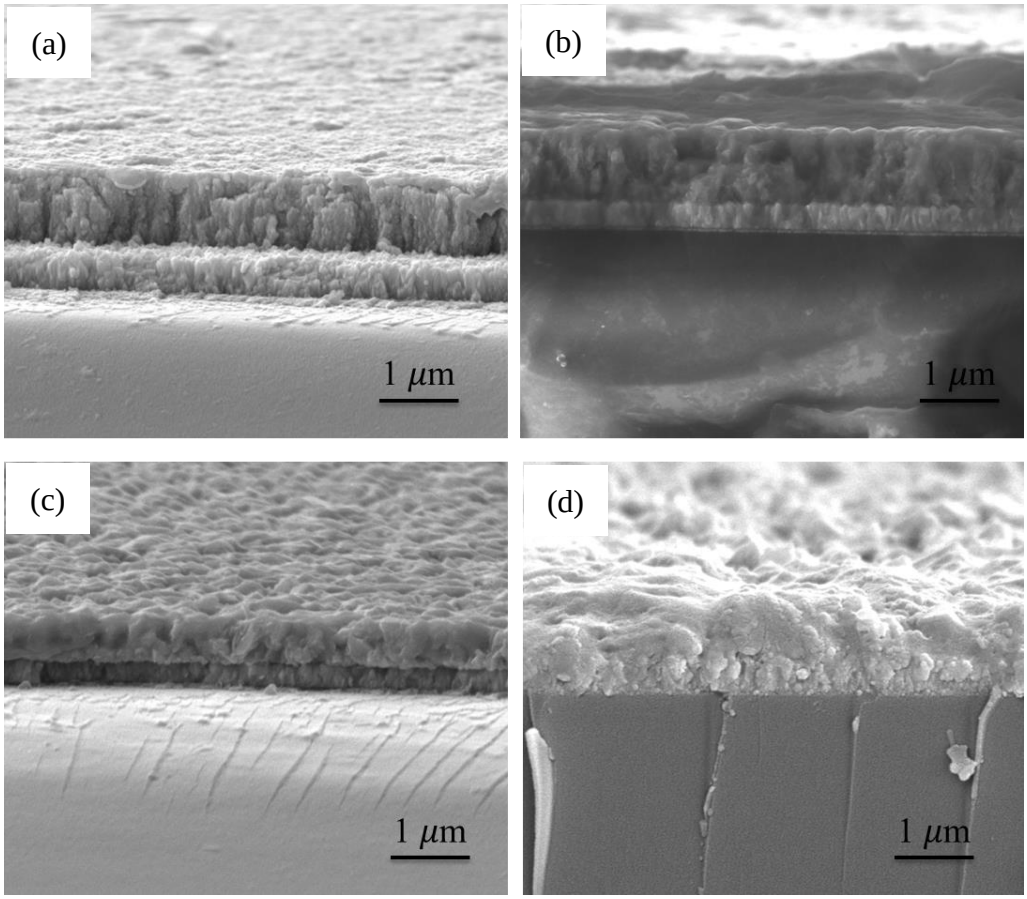

Figure 6.5 Cross-section SEM images of AACVD ZnO films with (a) 0 mL, (b) 2mL, (c) 4 mL and (d) 8 mL acetic acid added in precursor solutions.

After the initial nucleation, the following grain growth process determines the final film morphology. Typically, the fast-growing surfaces, such as untreated polar facets, exhibit small facets or even disappear during crystal growth because they will be replaced by slower-growing equivalent planes which are observed in the final crystal as the exposed surfaces.[153,183] Moreover, the organic molecules could be incorporated into the crystal lattice at the polar facets and hence slow their growth rate. It is widely known that the carboxylates are often selectively adsorbed on the ZnO surface sites,[184] such as citrate bound onto the Zn^{+}-terminated (0001) surface,[176,177,185] and different carboxylic acids have been utilized to modify ZnO crystal morphology from nanorods to nanoplates.[186] Thus, in this case, the presence of surplus acetate anions effectively reduces the surface energy of the

growing $\{10\bar{1}1\}$ plane and promotes the formation of ZnO pyramids. Nevertheless, it is still unclear why the acetic acid selectively functions as the growth modifier of $\{10\bar{1}1\}$ surfaces instead of other crystallographic facets. Density-function theory simulation study may provide a better understanding to this.

Finally, it is noteworthy that the electrical properties, *i.e.* resistance or resistivity, for these ZnO samples are unmeasurable because they were deposited on the highly conductive FTO glass substrates, whereby the FTO layer is being measured rather than the ZnO layer during the tests. In the next Section 6.4, textured zinc oxide coatings were made on silica glasses and the film resistance was evaluated by using four-point probe method.

6.4 Results and discussion for the AACVD of plate-shaped ZnO films

Fig. 6.6 presents the optical images of the AACVD ZnO films on silica glass surfaces prepared with various acetic acid and D.I. water contents in precursor solutions. As observed, untreated ZnO displays an uniform transparent area in the middle of substrate and this region becomes slightly opaque after adding acetic acid in precursor solution. Further addition of D.I. water produces ultra-hazy coating mainly at the first part of glass surface, indicating a change of film growth mechanism. We infer the introduction of high volume deionised water would increase the aerosol density considerably since the density of water (1.0 g cm^{-3}) is higher than that of methanol (0.79 g cm^{-3}),[178] whereby the precursor droplets were likely to be absorbed on the substrate immediately after entering into the reactor at the given flow rate. By comparison, the lighter precursor mist in another two depositions may obtain sufficient momentum to migrate to the thermodynamically preferred central glass region and yield denser coatings.

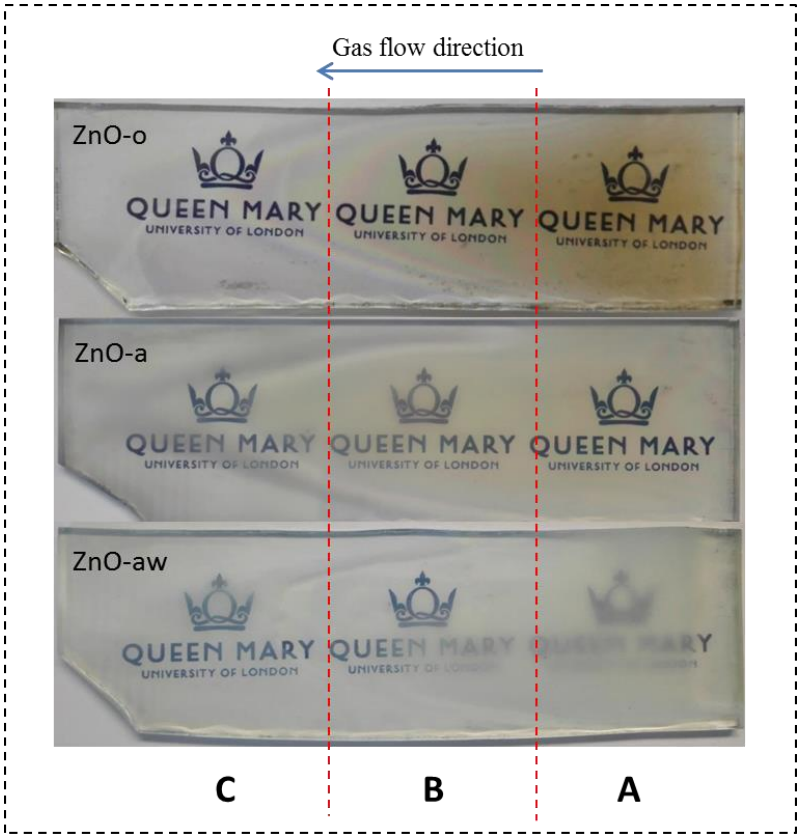

Figure 6.6 Optical appearance of AACVD ZnO films on silica glass substrates prepared with various acetic acid and D.I. water contents in precursor solutions. The central area B in ZnO-o and ZnO-a as well as the section A in ZnO-aw were selected for materials characterization.

To better characterize the initial optical observations, the UV-Vis total and diffuse transmittance of the ZnO films were measured and are illustrated in Fig. 6.7(a). The corresponding values are listed in Table 6.4. It is seen that all three samples exhibit similar high total transmission (68.1-72.4 %) across visible region. By contrast, their diffuse transmission displays significant variations from an average value of 3.2 % in ZnO-o to 44.0 % in ZnO-a and 67.1% in ZnO-aw. In this regard, distinct haze spectra are presented in Fig. 6.7(b) and the haze factor for ZnO-aw was found to be as high as 98.5 %, which is, to my best knowledge, the most hazy zinc oxide film so far reported.[38]

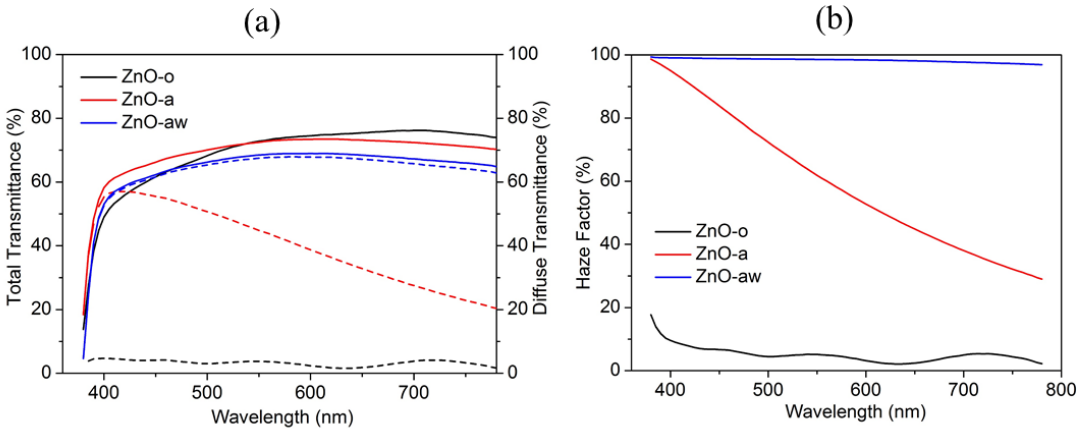

Figure 6.7 (a) UV-Vis total and diffuse transmittance and (b) haze factor spectra of AACVD ZnO films prepared with various acetic acid and D.I. water contents in precursor solutions.

Table 6.4 Structural and optical parameters for AACVD ZnO films prepared with various acetic acid and D.I. water contents in precursor solutions.

Sample I.D.	Film thickness	Texture coefficient			$R_{(RMS)}$	T_{total}	$T_{diffuse}$	Haze
	µm	(100)	(002)	(101)	nm	%	%	%
ZnO-o	1.0	2.57	0.76	0.79	11.9	72.4	3.2	4.4
ZnO-a	0.85	0.36	1.67	0.98	125.6	72.2	44.0	60.9
ZnO-aw	0.88	0.09	3.77	0.21	216.6	68.1	67.1	98.5

The structural properties of the studied ZnO coatings (including surface and cross-section morphology as well as crystal orientations) were examined by SEM, AFM and XRD. As seen in Fig. 6.8(a), untreated ZnO is largely composed by spherical agglomerated particles (~200 nm in diameter) and these agglomerates are formed of refined rods around 100 nm in length, which are only visible under the high magnification. These wedge-like grains are quite different with previously reported disc-like ZnO crystals under similar AACVD conditions.[141] The corresponding XRD pattern in Fig. 6.8(g) exhibits a preferred growth direction along the $(10\bar{1}0)$ crystallographic plane with a high texture coefficient $TC_{(100)}$ of 2.57, which may relate to its rod-like crystal growth.[156] The introduction of acetic acid results in uniform large tilted hexagonal plates (~1 µm in diameter) on ZnO-a film surface (see Fig. 6.8(b)). These hexagonal-plates are highly likely to be the base planes for ZnO

pyramids because the side facets of hexagonal pyramid are clearly observed in the inset higher magnification image and the corresponding cross-section image in Fig. 6.8(e). The evidence of pyramidal ZnO can be further verified from its diffraction pattern in Fig. 6.8(h), whose $(10\bar{1}1)$ peak intensity exceeds that of $(10\bar{1}0)$ and (0002), in accordance with a previous report of ZnO pyramids.[153] It is worth mentioning that the morphologies of ZnO-o and ZnO-a are distinct from that of sample C1 and C2, respectively, although the precursor concentrations between two corresponding depositions are identical. We infer this large variations in film surface morphology is mainly related to the increase of deposition temperature from 400 ℃ in C1 and C2 to 450 ℃ in ZnO-o and ZnO-a, where a higher reaction temperature has been demonstrated to promote AACVD ZnO crystal growth tremendously.[141] The influence of substrate on the zinc oxide nucleation and grain growth may be limited since the crystal structure of ZnO (hexagonal wurtzite) is different with that of SnO_2 (tetragonal rutile) [187] and thus an epitaxial growth phenomenon is unlikely to happen under current deposition conditions. The presence of deionized water in precursor solutions hardly increases the ZnO crystal size (~1.1 μm in diameter) but helps fully expose the hexagonal plates. As shown in Fig. 6.8(c), the microscale plates are uniformly well-stacked along the normal direction, however the side-view for ZnO-aw (see Fig. 6.8(f)) illustrates the sample is thickened by large continuous grains. This indicates those overlapped plates only exist on the film surface instead of through the whole bulk area, which may explain why the XRD pattern of ZnO-aw in Fig. 6.8(i) exhibits an extremely strong peak along the [0001] direction ($TC_{(002)}$ = 3.77) instead of the $[10\bar{1}0]$ direction ($TC_{(100)}$ = 0.09).

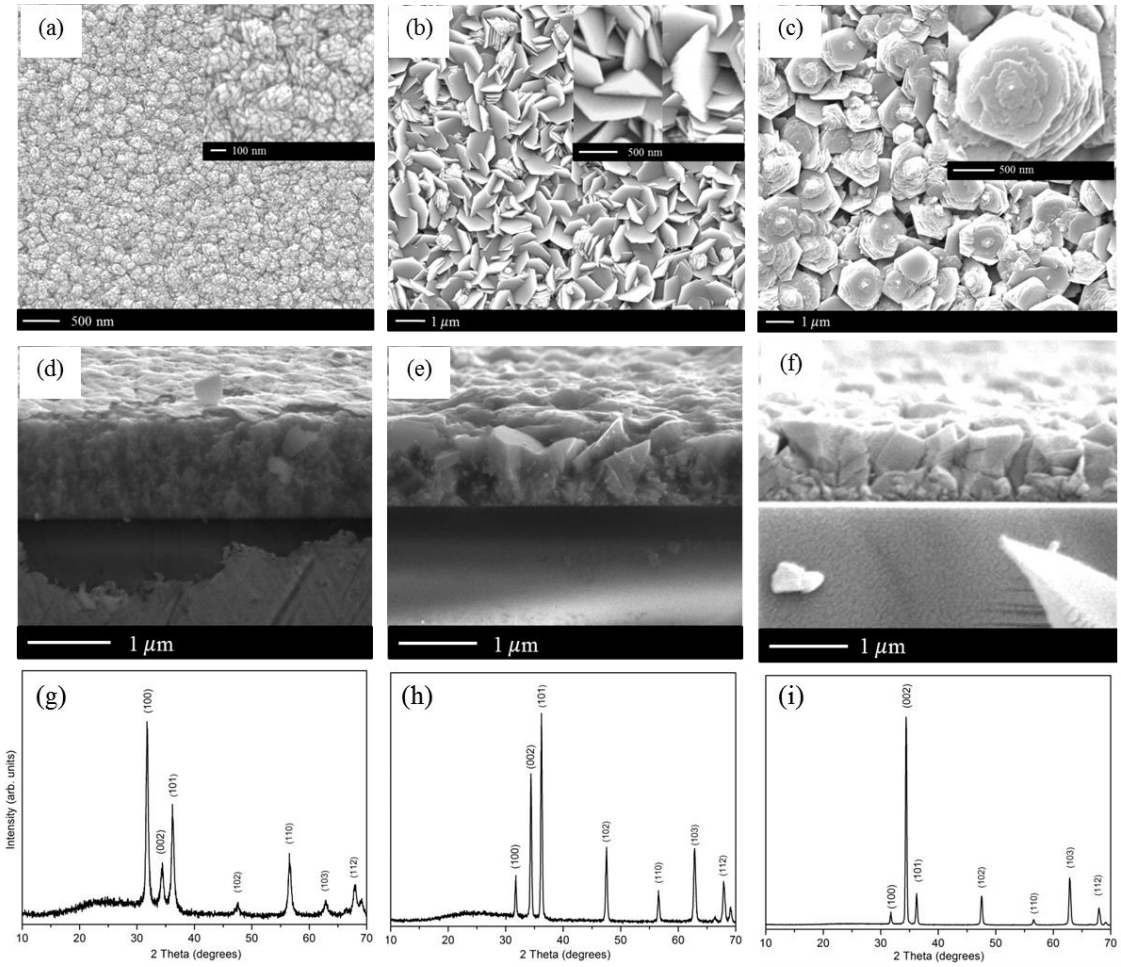

Figure 6.8 SEM and XRD images of (a), (d), (g) ZnO-o, (b), (e), (h) ZnO-a and (c), (f), (i) ZnO-aw films.

From the AFM images in Fig. 6.9(a)-(c), the root mean square roughness (R_{RMS}) of ZnO-o, ZnO-a and ZnO-aw films are found to be 11.9 nm, 125.6 nm and 216.6 nm, respectively. Therefore, we can infer that the strong light trapping effect in ZnO-aw results from its rough surface. It is noteworthy that, although ZnO-a has a similar roughness value to previous pyramidal ZnO sample C4 ($R_{RMS} \approx 103$ nm), the latter however exhibits a superior haze performance (91.5 %) over ZnO-a (60.9 %). This indicates that surface roughness is not the only dominant parameter in determining film haze. The topography of light scatter also plays an essential role and in some cases maybe more dominant in determining film haze.

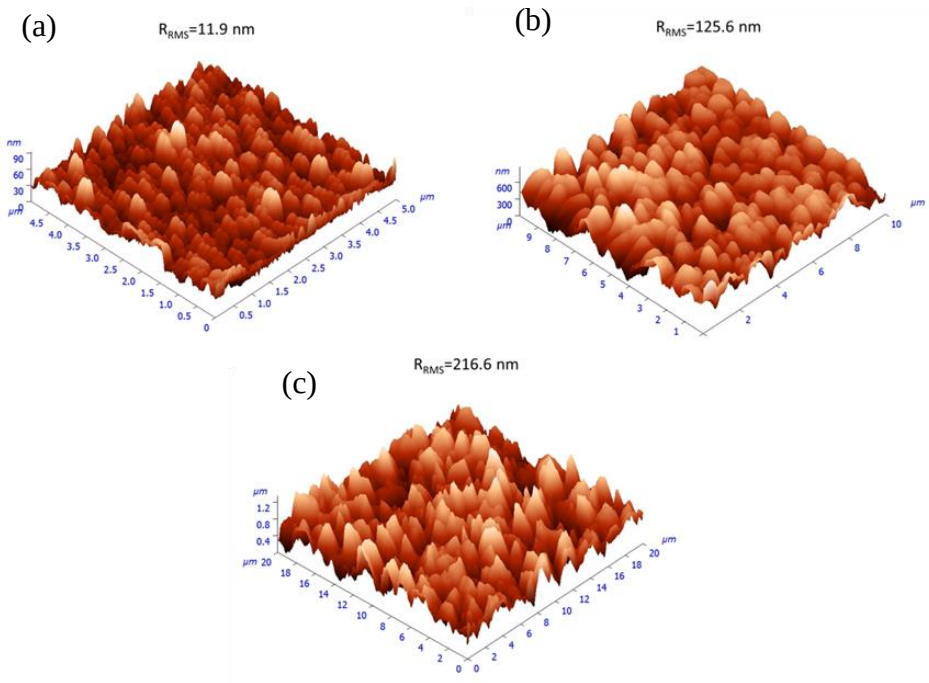

Figure 6.9 AFM images of (a) ZnO-o, (b) ZnO-a and (c) ZnO-aw films.

As discussed in Section 5.3, the formation of hexagonal pyramids in acid treated ZnO is originated from a retarded crystal nucleation and reduced polar surface energy with the assistance of capping acetate ions. But under the current conditions the interactions between acetates and {0001} facets may be more significant than that of $\{10\bar{1}1\}$, so the hexagonal base plates are more favourable to be exposed on the film surfaces instead of the pyramid side planes. Moreover, the addition of D.I. water increases the aerosol density and narrows the film growth region at the beginning of glass surface. In this regard, a majority of acetate ions added may have reached the glass surface, since less acetic acid would be pre-decomposed because of the much shorter traveling distance within the reactor. This increase of acetate concentration would favour the *a*-axis oriented crystal growth, as suggested in the case of citrates, [176,188]and well-defined hexagonal plates are readily obtained. But during the film thickening process, these multistacked plates would simultaneously emerge into continuous *c*-axis oriented grains because the large interfacial area

between polar {0001} facets is energetically unstable. As a result, the reflection signals of {0001} planes overwhelm that of $\{10\bar{1}0\}$ and $\{10\bar{1}1\}$ in the XRD pattern.

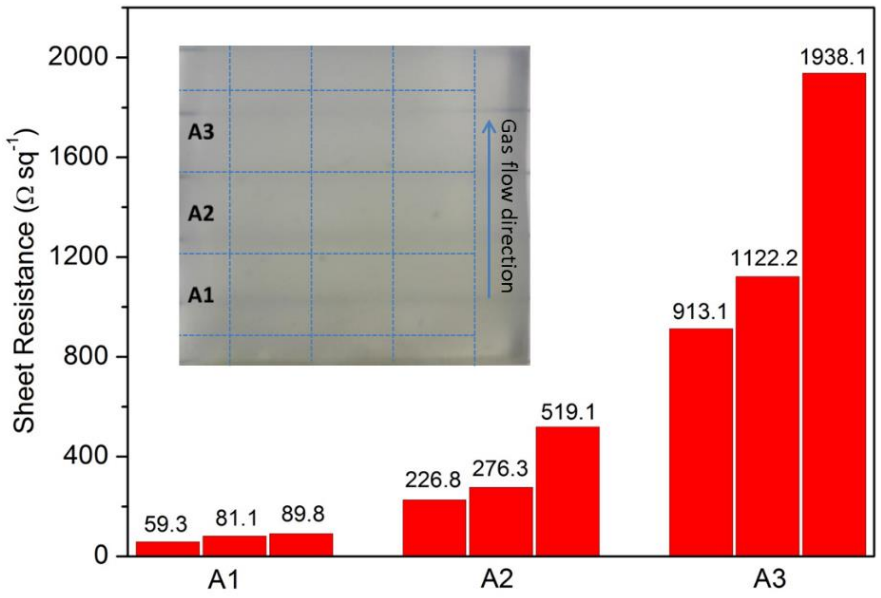

Figure 6.10 Film conductivity as a function of gas flow distance for a typical ZnO-aw sample.

Finally, film electrical conductivity was evaluated by using the four-point probe method. Untreated ZnO is electrically resistant with resistance values exceeding MΩ sq^{-1}. The addition of acetic acid effectively reduces it to ~2.3-4.1 KΩ sq^{-1}. The presence of D.I. water helps lower the film resistance further to a minimum value of ~60 Ω sq^{-1}. This number is still a little high compared to those in previously reported ZnO:B front electrodes (~10-30 Ω sq^{-1}),[9,188] but considering that those ZnO:B samples (~2-4 μm) are much thicker than ours (~1 μm), a more conductive ZnO-aw specimen can be anticipated once we prolong the deposition time. The conductivity of as-grown ZnO films can also be easily improved by additional hydrogen and/or argon plasma treatments.[189–191] It is worth mentioning that the ZnO-aw film resistance would increase linearly along the gas flowing direction, as illustrated in Fig. 6.10. This further supports my idea that the presence of deionized water could

enhance the aerosol density considerably and thus the deposition area closer to the gas inlet receives more nucleuses. But for real industrial production, uniform deposits can be guaranteed by employing a more advanced aerosol delivery system.[192]

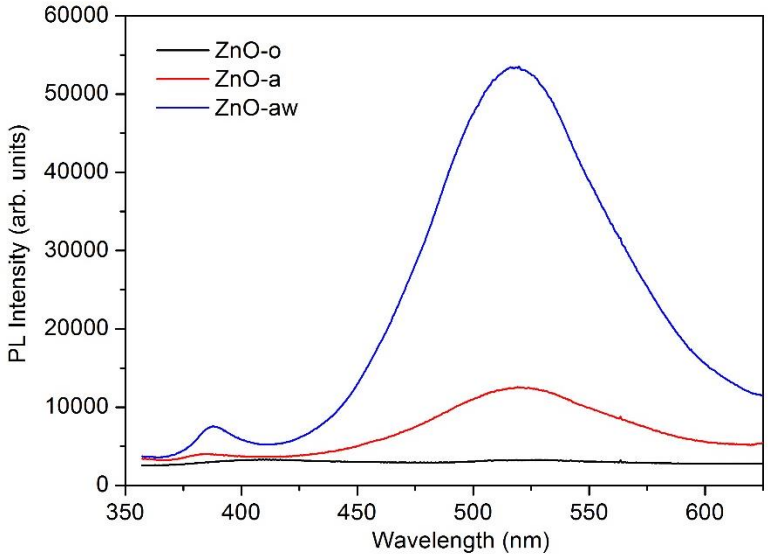

Figure 6.11 Room-temperature PL spectra of AACVD ZnO-o, ZnO-a and ZnO-aw films.

To explain the large variations in film conductivity, we examined the PL spectra of studied ZnO samples. As seen in Fig. 6.11, the ZnO-aw displays a board and intense peak near 520 nm, which has been reported to arise from a radiative recombination involving some lattice structural defects, such as oxygen vacancies, zinc vacancies, zinc interstitials.[193–195] This green emission peak becomes much less profound in ZnO-a and for the untreated ZnO sample the signals basically disappear into the background levels. According to previous studies, the zinc oxide samples with a large fraction of polar planes contain more oxygen vacancies.[170,196] A qualitative explanation to this phenomenon is that the ZnO polar planes stabilized by OH groups are subject to forming oxygen vacancies by removing either OH or H_2O groups from the surface.[196,197] Moreover it is well

known that the continuous columnar grain structure in ZnO would favour the charge carrier movement to a large extent. By comparison, the refined particles bring in a large amount of trapping centres for the carriers and deteriorate their mobility. Thus, combined the structural, electrical and photoluminescence results together, I could conclude that the low resistance in ZnO-aw should result from its high oxygen vacancy concentration and good carrier mobility together.

6.5 Conclusions

In this chapter, highly surface-textured zinc oxides films were successfully deposited on FTO and silica glass substrates by AACVD of zinc-acetate-dihydrate, acetic acid and deionized water in methanol. The addition of acetic acid in precursor solutions could i) promoted lateral grain growth by inhibiting the crystal nucleation, and ii) exposed $\{10\bar{1}1\}$ and $\{0001\}$ polar facets by lowering their surface energy, which helped form pyramid-like and plate-shaped film surface. These textured ZnO films exhibited good visible transparency (~70 %), low sheet resistance (~60 Ω sq^{-1}) and ultra large haze factor (up to 98.5 %), which could be potentially used as the front contact in thin-film solar cells.

Chapter 7 AACVD of Methylammonium Lead Iodide Films

The following chapter describes the deposition of methylammonium lead iodide films on FTO glass substrates using a novel two-step and three-step sequential AACVD process. The resulting $CH_3NH_3PbI_3$ coatings exhibit high uniformity, good phase purity and compact micron-sized pinhole-free grains, which can be potentially used as the light absorber layer in perovksite solar cells.

7.1 Introduction

The involvement of the AACVD community in perovskite solar cell area started in early 2014, where D.J. Lewis *et al.* firstly reported that phase pure perovskite $CH_3NH_3PbBr_3$ materials can be deposited onto glass substrates by single-step AACVD process at a temperature of 250 ℃.[198] After that $CH_3NH_3PbI_3$ films were synthesised on float glass by D.S. Bhachu *et al.* under similar AACVD conditions at 200 ℃.[199] However, the nano-to-microscale morphology of these AACVD perovskites was not studied in detail, with films appearing to have a low density and poor coverage on the substrates, as shown in Fig. 7.1. We infer these less densely packed perovskite coatings originate from the relatively high deposition temperature employed in the single-step process, which is required to fulfil the reaction between PbI_2 and CH_3NH_3I (or $PbBr_2$ and CH_3NH_3Br) but also often results in unfavourable gas phase nucleation and powdery deposits.[33] Therefore the one-step AACVD perovskite film morphology needs further modification for efficient photovoltaic performance. It is now widely accepted that the perovskite film properties including thickness, uniformity and morphology are hard to manipulate in an one-step solution-based processes, since it can be significantly affected by the environment.[200,201] By contrast, the multi-step methodologies allows for independent control in the

deposition conditions of each precursor and reaction, which eventually enables a better control over the perovskite film formation.[103]

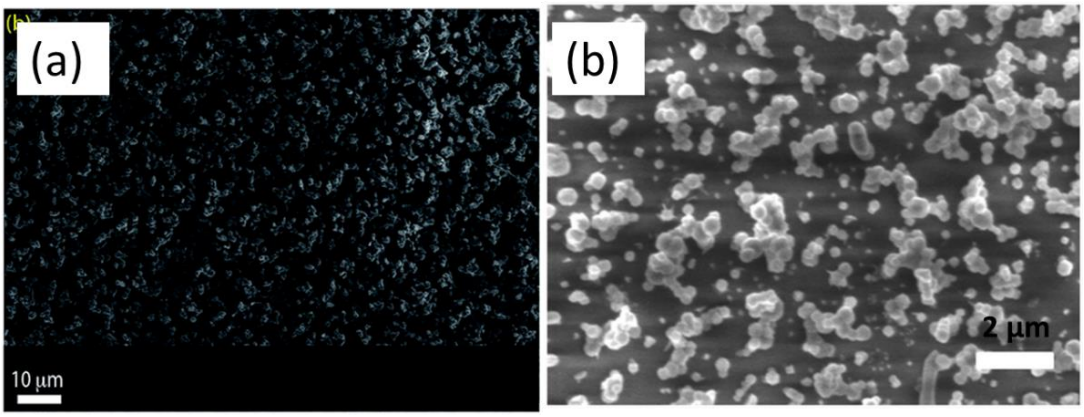

Figure 7.1 Poor-connected (a) $CH_3NH_3PbI_3$ and (b) $CH_3NH_3PbBr_3$ films on glass substrates fabricated by single-step aerosol assisted chemical vapour deposition.[198,199]

Based on the above observations, here I have investigated a sequential two-step AACVD method to fabricate high quality organo-metal halide perovskite materials on FTO glass substrates. The resulting $CH_3NH_3PbI_3$ films exhibit large area uniformity, good phase purity and micron-sized pinhole-free grains. After that, a sequential three-step AACVD process was developed to further improve the $MAPbI_3$ perovskite film morphology and thickness. We believe these AACVD perovskite materials have great potential to be used as the light absorber layer in perovksite solar cells.

7.2 Experimental

PbI_2 (99 %), *N*,*N*-Dimethylformamide (DMF, ≫ 99 %) and methanol (anhydrous, 99.8 %) purchased from Sigma-Aldrich and used as received. CH_3NH_3I was purchased from Solaronix.

Sequential two-step AACVD of $MAPbI_3$ films

The schematic of a typical two-step AACVD of $MAPbI_3$ films is illustrated in Fig 7.2, where a moderate deposition temperature (70 ℃) was firstly employed to obtain flat PbI_2 coatings on glass surfaces, followed by a higher heat input (220 ℃) to fulfil the reaction with CH_3NH_3I. For comparison, a temperature of 100 ℃ and 150 ℃ were employed for the PbI_2 and the CH_3NH_3I deposition, respectively, to investigate the effects of reaction temperatures to the perovskite film morphology.

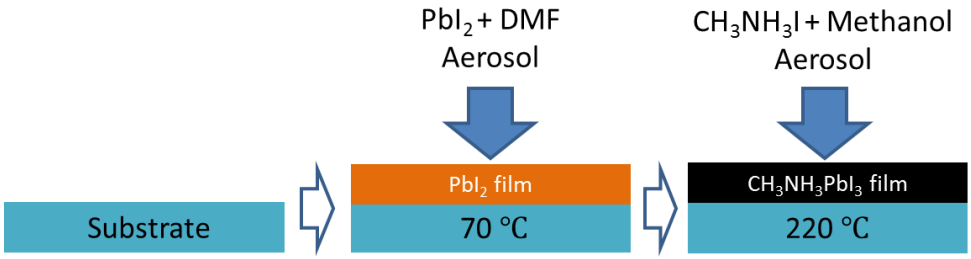

Figure 7.2 Schematic illustration of perovskite film formation through sequential two-step AACVD process.

Aqueous solutions for the PbI_2 deposition were prepared by dissolving PbI_2 in DMF, and for the subsequent $CH_3NH_3PbI_3$ formation CH_3NH_3I was dissolved in methanol. Methanol was selected as the carrier solvent for methylammonium iodide instead of the widely used isopropyl alcohol as it is extremely difficult to generate a mist from IPA. By comparison, methanol is much easier to aerosolize and CH_3NH_3I is very soluble in it. The precursor mist was created and delivered to the reaction chamber with nitrogen gas. Deposition was carried out on FTO glass (150 mm × 45 mm × 3 mm, Pilkington-NSG TEC 15). The detailed experimental conditions and corresponding sample I.D. are listed in Table 7.1.

Table 7.1 Experimental parameters for the sequential two-step AACVD $MAPbI_3$ films on FTO glass substrate.

Sample I.D.	PbI_2	DMF	CH_3NH_3I	Methanol	Deposition temperature		Flow rate	
					Step 1	Step 2	Step 1	Step 2
	[g]	[mL]	[g]	[mL]	[℃]	[℃]	[L min^{-1}]	[L min^{-1}]
D1	0.3	4	0.155	4	70	220	0.6	0.3
D2	2.0	20	0.69	20	100	150	0.8	0.8

Fig. 7.3 presents the optical image of the two-step AACVD perovskite deposit, where uniform dark coating can be clearly observed across the glass surface, indicating that $MAPbI_3$ perovskite thin film may have been successfully fabricated using the sequential AACVD process. The dense area in the middle of the glass substrate (30 mm × 30 mm) was then selected for further structural and optical characterization.

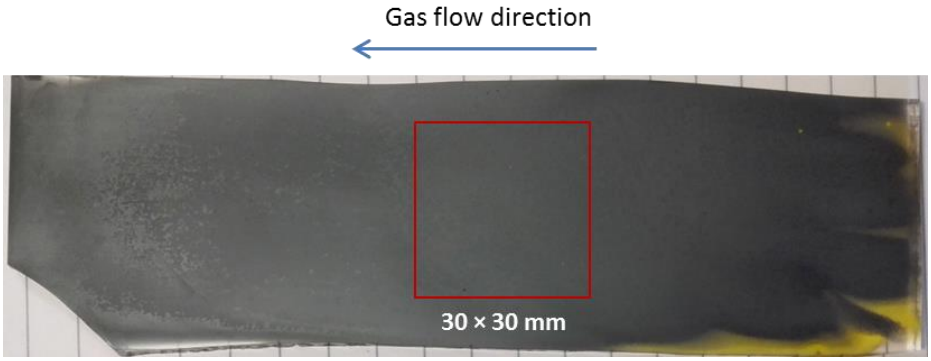

Figure 7.3 Photograph showing large-area uniform $CH_3NH_3PbI_3$ film grown by sequential two-step AACVD on FTO glass substrate.

Sequential three-step AACVD of $MAPbI_3$ films

In the three-step process, a low PbI_2 deposition temperature (30 ℃) was firstly employed to obtain a wet PbI_2-DMF deposit on the glass surface. Afterwards, the samples were dried under a moderate temperature (70 ℃) for 5 mins, which aimed to distribute the PbI_2 uniformly across the surface. Finally, a high deposition temperature (220 ℃) was utilized to fulfil the reaction between PbI_2 and CH_3NH_3I. It

is worth mentioning that the intermediate drying step is indispensable to obtain high quality perovskite film. If the samples were directly heated from 30 ℃ to 220 ℃, the PbI_2 would nucleate and grow within the solution phase in an ultra-fast way, resulting in large poorly-connected dendritic crystals. The schematic of the three-step AACVD of $MAPbI_3$ films is illustrated in Fig 7.4.

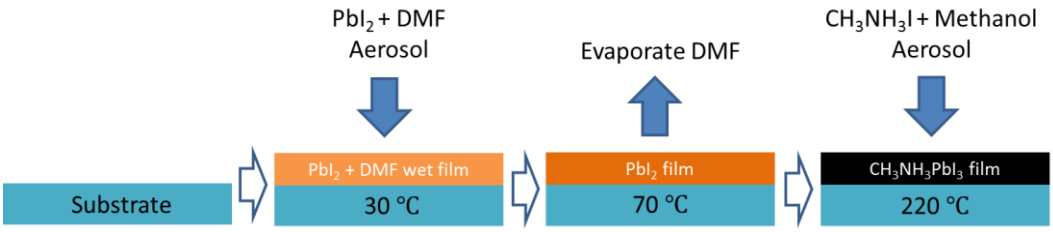

Figure 7.4 Schematic illustration of perovskite film formation through sequential three-step AACVD process.

Aqueous solutions for the PbI_2 deposition were prepared by dissolving 0.2-0.3 g PbI_2 in 4 mL DMF, and for the $MAPbI_3$ formation 0.114-0.155 g CH_3NH_3I was dissolved in 4 mL methanol (see Table 7.2). The nitrogen gas flow rate was kept at 0.5 L min^{-1} for the first two steps and at 0.3 L min^{-1} for the final deposition. FTO glass (Pilkington-NSG TEC 15) was utilized as substrate and the optimum glass size was found to be 25 mm × 10 mm. The use of wider substrate (*i.e.* 25 mm × 15 mm) would deteriorate the PbI_2 film uniformity during the solvent evaporation, arising from the large temperature gradient within the cold-wall reactor. The arrangement of these glass slides inside the CVD reactor also significantly affected the perovskite film uniformity and the optimum substrate distribution is illustrated in Fig. 7.5. The resulting three-step AACVD perovskite deposit is shown in the inset of Fig. 7.5 and these dark coatings were characterised by SEM only at the monument.

Table 7.2 Experimental and structural parameters for the sequential three-step AACVD $MAPbI_3$ films prepared under different film thickness.

Sample I.D.	PbI_2	DMF	CH_3NH_3I	Methanol	CH_3NH_3I:PbI_2 ratio	Film thickness
	[g]	[mL]	[g]	[mL]		[μm]
E1	0.3	4	0.155	4	1.5	0.94
E2	0.25	4	0.173	4	2.0	0.85
E3	0.24	4	0.124	4	1.5	0.68
E4	0.23	4	0.119	4	1.5	0.59
E5	0.22	4	0.114	4	1.5	0.65
E6	0.2	4	0.138	4	2.0	0.66

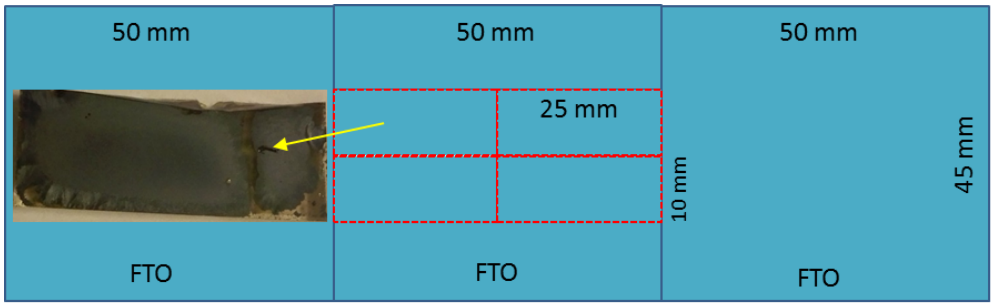

Figure 7.5 The schematic view of FTO glass arrangement within the CVD reactor for the sequential three-step AACVD process. The inset shows the optical image of the corresponding $MAPbI_3$ film.

7.3 Results and discussion for the two-step AACVD $MAPbI_3$ films

XRD measurement was firstly conducted to confirm the AACVD perovskite film crystal structure and the diffraction patterns are shown in Fig. 7.6. Besides a tiny signature peak at 12.60º in D1 and at 12.69º in D2 corresponds to a low-level impurity of PbI_2,[84] the intense peaks at 14.04º, 28.29º, 31.80º, 40.56º and 43.07º (D1) and at 14.13º, 28.62º, 32.07º, 40.71º and 43.37º (D2) can be respectively assigned to (110), (220), (310), (224) and (314) planes of a tetragonal perovskite structure.[202] This indicates the majority of the PbI_2 has been converted into $CH_3NH_3PbI_3$ after exposure to CH_3NH_3I mist, confirming that the sequential AACVD process has successfully produced perovskite crystal materials. Although the PbI_2 peak indicates that a very small quantity of the initial material was not fully converted, it has previously been demonstrated that organometallic halide

perovskites with a small amount of PbI_2 purities are still able to achieve high device performance.[83,203,204] It is worth mentioning that the diffraction peaks for the FTO substrate are hardly observed in D1 (profound in D2). We infer this is because the upper $MAPbI_3$ perovskite layer in D1 is compact and thick, whereby the incident X-ray beam cannot penetrate through it under the glancing incidence model we selected. So the FTO layer information is not seen in the diffraction pattern of D1.

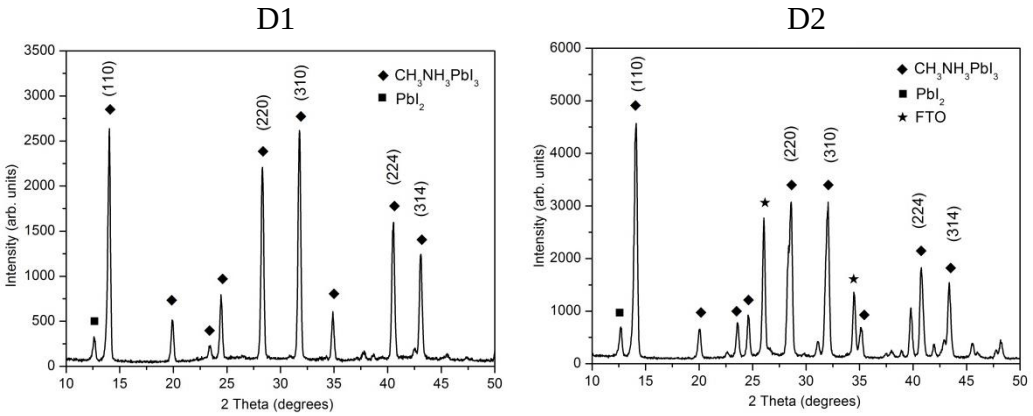

Figure 7.6 XRD patterns of the two-step AACVD $CH_3NH_3PbI_3$ films on FTO glass substrates.

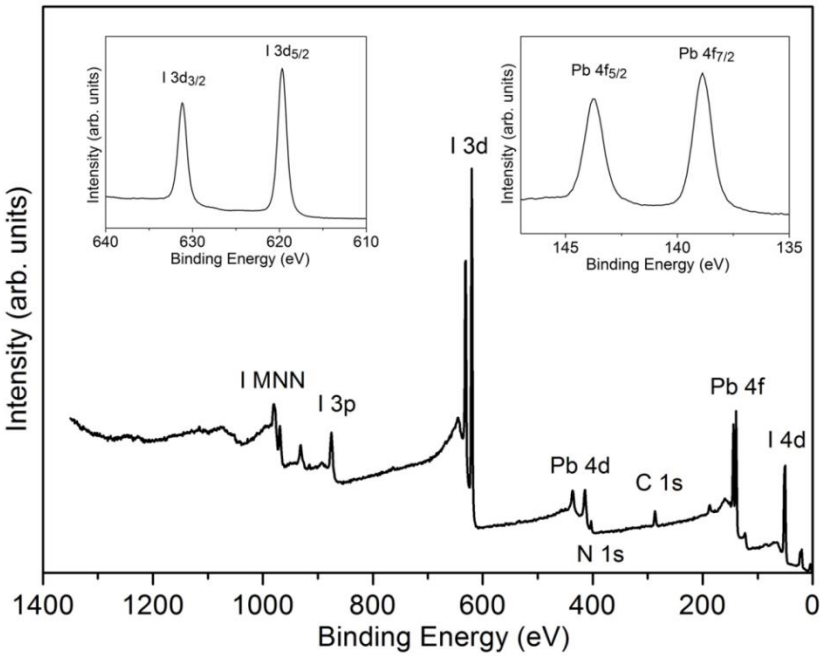

Figure 7.7 XPS survey spectrum and I 3d and Pb 4f core level spectra for sample D1.

Film surface elemental analysis was carried out by using XPS and the spectra of the representative sample D1 are presented in Fig. 7.7. The survey spectra indicate the presence of carbon, nitrogen, lead and iodide photoelectron and Auger signals. No other elements were detected in appreciable amounts. The inset of Fig. 7.4 displays the high-resolution I 3d and Pb 4f XPS photoelectron signals. The I $3d_{5/2}$ and Pb $4f_{7/2}$ core levels appear at the binding energies of 619.5 eV and 138.8 eV respectively, in good agreement with reported values in literatures.[205,206] The I:Pb atomic ratio was found to be 2.96, which is very close to the expected value of 3.0 and also supports above XRD observations well.

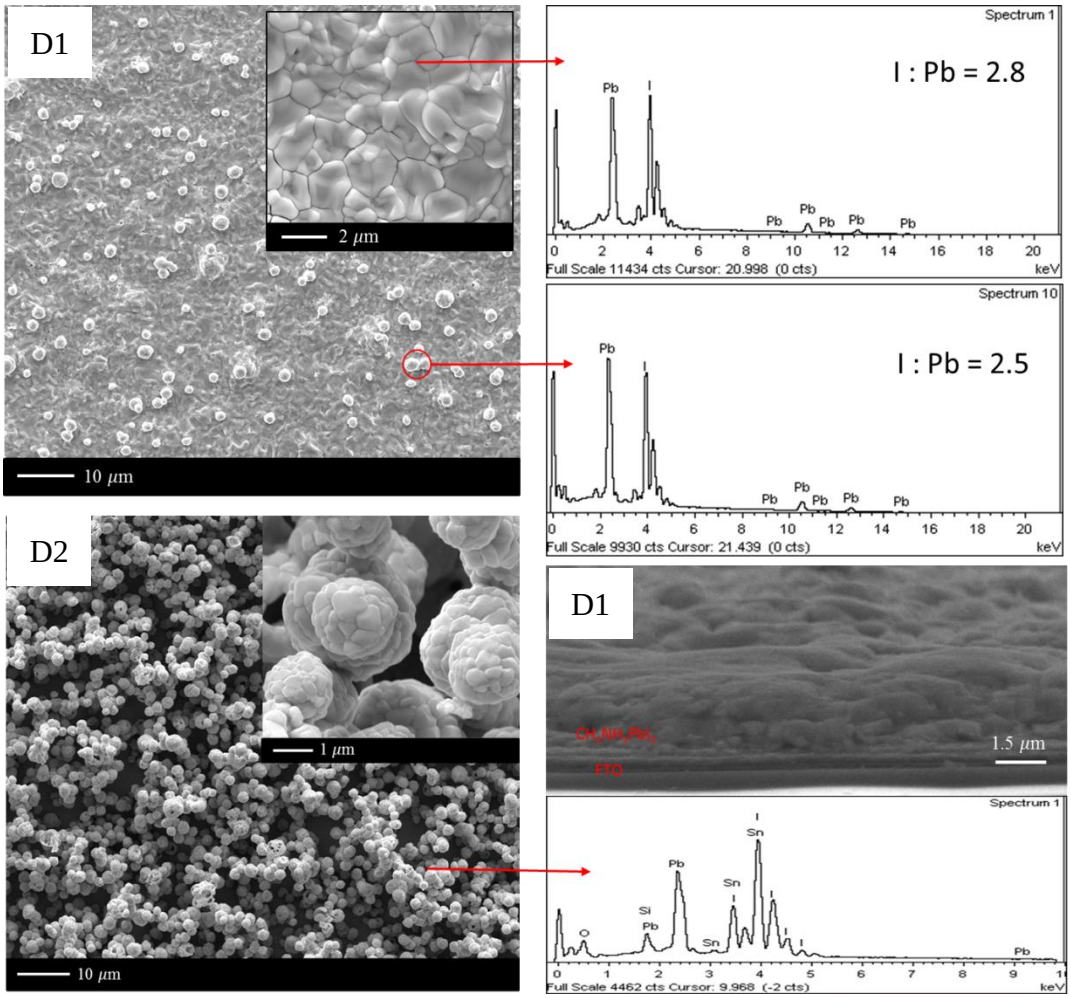

Figure 7.8 SEM images and corresponding EDS spectra of the two-step AACVD $CH_3NH_3PbI_3$ films on FTO glass substrates.

The surface morphology of $MAPbI_3$ coating was investigated through SEM analysis and the images are shown in Fig. 7.8. It is seen that the perovskite film D1 is fully covered across the studied area without any evidence of pin-holes. This clearly demonstrates that the two-step AACVD process has successfully avoided the solid-gas phase reaction in single-step depositions,[198,199] leading to a significant microstructure improvement from poorly connected particles into dense continuous films. From the inset high magnification image, the film grain size is estimated to be 1-2 μm. These large compact grains are extremely favourable for PV application because the reduced grain boundaries should help alleviate surface recombination when carriers are transported in the perovskite layer.[84] Certain spherical particles are also observed on the film surface, which can be identified as unreacted PbI_2 because their average I:Pb atomic ratio (2.5) estimated by the EDS is lower than that of grain interiors (2.8), as illustrated in Fig. 7.8. The film thickness for D1 was found to be ~1.5 μm from its cross-section SEM image (see Fig. 7.8). In optimizing planar heterojunction perovskite solar cells, perovskite film thickness is a key parameter. If the film is too thin, then that region will not absorb sufficient sunlight. If the film is too thick, there is a significant chance that the electron and hole (or exciton) diffusion length will shorter than the film thickness, and that the charge will therefore not collected at the p-type and n-type heterojunctions.[83] According to the recent studies by J. Huang *et al.*, the effective charge diffusion length in micron-sized $CH_3NH_3PbI_3$ films could be as long as 3.5 μm.[85,86] Therefore, from the perspective of perovskite film density, grain size and thickness, the AACVD $MAPbI_3$ coatings have great potential to be used as light absorber in high performance perovskite solar cells, once the surface impurities have been minimized.

By comparison, the other perovskite sample D2 is largely composed of spherical agglomerated particles (with average diameter around 2 μm), which forms a highly porous structure and cannot be utilized as a light absorber in perovskite solar cells. This porous film morphology indicates the increase of PbI_2 deposition temperature from 70 ℃ to 100 ℃ has transformed the preferred surface heterogeneous nucleation behaviour into the unfavourable gas phase homogeneous nucleation phenomena. As a result, a much higher precursor input is required to obtain a good film coverage across the glass surface, as shown in Table 7.1. Moreover, since the film is less-densely packed, the FTO substrate information therefore can be readily collected by EDS and XRD, as illustrated in Fig. 7.6 and Fig. 7.8. The film thickness for sample D2 is estimated to be larger than 5 μm from its multi-stacked particles.

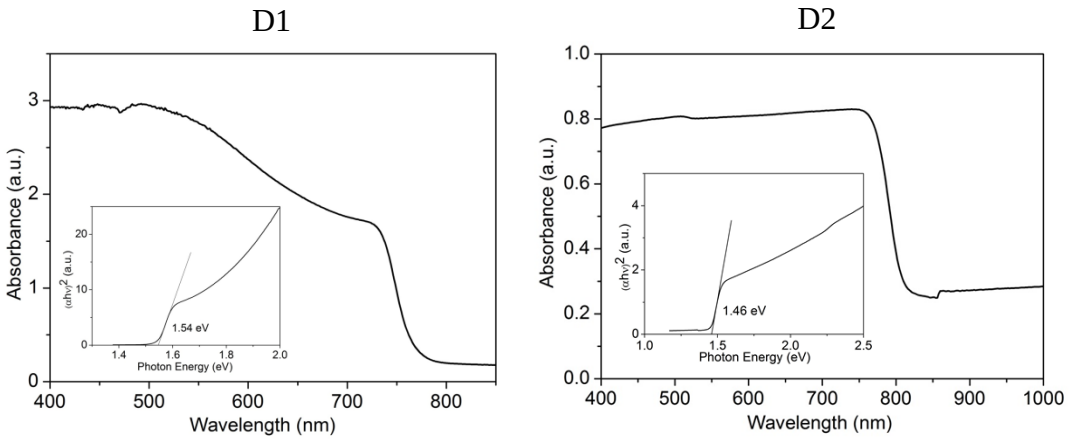

Figure 7.9 UV-Vis absorbance spectra and optical bangap plot for the two-step AACVD $CH_3NH_3PbI_3$ films on FTO glass substrates.

Finally, the evidence of perovskite-type $MAPbI_3$ can also be supported by its optical characteristics. Fig. 7.9 shows the UV-vis absorption spectrum of the $MAPbI_3$ sample on FTO substrate, in which a strong absorption ranging from 400 nm to 780 nm (D1) and 400 nm to 800 nm (D2) is clearly observed. The slight longer absorption range in D2 may relate to its porous microstructures, whereby the incident

light scattered between the particles is fully absorbed. The optical bandgap of $MAPbI_3$ film is then determined from a Tauc plot using the $(ahv)^2$ relation,[65] as illustrated in the inset of Fig. 7.9. The obtained direct band gap value of 1.54 eV (D1) and 1.46 eV (D2), estimated from the intercept by extrapolating the linear fit of the Tauc plot to energy axis, is in good agreement with previously reported data for perovskite $CH_3NH_3PbI_3$ (1.48-1.54 eV).[199,207,208]

7.4 Results and discussion for the three-step AACVD $MAPbI_3$ films

The surface morphology of the three-step AACVD $MAPbI_3$ films prepared under different film thickness were examined by SEM and the images are shown in Fig. 7.10. It is seen that all the samples, except E6, are densely packed across the studied area without any evidence of pin-holes. From the inset high magnification images, the $MAPbI_3$ grain size can be estimated to be micron scale, even their film thickness values are lower than 1 um (see Table 7.1). The grain size distribution for the 600 nm thick sample E4 is illustrated in Fig. 7.11. As observed, around 45 % of the grains inside are larger than 1 μm and the maximum grain size could reach 2.8-3 μm. The average grain size for sample D4 is then calculated to be 1.05 μm. These enlarged perovskite grains indicate the three-step AACVD process could effectively promote perovskite film crystallization.

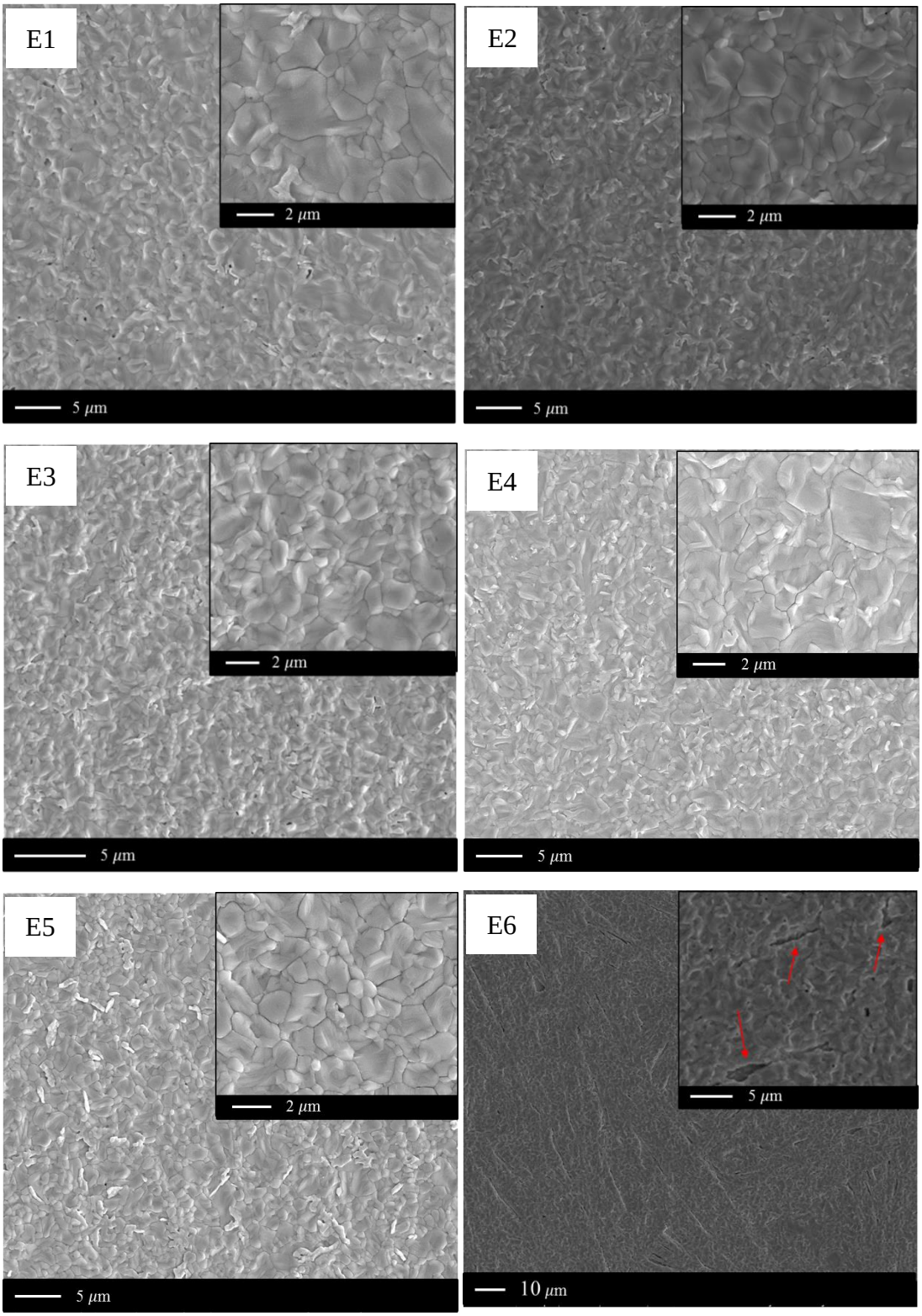

Figure 7.10 Surface SEM images for the three-step AACVD $CH_3NH_3PbI_3$ films on FTO glass substrate prepared under different film thickness. The insets show higher magnification images for corresponding sample. The red arrows in E6 refer to pin-holes.

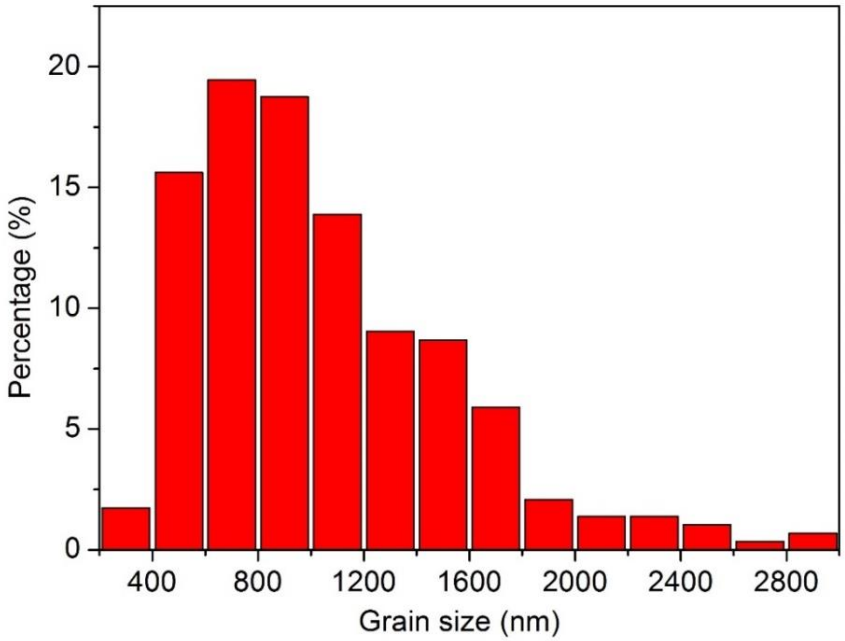

Figure 7.11 The grain size distribution in sample E4.

The unreacted PbI_2 can also be observed from the film surfaces, but these lead impurities tend to distribute evenly between the grain boundaries, such as in sample E4 and E5, instead of agglomerating into large particles on top of the surfaces as like in the two-step AACVD $MAPbI_3$ film D1. This surface modification could tremendously reduce the perovskite film surface roughness, which is beneficial for the deposition of hole transporting materials over the existing perovskite layer during device fabrication. It is worth mentioning that an appropriate amount of PbI_2 species in the $CH_3NH_3PbI_3$ film has been reported to improve the carrier behaviour by reducing the recombination in the grain boundaries, as well as in the interfaces between the absorber and the carrier transport layer.[209] However, a recent study by F. Liu *et al.* demonstrates that the presence of unreacted PbI_2 would result in an intrinsic instability of the $MAPbI_3$ film under illumination, leading to the film degradation under inert atmosphere and faster degradation upon exposure to illumination and humidity. Thus, further efforts to minimize lead iodide impurities

are still essential. This can be fulfilled by certain post-deposition treatments, such as dip the perovskite deposits into an isopropanol solution containing MAI.

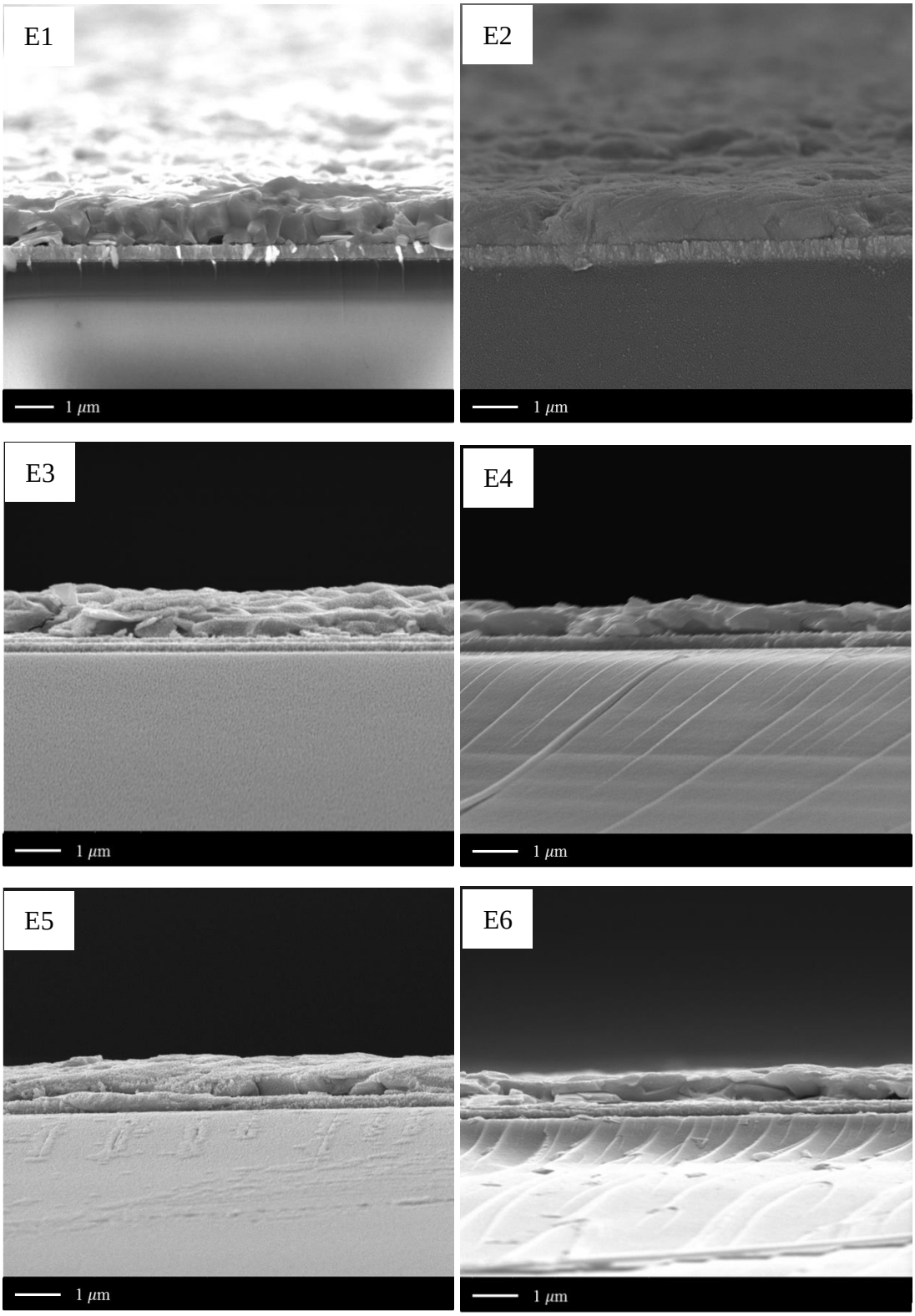

Figure 7.12 Cross-section SEM images for the three-step AACVD $CH_3NH_3PbI_3$ films on FTO glass substrate prepared under different film thickness.

The cross-section images for the three-step AACVD $MAPbI_3$ films are shown in Fig. 7.12. It is seen that these coatings are highly likely to be thickened by large continuous grains. According to the study by J. Huang *et al.*, the continuous perovskite grains would greatly enhance the charge extraction process because the photogenerated electrons and holes do not need to go through any grain boundaries during their transport in the out-of-plane direction before being collected by the electrodes.[85] The $CH_3NH_3PbI_3$ film thickness generally decreases with PbI_2 precursor input and the minimum thickness obtained is around 0.59 μm in sample E4, which is ideal for high performance perovskite solar cells.

7.5 Conclusions

In this chapter, uniform compact $CH_3NH_3PbI_3$ perovskite films have been successfully synthesised on FTO glass substrates by two-step and three-step sequential AACVD methods. This provides an important alternative to previous single-step process, offering the potential of scalable fabrication of organometallic halide perovskites with a cost-effective approach.

Chapter 8 Overall Conclusions and Future Work

8.1 Overall conclusions

The aim of this work is to fabricate thin film materials on glass substrates for energy efficient glazing and solar cells applications by use of low cost sol-gel dip coating and aerosol assisted chemical vapour deposition methods.

Chapter 4 describes the deposition of gallium doped zinc oxide films on silica glass substrates by using sol-gel dip coating method utilising zinc acetate and gallium acetylacetonate as precursors. The effects of film thickness (230-480 nm), heating temperature (400-600 ℃) and atmosphere (Air/Argon) on the ZnO structural and opto-electronic properties was investigated.

The results demonstrated that highly *c*-axis oriented crystals could be easily formed in sol-gel ZnO:Ga coatings, which originated from a preferred nucleation and got fully developed during structure evolution. An increase in film thickness prolonged the preheating process and promotes nucleation, resulting in a more crystalline film after annealing. Higher temperature annealing (600 °C) in air could degrade the Ga doping efficiency and decrease the carrier concentration, but the enlarged grain size helped enhance the carrier mobility and improve the film conductivity. Under a modified annealing process in argon, favourable carrier density (3.38×10^{19} cm^{-3}) and mobility (15.7 cm^2 $V^{-1}s^{-1}$) were obtained at the same time, resulting in a minimum film resistivity of 1.18×10^{-2} Ω cm. The studied ZnO:Ga coatings kept transparent both in the visible and near infrared light due to the insufficient carrier density.

Chapter 5 investigates the deposition of gallium doped zinc oxide films on silica glass substrates by using AACVD method utilising zinc and gallium acetylacetonates as precursors. The effects of gallium doping content (0.4-6.1 at.%), deposition temperature (350-450 °C) and time (45-135 min) on the ZnO structural and opto-electronic performances were systematically studied.

At a deposition temperature of 350 °C, highly c-axis oriented films are easily formed in the case of pure ZnO with hexagonal (002) surfaces observed. This texture is gradually weakened in 0.4 at.% to 3.0 at.% Ga doped samples, and the deposit morphology is transformed to granular particles, irregular platelets, agglomerated particles and wedge-like structures, respectively, which may result from retarded grain boundary growth and increasing exposed non-(002) surfaces. Further gallium addition to 4.3 at.% suppresses the grain growth and deteriorates the system crystallinity, with a concomitant change to a (102) preferential orientation in the heavily 6.1 at.% Ga doped sample. After the substrate temperature was increased from 400 °C to 450 °C, the preferred deposition and growth sites on glass surface change, which corresponds to a deposition mechanism transformation from surface reaction kinetics limited into mass transport limited. The resulting ZnO:Ga coatings are mainly composed by *c*-axis oriented crystallites and their crystallinity exhibits a continuous improvement with film thickness, associated with an emergence of columnar structures.

The AACVD ZnO:Ga coatings exhibited high carrier concentration (up to 5.28×10^{20} cm^{-3}) but limited carrier mobility (< 5 cm^2 $V^{-1}s^{-1}$), and the minimum resistivity value obtained was 6.5×10^{-3} Ω cm. The poor mobility performance is mainly originated from an insufficient doping efficiency with a high amount of inactive doping atoms cannot generate free electrons but act as electron scattering

centres. In spite of this, due to the large band gaps and favourable carrier numbers, high visible transmittance (> 80 %) and infrared reflection (up to 48.9 % at 2500 nm) were observed in these films, which is close to the optical requirements for commercial energy saving glazing. We firstly proved that the film infrared reflectivity was determined by the carrier density and carrier number together.

Chapter 6 probes the deposition of surface-textured zinc oxide films on FTO and silica glass substrates by using AACVD method utilising zinc-acetate-dihydrate, acetic acid and deionized water as precursors. The effects of acetic acid (0-8 mL) and D.I. water (0-4 mL) content on the ZnO structural and functional properties were investigated.

It was found that the introduction of acetic acid in precursor solutions could i) promote lateral grain growth by inhibiting the ZnO crystal nucleation, and ii) expose $\{10\bar{1}1\}$ polar facets by lowering their surface energy, which helped form pyramid-like film surfaces. The resulting ZnO coatings exhibited good optical transparency (~70 %) and ultra-large haze factor (up to 91.6 %), due to the high surface roughness (up to 103 nm). Further addition of D.I. water into precursors increased the aerosol density and narrowed the film growth region at the beginning of glass surface. In this regard, a majority of acetate ions added may have reached the glass surface, since less acetic acid would be pre-decomposed because of the much shorter traveling distance within the reactor. This large increase of acetate concentration would favour the *a*-axis oriented crystal growth, resulting in well-defined hexagonal-plate-shaped film surfaces combined with large roughness value (up to 216.6 nm). The plate-like ZnO films exhibited good visible transparency (~70 %), low sheet resistance (~60 Ω sq^{-1}) and ultra large haze factor (up to 98.5 %), which could be potentially used as the front contact in thin-film solar cells. The low film resistance was

attributed to the high oxygen vacancy concentration with the formation of large polar hexagonal plates.

Chapter 7 focuses on the deposition of methylammonium lead iodide films on FTO glass substrates using a two-step and three-step sequential AACVD method. The effect of deposition temperature and precursor content on the $MAPbI_3$ perovskite film structural properties was primarily investigated.

Large-are uniform $MAPbI_3$ perovskite films with high phase purity and micron-sized pinhole-free grains were obtained in the two-step process. This represents that the new process has successfully avoided the solid-gas phase reaction in those reported single-step depositions, leading to a significant microstructure improvement from poorly connected particles into dense continuous films. The $MAPbI_3$ film morphology can be further improved by employing a three-step sequential process, demonstrating the feasibility of making efficient perovskite solar cells via AACVD technique.

In conclusion, AACVD shows a great potential for the scalable fabrication of ZnO-based and organometallic halide-based thin film materials.

8.2 Future work

A range of ideas that could be further carried out for this project are suggested in this section, these include:

- To lower the sol-gel ZnO:Ga film resistivity to a range of 10^{-3} Ω cm, there are a number of deposition parameters can be studied. For example, a mixed annealing atmosphere of argon (majority) and oxygen may be helpful to keep low surface absorbed oxygen content and high film crystallinity at the same

time. The ratio between oxygen and argon can be tuned to optimize the ZnO:Ga film conductivity. Also the increase of coating layers to 15 or 18 and the use of higher gallium concentration in precursor solutions may improve the ZnO:Ga film properties considerably. To lower the AACVD ZnO:Ga film resistivity to a range of 10^{-4} Ω cm, certain post-deposition treatment, such as rapid thermal annealing in argon, to promote grain growth and active the neutral impurities into lattice sites may help.

- Further systematically investigation on how the pyramid-shaped and plate-shaped ZnO films are formed during the depositions would be desirable. Different deposition time can be employed to observe film morphology and structure evolution. The incorporation of these surface-textured ZnO films into photovoltaic devices is highly recommended. The pyramid-shaped ZnO films on FTO substrates can be used to fabricate CuO_2/ZnO/FTO all-oxide heterojunction solar cells. The plate-shaped ZnO coatings on pure glasses are suitable for silicon thin film solar cells once a more uniform and conductive film is obtained.

- To demonstrate the feasibility of fabricating AACVD derived perovskite solar cells, it is recommend to spin-coat the PbI_2 layer on the substrates instead of by AACVD, because currently the former is easier to form a thin uniform PbI_2 layer. After that, PbI_2 can be converted it into $MAPbI_3$ via the AACVD reaction. Further efforts should also be made to fabricate the mixed organolead halide materials, such as $MAPb(I_{1-x}Br_x)_3$. Compared to other vapour-based deposition methods, AACVD is able to precisely control the perovskite film composition since the ratio between CH_3NH_3I and CH_3NH_3Br can be easily tuned in precursor mist. It is also worth designing and

assembling a smaller CVD reactor for the perovskite film deposition, in order to obtain films with better uniformity for device fabrication.

References

[1] M. He, D. Zheng, M. Wang, C. Lin, Z. Lin, High efficiency perovskite solar cells: from complex nanostructure to planar heterojunction, J. Mater. Chem. A. 2 (2014) 5994–6003.

[2] M.E.A. Warwick, R. Binions, Advances in thermochromic vanadium dioxide films, J. Mater. Chem. A. 2 (2014) 3275.

[3] A.M. Omer, Energy, environment and sustainable development, Renew. Sustain. Energy Rev. 12 (2008) 2265–2300.

[4] M.E.A. Warwick, G. Hyett, I. Ridley, F.R. Laffir, C. Olivero, P. Chapon, et al., Synthesis and energy modelling studies of titanium oxy-nitride films as energy efficient glazing, Sol. Energy Mater. Sol. Cells. 118 (2013) 149–156.

[5] S. Chen, G. Carraro, D. Barreca, A. Sapelkin, W. Chen, X. Huang, et al., Aerosol assisted chemical vapour deposition of Ga-doped ZnO films for energy efficient glazing: effects of doping concentration on the film growth behaviour and opto-electronic properties, J. Mater. Chem. A. 3 (2015) 13039–13049.

[6] C.G. Granqvist, Transparent conductors as solar energy materials: A panoramic review, Sol. Energy Mater. Sol. Cells. 91 (2007) 1529–1598.

[7] B.-Z. Dong, G.-J. Fang, J.-F. Wang, W.-J. Guan, X.-Z. Zhao, Effect of thickness on structural, electrical, and optical properties of ZnO: Al films deposited by pulsed laser deposition, J. Appl. Phys. 101 (2007) 033713.

[8] D. Wan, F. Huang, Y. Wang, X. Mou, F. Xu, Highly Surface-Textured ZnO:Al Films Fabricated by Controlling the Nucleation and Growth Separately for Solar Cell Applications, ACS Appl. Mater. Interfaces. 2 (2010) 2147–2152.

[9] S. Faÿ, J. Steinhauser, N. Oliveira, E. Vallat-Sauvain, C. Ballif, Opto-electronic properties of rough LP-CVD ZnO:B for use as TCO in thin-film silicon solar cells, Thin Solid Films. 515 (2007) 8558–8561.

[10] Y.H. Heo, D.J. You, H. Lee, S. Lee, H.-M. Lee, ZnO:B back reflector with

high haze and low absorption enhanced triple-junction thin film Si solar modules, Sol. Energy Mater. Sol. Cells. 122 (2014) 107–111.

[11] https://www.cvdequipment.com/markets-served/tco-coatings/.

[12] S. Chen, N. Noor, I.P. Parkin, R. Binions, Temperature and thickness-dependent growth behaviour and opto-electronic properties of Ga-doped ZnO films prepared by aerosol-assisted chemical vapour deposition, J. Mater. Chem. A. 2 (2014) 17174–17182.

[13] http://www.nrel.gov/ncpv/images/efficiency_chart.jpg.

[14] H.J. Snaith, Perovskites: The Emergence of a New Era for Low-Cost, High-Efficiency Solar Cells, J. Phys. Chem. Lett. 4 (2013) 3623–3630.

[15] Y. Fu, F. Meng, M.B. Rowley, B.J. Thompson, M.J. Shearer, D. Ma, et al., Solution Growth of Single Crystal Methylammonium Lead Halide Perovskite Nanostructures for Optoelectronic and Photovoltaic Applications, J. Am. Chem. Soc. 137 (2015) 5810–5818.

[16] D. Chen, Anti-reflection (AR) coatings made by sol–gel processes: A review, Sol. Energy Mater. Sol. Cells. 68 (2001) 313–336.

[17] K.L. Choy, Chemical vapour deposition of coatings, Prog. Mater. Sci. 48 (2003) 57–170.

[18] D. Perednis, L.J. Gauckler, Thin Film Deposition Using Spray Pyrolysis, J. Electroceramics. 14 (2005) 103–111.

[19] D.M. Mattox, Handbook of Physical Vapor Deposition (PVD) Processing, William Andrew, 2010.

[20] J.A. Manzi, C.E. Knapp, I.P. Parkin, C.J. Carmalt, Aerosol-Assisted Chemical-Vapour Deposition of Zinc Oxide from Single-Source β-Iminoesterate Precursors, Eur. J. Inorg. Chem. 2015 (2015) 3658–3665.

[21] A.C. Jones, M.L. Hitchman, Chemical Vapour Deposition: Precursors, Processes and Applications, Royal Society of Chemistry, 2009.

[22] P. Marchand, I.A. Hassan, I.P. Parkin, C.J. Carmalt, Aerosol-assisted delivery of precursors for chemical vapour deposition: expanding the scope of CVD for

materials fabrication., Dalt. Trans. 42 (2013) 9406–9422.

[23] J.S. Bhat, A.S. Patil, N. Swami, B.G. Mulimani, B.R. Gayathri, N.G. Deshpande, et al., Electron irradiation effects on electrical and optical properties of sol-gel prepared ZnO films, J. Appl. Phys. 108 (2010) 043513.

[24] J.D. Wright, N.A.J.M. Sommerdijk, Sol-Gel Materials: Chemistry and Applications, CRC Press, 2000.

[25] L. Znaidi, Sol–gel-deposited ZnO thin films: A review, Mater. Sci. Eng. B. 174 (2010) 18–30.

[26] J. Livage, D. Ganguli, Sol–gel electrochromic coatings and devices: A review, Sol. Energy Mater. Sol. Cells. 68 (2001) 365–381.

[27] M. Niederberger, N. Pinna, Metal Oxide Nanoparticles in Organic Solvents, Springer London, London, 2009.

[28] H.K. Raut, V.A. Ganesh, A.S. Nair, S. Ramakrishna, Anti-reflective coatings: A critical, in-depth review, Energy Environ. Sci. 4 (2011) 3779.

[29] S.M. Attia, J. Wang, G. Wu, J. Shen, J. Ma, Review on Sol-Gel Derived Coatings: Process, Techniques and Optical Applications, J. Mater. Sci. Technol. 18 (2009) 211–217.

[30] L.D. Landau, B.G. Levich, Dynamics of Curved Fronts, Acta Physicochim. U.R.S.S. 17 (1942) 42–54.

[31] J. Polte, Fundamental growth principles of colloidal metal nanoparticles – a new perspective, CrystEngComm. 17 (2015) 6809–6830.

[32] C. V. Thompson, Structure evolution during processing of polycrystalline films, Annu. Rev. Mater. Sci. 30 (2000) 159–190.

[33] H.O. Pierson, Handbook of Chemical Vapor Deposition (CVD): Principles, Technology, and Applications, Noyes Publications, 1992.

[34] D. Dobkin, M.K. Zuraw, Principles of Chemical Vapor Deposition, Springer Science & Business Media, 2003.

[35] G.B. Stringfellow, Organometallic Vapor-Phase Epitaxy: Theory and Practice,

Academic Press, 1999.

[36] J.A. Venables, G.D.T. Spiller, M. Hanbucken, Nucleation and growth of thin films, Reports Prog. Phys. 47 (1984) 399–459.

[37] X. Hou, K.-L. Choy, Processing and Applications of Aerosol-Assisted Chemical Vapor Deposition, Chem. Vap. Depos. 12 (2006) 583–596.

[38] S. Chen, M. McLachlan, A. Sapelkin, R. Binions, Aerosol assisted chemical vapour deposition of transparent conductive ZnO thin films with hexagonal microplate surfaces and ultrahigh haze values, J. Mater. Chem. A. 3 (2015) 22311–22315.

[39] H.L. Hartagel, A.L. Dawar, A.K. Jain, C. Jagadish, Semiconducting Transparent Thin Films, Institute of Physics Publishing, Bristol, 1995.

[40] J. William S. Rees, CVD of Nonmetals, John Wiley & Sons, 2008.

[41] S.G. Mahajan, J.T. Abrahamson, S. Birkhimer, E. Friedman, Q.H. Wang, M. Beck, et al., Superadiabaticity in reaction waves as a mechanism for energy concentration, Energy Environ. Sci. 7 (2014) 3391–3402.

[42] J.M. Wallace, P. V. Hobbs, Atmospheric Science: An Introductory Survey, Academic Press, 2006.

[43] S.S. Kanu, R. Binions, Thin films for solar control applications, Proc. R. Soc. A. 466 (2009) 19–44.

[44] Z. Wu, W. Wang, Y. Cao, J. He, Q. Luo, W.A. Bhutto, et al., A beyond near-infrared response in a wide-bandgap ZnO/ZnSe coaxial nanowire solar cell by pseudomorphic layers, J. Mater. Chem. A. 2 (2014) 14571.

[45] D. Ginley, H. Hosono, D.C. Paine, Handbook of Transparent Conductors, Springer, New York, 2010.

[46] T. Yamada, H. Makino, N. Yamamoto, T. Yamamoto, Ingrain and grain boundary scattering effects on electron mobility of transparent conducting polycrystalline Ga-doped ZnO films, J. Appl. Phys. 107 (2010) 123534.

[47] P. Chand, A. Gaur, A. Kumar, Study of optical and ferroelectric behavior of ZnO nanostructures, Adv. Mater. Lett. 4 (2013) 220–224.

[48] Z.L. Wang, Zinc oxide nanostructures: growth, properties and applications, J. Phys. Condens. Matter. 16 (2004) R829–R858.

[49] http://www.wikiwand.com/en/Zinc_oxide.

[50] T.S. Herng, A. Kumar, C.S. Ong, Y.P. Feng, Y.H. Lu, K.Y. Zeng, et al., Investigation of the non-volatile resistance change in noncentrosymmetric compounds., Sci. Rep. 2 (2012) 587.

[51] S. Chen, R.M. Wilson, R. Binions, Synthesis of highly surface-textured ZnO thin films by aerosol assisted chemical vapour deposition, J. Mater. Chem. A. 3 (2015) 5794–5797.

[52] A. Janotti, C.G. Van de Walle, Fundamentals of zinc oxide as a semiconductor, Reports Prog. Phys. 72 (2009) 126501.

[53] S. Bae, S.J. Kim, D. Shin, J.-H. Ahn, B.H. Hong, Towards industrial applications of graphene electrodes, Phys. Scr. T146 (2012) 014024.

[54] X. Yu, J. Ma, F. Ji, Y. Wang, X. Zhang, C. Cheng, et al., Effects of sputtering power on the properties of ZnO:Ga films deposited by r.f. magnetron-sputtering at low temperature, J. Cryst. Growth. 274 (2005) 474–479.

[55] A.Z. Barasheed, S.R.S. Kumar, H.N. Alshareef, Temperature dependent thermoelectric properties of chemically derived gallium zinc oxide thin films, J. Mater. Chem. C. 1 (2013) 4122.

[56] J.H. Kim, B. Du Ahn, C.H. Lee, K.A. Jeon, H.S. Kang, S.Y. Lee, Effect of rapid thermal annealing on electrical and optical properties of Ga doped ZnO thin films prepared at room temperature, J. Appl. Phys. 100 (2006) 113515.

[57] W.W. Wenas, A. Yamada, K. Takahashi, M. Yoshino, M. Konagai, Electrical and optical properties of boron-doped ZnO thin films for solar cells grown by metalorganic chemical vapor deposition, J. Appl. Phys. 70 (1991) 7119.

[58] J. Hu, R.G. Gordon, Textured aluminum-doped zinc oxide thin films from atmospheric pressure chemical-vapor deposition, J. Appl. Phys. 71 (1992) 880.

[59] J. Hu, R.G. Gordon, Atmospheric pressure chemical vapor deposition of gallium doped zinc oxide thin films from diethyl zinc, water, and triethyl

gallium, J. Appl. Phys. 72 (1992) 5381.

[60] J. Hu, R.G. Gordon, Electrical and Optical Properties of Indium Doped Zinc Oxide Films Prepared by Atmospheric Pressure Chemical Vapor Deposition, MRS Proc. 283 (1992) 891.

[61] A. Tiburcio-Silver, A. Sanchez-Juarez, A. Avila-Garcia, Properties of gallium-doped ZnO deposited onto glass by spray pyrolysis, Sol. Energy Mater. Sol. Cells. 55 (1998) 3–10.

[62] C. Erginsoy, Neutral Impurity Scattering in Semiconductors, Phys. Rev. 79 (1950) 1013–1014.

[63] R.M. Pasquarelli, D.S. Ginley, R. O'Hayre, Solution processing of transparent conductors: from flask to film., Chem. Soc. Rev. 40 (2011) 5406–41.

[64] N. Naghavi, C. Marcel, L. Dupont, A. Rougier, J.-B. Leriche, C. Guéry, Structural and physical characterisation of transparent conducting pulsed laser deposited In_2O_3–ZnO thin films, J. Mater. Chem. 10 (2000) 2315–2319.

[65] J. Tauc, Optical properties and electronic structure of amorphous Ge and Si, Mater. Res. Bull. 3 (1968) 37–46.

[66] C.S. Chua, D. Ansovini, C.J.J. Lee, Y.T. Teng, L.T. Ong, D. Chi, et al., The effect of crystallinity on photocatalytic performance of Co_3O_4 water-splitting cocatalysts., Phys. Chem. Chem. Phys. 18 (2016) 5172–8.

[67] L.K. Ono, M.R. Leyden, S. Wang, Y. Qi, Organometal halide perovskite thin films and solar cells by vapor deposition, J. Mater. Chem. A. (2016).

[68] W.S. Yang, J.H. Noh, N.J. Jeon, Y.C. Kim, S. Ryu, J. Seo, et al., High-performance photovoltaic perovskite layers fabricated through intramolecular exchange, Science. 348 (2015) 1234–7.

[69] M.A. Green, A. Ho-Baillie, H.J. Snaith, The emergence of perovskite solar cells, Nat. Photonics. 8 (2014) 506–514.

[70] Q. Chen, N. De Marco, Y. (Michael) Yang, T.-B. Song, C.-C. Chen, H. Zhao, et al., Under the spotlight: The organic–inorganic hybrid halide perovskite for

optoelectronic applications, Nano Today. 10 (2015) 355–396.

[71] S.D. Stranks, G.E. Eperon, G. Grancini, C. Menelaou, M.J.P. Alcocer, T. Leijtens, et al., Electron-hole diffusion lengths exceeding 1 micrometer in an organometal trihalide perovskite absorber, Science. 342 (2013) 341–4.

[72] J.H. Noh, S.H. Im, J.H. Heo, T.N. Mandal, S. Il Seok, Chemical management for colorful, efficient, and stable inorganic-organic hybrid nanostructured solar cells, Nano Lett. 13 (2013) 1764–9.

[73] J. Seo, S. Park, Y. Chan Kim, N.J. Jeon, J.H. Noh, S.C. Yoon, et al., Benefits of very thin PCBM and LiF layers for solution-processed p–i–n perovskite solar cells, Energy Environ. Sci. 7 (2014) 2642.

[74] G.E. Eperon, S.D. Stranks, C. Menelaou, M.B. Johnston, L.M. Herz, H.J. Snaith, Formamidinium lead trihalide: a broadly tunable perovskite for efficient planar heterojunction solar cells, Energy Environ. Sci. 7 (2014) 982.

[75] T.-B. Song, Q. Chen, H. Zhou, C. Jiang, H.-H. Wang, Y. (Michael) Yang, et al., Perovskite solar cells: film formation and properties, J. Mater. Chem. A. 3 (2015) 9032–9050.

[76] Y. Zhao, K. Zhu, Organic–inorganic hybrid lead halide perovskites for optoelectronic and electronic applications, Chem. Soc. Rev. 45 (2016) 655–689.

[77] M.R. Filip, G.E. Eperon, H.J. Snaith, F. Giustino, Steric engineering of metal-halide perovskites with tunable optical band gaps, Nat. Commun. 5 (2014) 5757.

[78] G. Xing, N. Mathews, S. Sun, S.S. Lim, Y.M. Lam, M. Grätzel, et al., Long-range balanced electron- and hole-transport lengths in organic-inorganic CH3NH3PbI3, Science. 342 (2013) 344–347.

[79] S.M.H. Qaid, M.S. Al Sobaie, M.A. Majeed Khan, I.M. Bedja, F.H. Alharbi, M.K. Nazeeruddin, et al., Band-gap tuning of lead halide perovskite using a single step spin-coating deposition process, Mater. Lett. 164 (2016) 498–501.

[80] S. Sun, T. Salim, N. Mathews, M. Duchamp, C. Boothroyd, G. Xing, et al., The origin of high efficiency in low-temperature solution-processable bilayer

organometal halide hybrid solar cells, Energy Environ. Sci. 7 (2014) 399–407.

[81] J. Kim, S.-H. Lee, J.H. Lee, K.-H. Hong, The Role of Intrinsic Defects in Methylammonium Lead Iodide Perovskite, J. Phys. Chem. Lett. 5 (2014) 1312–7.

[82] Q. Dong, Y. Fang, Y. Shao, P. Mulligan, J. Qiu, L. Cao, et al., Electron-hole diffusion lengths > 175 μm in solution grown $CH_3NH_3PbI_3$ single crystals, Science. 347 (2015) 967–70.

[83] M. Liu, M.B. Johnston, H.J. Snaith, Efficient planar heterojunction perovskite solar cells by vapour deposition, Nature. 501 (2013) 395–8.

[84] Q. Chen, H. Zhou, Z. Hong, S. Luo, H.-S. Duan, H.-H. Wang, et al., Planar heterojunction perovskite solar cells via vapor-assisted solution process, J. Am. Chem. Soc. 136 (2014) 622–625.

[85] Z. Xiao, Q. Dong, C. Bi, Y. Shao, Y. Yuan, J. Huang, Solvent annealing of perovskite-induced crystal growth for photovoltaic-device efficiency enhancement, Adv. Mater. 26 (2014) 6503–9.

[86] Y. Deng, E. Peng, Y. Shao, Z. Xiao, Q. Dong, J. Huang, Scalable fabrication of efficient organolead trihalide perovskite solar cells with doctor-bladed active layers, Energy Environ. Sci. 8 (2015) 1544–1550.

[87] G. Frank, E. Kauer, H. Köstlin, F.J. Schmitte, Transparent heat-reflecting coatings for solar applications based on highly doped tin oxide and indium oxide, Sol. Energy Mater. 8 (1983) 387–398.

[88] M.W. Zhu, J. Gong, C. Sun, J.H. Xia, X. Jiang, Investigation of correlation between the microstructure and electrical properties of sol-gel derived ZnO based thin films, J. Appl. Phys. 104 (2008) 073113.

[89] D.S. Bhachu, G. Sankar, I.P. Parkin, Aerosol Assisted Chemical Vapor Deposition of Transparent Conductive Zinc Oxide Films, Chem. Mater. 24 (2012) 4704–4710.

[90] V. Musat, B. Teixeira, E. Fortunato, R.C.. Monteiro, P. Vilarinho, Al-doped ZnO thin films by sol–gel method, Surf. Coatings Technol. 180-181 (2004) 659–662.

[91] A.M.T.M.L. Castaner, Practical Handbook of Photovoltaics: Fundamentals and Applications, Academic Press, 2011.

[92] http://www.pveducation.org/pvcdrom/solar-cell-operation/solar-cell-structure.

[93] M.T. Kibria, A. Ahammed, S.M. Sony, F. Hossain, A Review : Comparative studies on different generation solar cells technology, Int. Conf. Environ. Asp. Bangladesh. (2014) 51–53.

[94] B. Liu, X. Liang, J. Liang, L. Bai, H. Gao, Z. Chen, et al., Broadband light trapping based on periodically textured ZnO thin films, Nanoscale. 7 (2015) 9816–24.

[95] M. Boccard, P. Cuony, C. Battaglia, S. Hänni, S. Nicolay, L. Ding, et al., Nanometer- and Micrometer-Scale Texturing for High-Efficiency Micromorph Thin-Film Silicon Solar Cells, IEEE J. Photovoltaics. 2 (2012) 83–87.

[96] T. Shinagawa, K. Shibata, O. Shimomura, M. Chigane, R. Nomura, M. Izaki, Solution-processed high-haze ZnO pyramidal textures directly grown on a TCO substrate and the light-trapping effect in Cu_2O solar cells, J. Mater. Chem. C. 2 (2014) 2908.

[97] Z. Hu, J. Zhang, Y. Zhao, Effect of textured electrodes with light-trapping on performance of polymer solar cells, J. Appl. Phys. 111 (2012) 104516.

[98] T. Chih-Hung, H. Sui-Ying, H. Tsung-Wei, T. Yu-Tang, C. Yan-Fang, Y.H. Jhang, et al., Influences of textures in fluorine-doped tin oxide on characteristics of dye-sensitized solar cells, Org. Electron. 12 (2011) 2003–2011.

[99] C. Battaglia, C.-M. Hsu, K. Söderström, J. Escarré, F.-J. Haug, M. Charrière, et al., Light trapping in solar cells: can periodic beat random?, ACS Nano. 6 (2012) 2790–7.

[100] O. Kluth, B. Rech, L. Houben, S. Wieder, G. Schöpe, C. Beneking, et al., Texture etched ZnO:Al coated glass substrates for silicon based thin film solar cells, Thin Solid Films. 351 (1999) 247–253.

[101] M.M. Lee, J. Teuscher, T. Miyasaka, T.N. Murakami, H.J. Snaith, Efficient

hybrid solar cells based on meso-superstructured organometal halide perovskites, Science. 338 (2012) 643–7.

[102] H.S. Jung, N.-G. Park, Perovskite Solar Cells: From Materials to Devices, Small. 11 (2015) 10–25.

[103] T. Salim, S. Sun, Y. Abe, A. Krishna, A.C. Grimsdale, Y.-M. Lam, Perovskite-Based Solar Cells: Impact of Morphology and Device Architecture on Device Performance, J. Mater. Chem. A. 3 (2015) 8943–8969.

[104] H. Hu, D. Wang, Y. Zhou, J. Zhang, S. Lv, S. Pang, et al., Vapour-based processing of hole-conductor-free $CH_3NH_3PbI_3$ perovskite/C_{60} fullerene planar solar cells, RSC Adv. 4 (2014) 28964.

[105] M.R. Leyden, L.K. Ono, S.R. Raga, Y. Kato, S. Wang, Y. Qi, High Performance Perovskite Solar Cells by Hybrid Chemical Vapor Deposition, J. Mater. Chem. A. 2 (2014) 18742–18745.

[106] S. Shi, Y. Li, X. Li, H. Wang, Advancements in all-solid-state hybrid solar cells based on organometal halide perovskites, Mater. Horiz. 2 (2015) 378–405.

[107] P. Gao, M. Grätzel, M.K. Nazeeruddin, Organohalide lead perovskites for photovoltaic applications, Energy Environ. Sci. 7 (2014) 2448.

[108] S. Chen, J. Briscoe, Y. Shi, K. Chen, R. Wilson, S. Dunn, et al., A simple, low-cost CVD route to high quality $CH_3NH_3PbI_3$ perovskite thin films, CrystEngComm. 17 (2015) 7486–7489.

[109] S. R. Raga, L.K. Ono, Y. Qi, Rapid Perovskite Formation by CH_3NH_2 Gas-Induced Intercalation and Reaction of PbI_2, J. Mater. Chem. A. 4 (2015) 2494–2500.

[110] http://www.rigaku.com/en/products/xrd/ultima/app029.

[111] R.W. Schwartz, P.G. Clem, J.A. Voigt, E.R. Byhoff, M. Van Stry, T.J. Headley, et al., Control of Microstructure and Orientation in Solution-Deposited $BaTiO_3$ and $SrTiO_3$ Thin Films, J. Am. Ceram. Soc. 82 (1999) 2359–2367.

[112] Y. Natsume, H. Sakata, Electrical and optical properties of zinc oxide films post-annealed in H_2 after fabrication by sol–gel process, Mater. Chem. Phys. 78 (2003) 170–176.

[113] M. Zhu, H. Huang, J. Gong, C. Sun, X. Jiang, Role of oxygen desorption during vacuum annealing in the improvement of electrical properties of aluminum doped zinc oxide films synthesized by sol gel method, J. Appl. Phys. 102 (2007) 043106.

[114] J.-P. Lin, J.-M. Wu, The effect of annealing processes on electronic properties of sol-gel derived Al-doped ZnO films, Appl. Phys. Lett. 92 (2008) 134103.

[115] V. Musat, B. Teixeira, E. Fortunato, R.C.C. Monteiro, Effect of post-heat treatment on the electrical and optical properties of ZnO:Al thin films, Thin Solid Films. 502 (2006) 219–222.

[116] K.Y. Cheong, N. Muti, S.R. Ramanan, Electrical and optical studies of ZnO:Ga thin films fabricated via the sol–gel technique, Thin Solid Films. 410 (2002) 142–146.

[117] K. Lin, Y.-Y. Chen, Improvement of electrical properties of sol–gel derived ZnO:Ga films by infrared heating method, J. Sol-Gel Sci. Technol. 51 (2009) 215–221.

[118] C.-Y. Tsay, K.-S. Fan, C.-M. Lei, Synthesis and characterization of sol–gel derived gallium-doped zinc oxide thin films, J. Alloys Compd. 512 (2012) 216–222.

[119] P.K. Nayak, J. Yang, J. Kim, S. Chung, J. Jeong, C. Lee, et al., Spin-coated Ga-doped ZnO transparent conducting thin films for organic light-emitting diodes, J. Phys. D. Appl. Phys. 42 (2009) 035102.

[120] C.D. Wagner, Handbook of x-ray photoelectron spectroscopy: a reference book of standard data for use in x-ray photoelectron spectroscopy, Physical Electronics Division, Perkin-Elmer Corp., 1979.

[121] Http://srdata.nist.gov/xps/.

[122] M. Hellwig, K. Xu, D. Barreca, A. Gasparotto, M. Winter, E. Tondello, et al., Novel Gallium Complexes with Malonic Diester Anions as Molecular

Precursors for the MOCVD of Ga_2O_3 Thin Films, Eur. J. Inorg. Chem. 2009 (2009) 1110–1117.

[123] J. Zhang, X.F. Li, J.G. Lu, Z.Z. Ye, L. Gong, P. Wu, et al., Performance and stability of amorphous InGaZnO thin film transistors with a designed device structure, J. Appl. Phys. 110 (2011) 084509.

[124] Joint Committee Powder Diffraction Standards, Powder Diffraction File (Data File 36-1451).

[125] S. Liang, X. Bi, Structure, conductivity, and transparency of Ga-doped ZnO thin films arising from thickness contributions, J. Appl. Phys. 104 (2008) 113533.

[126] V. Gupta, A. Mansingh, Influence of postdeposition annealing on the structural and optical properties of sputtered zinc oxide film, J. Appl. Phys. 80 (1996) 1063–1073.

[127] C.-Y. Tsay, W.-T. Hsu, Sol–gel derived undoped and boron-doped ZnO semiconductor thin films: Preparation and characterization, Ceram. Int. 39 (2013) 7425–7432.

[128] H. Kim, J.S. Horwitz, G. Kushto, A. Piqué, Z.H. Kafafi, C.M. Gilmore, et al., Effect of film thickness on the properties of indium tin oxide thin films, J. Appl. Phys. 88 (2000) 6021.

[129] G.-G. Wang, J. Zeng, J.-C. Han, L.-Y. Wang, Highly transparent and conductive Ga-doped ZnO films with good thermal stability prepared by dual-target reactive sputtering, Mater. Lett. 137 (2014) 307–310.

[130] D.L. Zhu, Q. Wang, S. Han, P.J. Cao, W.J. Liu, F. Jia, et al., Optimization of process parameters for the electrical properties in Ga-doped ZnO thin films prepared by r.f. magnetron sputtering, Appl. Surf. Sci. 298 (2014) 208–213.

[131] J.M. Stiegler, R. Tena-Zaera, O. Idigoras, A. Chuvilin, R. Hillenbrand, Correlative infrared-electron nanoscopy reveals the local structure-conductivity relationship in zinc oxide nanowires, Nat. Commun. 3 (2012) 1131.

[132] J. Wang, Z. Wang, B. Huang, Y. Ma, Y. Liu, X. Qin, et al., Oxygen vacancy

induced band-gap narrowing and enhanced visible light photocatalytic activity of ZnO, ACS Appl. Mater. Interfaces. 4 (2012) 4024–30.

[133] P. Nunes, E. Fortunato, R. Martins, Influence of the post-treatment on the properties of ZnO thin films, Thin Solid Films. 383 (2001) 277–280.

[134] Q.-B. Ma, Z.-Z. Ye, H.-P. He, L.-P. Zhu, J.-Y. Huang, Y.-Z. Zhang, et al., Influence of annealing temperature on the properties of transparent conductive and near-infrared reflective ZnO:Ga films, Scr. Mater. 58 (2008) 21–24.

[135] S. Kim, J. Seo, H.W. Jang, J. Bang, W. Lee, T. Lee, et al., Effects of H2 ambient annealing in fully 002-textured ZnO:Ga thin films grown on glass substrates using RF magnetron co-sputter deposition, Appl. Surf. Sci. 255 (2009) 4616–4622.

[136] K.-H. Lim, K. Kim, S. Kim, S.Y. Park, H. Kim, Y.S. Kim, UV-Visible Spectroscopic Analysis of Electrical Properties in Alkali Metal-Doped Amorphous Zinc Tin Oxide Thin-Film Transistors, Adv. Mater. 25 (2013) 2994–3000.

[137] Y.-Y. Chen, J.-C. Hsu, C.-Y. Lee, P.W. Wang, Influence of oxygen partial pressure on structural, electrical, and optical properties of Al-doped ZnO film prepared by the ion beam co-sputtering method, J. Mater. Sci. 48 (2012) 1225–1230.

[138] G.C. Park, S.M. Hwang, J.H. Lim, J. Joo, Growth behavior and electrical performance of Ga-doped ZnO nanorod/p-Si heterojunction diodes prepared using a hydrothermal method, Nanoscale. 6 (2014) 1840–7.

[139] H. Wang, S. Baek, J. Song, J. Lee, S. Lim, Microstructural and optical characteristics of solution-grown Ga-doped ZnO nanorod arrays, Nanotechnology. 19 (2008) 075607.

[140] R. Elleuch, R. Salhi, N. Maalej, J.-L. Deschanvres, R. Maalej, Structural and luminescence correlation of annealed Er-ZnO/Si thin films deposited by AACVD process, Mater. Sci. Eng. B. 178 (2013) 1124–1129.

[141] M.R. Waugh, G. Hyett, I.P. Parkin, Zinc Oxide Thin Films Grown by Aerosol Assisted CVD, Chem. Vap. Depos. 14 (2008) 366–372.

[142] M.A. Ehsan, H.N. Ming, M. Misran, Z. Arifin, E.R.T. Tiekink, A.P. Safwan, et al., Effect of AACVD Processing Parameters on the Growth of Greenockite (CdS) Thin Films using a Single-Source Cadmium Precursor, Chem. Vap. Depos. 18 (2012) 191–200.

[143] M.G. Nolan, J.A. Hamilton, S. O'Brien, G. Bruno, L. Pereira, E. Fortunato, et al., The characterisation of aerosol assisted CVD conducting, photocatalytic indium doped zinc oxide films, J. Photochem. Photobiol. A Chem. 219 (2011) 10–15.

[144] G. Walters, I.P. Parkin, Aerosol assisted chemical vapour deposition of ZnO films on glass with noble metal and p-type dopants; use of dopants to influence preferred orientation, Appl. Surf. Sci. 255 (2009) 6555–6560.

[145] M. Zhang, Y. Nakayama, L. Pan, Synthesis of Carbon Tubule Nanocoils in High Yield Using Iron-Coated Indium Tin Oxide as Catalyst, Jpn. J. Appl. Phys. 39 (2000) L1242–L1244.

[146] D. Bekermann, A. Gasparotto, D. Barreca, L. Bovo, A. Devi, R.A. Fischer, et al., Highly Oriented ZnO Nanorod Arrays by a Novel Plasma Chemical Vapor Deposition Process, Cryst. Growth Des. 10 (2010) 2011–2018.

[147] A.A. Ramadan, A.A. Abd El-Mongy, A.M. El-Shabiny, A.T. Mater, S.H. Mostafa, E.A. El-Sheheedy, et al., Addressing difficulties in using XRD intensity for structural study of thin films, Cryst. Res. Technol. 44 (2009) 111–116.

[148] E.-K. Jeong, D.-H. Kim, I.-S. Kim, S.-Y. Choi, Enhancement of the Light Emissions from Ag Doped ZnO Thin Films by Post-Annealing Process in Air, ECS Trans. 11 (2007) 193–201.

[149] X.-L. Li, Z.-L. Wang, X.-F. Qin, H.-S. Wu, X.-H. Xu, G.A. Gehring, Enhancement of magnetic moment of Co-doped ZnO films by postannealing in vacuum, J. Appl. Phys. 103 (2008) 023911.

[150] W. Lin, K. Ding, Z. Lin, J. Zhang, J. Huang, F. Huang, The growth and investigation on Ga-doped ZnO single crystals with high thermal stability and high carrier mobility, CrystEngComm. 13 (2011) 3338.

[151] J. Briscoe, D.E. Gallardo, S. Dunn, In situ antimony doping of solution-grown ZnO nanorods, Chem. Commun. (Camb). (2009) 1273–5.

[152] D. Köhl, G. Natarajan, M. Wuttig, Structure control of sputtered zinc oxide films by utilizing zinc oxide seed layers tailored by ion beam assisted sputtering, J. Phys. D. Appl. Phys. 45 (2012) 245302.

[153] X. Zhou, Z.-X. Xie, Z.-Y. Jiang, Q. Kuang, S.-H. Zhang, T. Xu, et al., Formation of ZnO hexagonal micro-pyramids: a successful control of the exposed polar surfaces with the assistance of an ionic liquid, Chem. Commun. 1 (2005) 5572–4.

[154] M. Podlogar, J.J. Richardson, D. Vengust, N. Daneu, Z. Samardžija, S. Bernik, et al., Growth of Transparent and Conductive Polycrystalline (0001)-ZnO Films on Glass Substrates Under Low-Temperature Hydrothermal Conditions, Adv. Funct. Mater. 22 (2012) 3136–3145.

[155] B. Liu, M. Gu, X. Liu, S. Huang, C. Ni, First-principles study of fluorine-doped zinc oxide, Appl. Phys. Lett. 97 (2010) 122101.

[156] Y.-J. Choi, H.-H. Park, A simple approach to the fabrication of fluorine-doped zinc oxide thin films by atomic layer deposition at low temperatures and an investigation into the growth mode, J. Mater. Chem. C. 2 (2014) 98.

[157] I. Petrov, P.B. Barna, L. Hultman, J.E. Greene, Microstructural evolution during film growth, J. Vac. Sci. Technol. A. 21 (2003) S117.

[158] G.-D. Yuan, W.-J. Zhang, J.-S. Jie, X. Fan, J.-X. Tang, I. Shafiq, et al., Tunable n-Type Conductivity and Transport Properties of Ga-doped ZnO Nanowire Arrays, Adv. Mater. 20 (2008) 168–173.

[159] D.-J. Lee, K.-J. Kim, S.-H. Kim, J.-Y. Kwon, J. Xu, K.-B. Kim, Atomic layer deposition of Ti-doped ZnO films with enhanced electron mobility, J. Mater. Chem. C. 1 (2013) 4761.

[160] H.K. Yadav, K. Sreenivas, V. Gupta, Influence of postdeposition annealing on the structural and optical properties of cosputtered Mn doped ZnO thin films, J. Appl. Phys. 99 (2006) 083507.

[161] K. Yim, C. Lee, Dependence of the electrical and optical properties of

sputter-deposited ZnO:Ga films on the annealing temperature, time, and atmosphere, J. Mater. Sci. Mater. Electron. 18 (2006) 385–390.

[162] N. Rashidi, V.L. Kuznetsov, J.R. Dilworth, M. Pepper, P.J. Dobson, P.P. Edwards, Highly conducting and optically transparent Si-doped ZnO thin films prepared by spray pyrolysis, J. Mater. Chem. C. 1 (2013) 6960.

[163] E. Burstein, Anomalous Optical Absorption Limit in InSb, Phys. Rev. 93 (1954) 632–633.

[164] T.S. Moss, The Interpretation of the Properties of Indium Antimonide, Proc. Phys. Soc. Sect. B. 67 (1954) 775–782.

[165] P. Banerjee, W.-J. Lee, K.-R. Bae, S.B. Lee, G.W. Rubloff, Structural, electrical, and optical properties of atomic layer deposition Al-doped ZnO films, J. Appl. Phys. 108 (2010) 043504.

[166] Y.-S. Lee, Y.-C. Peng, J.-H. Lu, Y.-R. Zhu, H.-C. Wu, Electronic and optical properties of Ga-doped ZnO, Thin Solid Films. 570 (2014) 464–470.

[167] S.-H. Ko Park, Y.E. Lee, Controlling preferred orientation of ZnO thin films by atomic layer deposition, J. Mater. Sci. 39 (2004) 2195–2197.

[168] M. Steglich, A. Bingel, G. Jia, F. Falk, Atomic layer deposited ZnO:Al for nanostructured silicon heterojunction solar cells, Sol. Energy Mater. Sol. Cells. 103 (2012) 62–68.

[169] C.H. Ahn, S.Y. Lee, H.K. Cho, Influence of growth temperature on the electrical and structural characteristics of conductive Al-doped ZnO thin films grown by atomic layer deposition, Thin Solid Films. 545 (2013) 106–110.

[170] N. Qin, Q. Xiang, H. Zhao, J. Zhang, J. Xu, Evolution of ZnO microstructures from hexagonal disk to prismoid, prism and pyramid and their crystal facet-dependent gas sensing properties, CrystEngComm. 16 (2014) 7062.

[171] S. Shoaee, J. Briscoe, J.R. Durrant, S. Dunn, Acoustic enhancement of polymer/ZnO nanorod photovoltaic device performance, Adv. Mater. 26 (2014) 263–8.

[172] Y.H. Leung, Z.B. He, L.B. Luo, C.H.A. Tsang, N.B. Wong, W.J. Zhang, et al.,

ZnO nanowires array p-n homojunction and its application as a visible-blind ultraviolet photodetector, Appl. Phys. Lett. 96 (2010) 053102.

[173] L. Loh, S. Dunn, Recent Progress in ZnO-Based Nanostructured Ceramics in Solar Cell Applications, J. Nanosci. Nanotechnol. 12 (2012) 8215–8230.

[174] J. Liu, X. Chen, W. Wang, Y. Liu, Q. Huang, Z. Guo, Self-assembly of [10$\bar{1}$0] grown ZnO nanowhiskers with exposed reactive (0001) facets on hollow spheres and their enhanced gas sensitivity, CrystEngComm. 13 (2011) 3425.

[175] A. McLaren, T. Valdes-Solis, G. Li, S.C. Tsang, Shape and size effects of ZnO nanocrystals on photocatalytic activity, J. Am. Chem. Soc. 131 (2009) 12540–1.

[176] Z.R. Tian, J.A. Voigt, J. Liu, B. McKenzie, M.J. McDermott, M.A. Rodriguez, et al., Complex and oriented ZnO nanostructures, Nat. Mater. 2 (2003) 821–6.

[177] N.J. Nicholas, G. V Franks, W.A. Ducker, Selective adsorption to particular crystal faces of ZnO, Langmuir. 28 (2012) 7189–96.

[178] http://www.engineeringtoolbox.com/liquids-densities-d_743.html.

[179] Q. Kuang, X. Zhou, L.-S. Zheng, Hexagonal ZnO/SnO_2 core–shell micropyramids: epitaxial growth-based synthesis, chemical conversion, and cathodoluminescence, Inorg. Chem. Front. 1 (2014) 186.

[180] T. Shinagawa, M. Izaki, Morphological evolution of ZnO nanorod arrays induced by a pH-buffering effect during electrochemical deposition, RSC Adv. 4 (2014) 30999.

[181] S. Yamabi, H. Imai, Growth conditions for wurtzite zinc oxide films in aqueous solutions, J. Mater. Chem. (2002) 3773–3778.

[182] H. Yin, Z. Xu, Q. Wang, J. Bai, H. Bao, Study of assembling ZnO nanorods into chrysanthemum-like crystals, Mater. Chem. Phys. 91 (2005) 130–133.

[183] N.P. Herring, K. AbouZeid, M.B. Mohamed, J. Pinsk, M.S. El-Shall, Formation mechanisms of gold-zinc oxide hexagonal nanopyramids by heterogeneous nucleation using microwave synthesis, Langmuir. 27 (2011)

15146–54.

[184] K. Govender, D.S. Boyle, P.B. Kenway, P.O. Brien, Understanding the factors that govern the deposition and morphology of thin films of ZnO from aqueous solution, J. Mater. Chem. 14 (2004) 2575–2591.

[185] B.D. Andeen, J.H. Kim, F.F. Lange, G.K.L. Goh, S. Tripathy, Lateral Epitaxial Overgrowth of ZnO in Water at 90 ° C, Adv. Funct. Mater. (2006) 799–804.

[186] J. Yahiro, T. Kawano, H. Imai, Nanometric morphological variation of zinc oxide crystals using organic molecules with carboxy and sulfonic groups, J. Colloid Interface Sci. 310 (2007) 302–311.

[187] Q. Kuang, Z.-Y. Jiang, Z.-X. Xie, S.-C. Lin, Z.-W. Lin, S.-Y. Xie, et al., Tailoring the optical property by a three-dimensional epitaxial heterostructure: a case of ZnO/SnO_2, J. Am. Chem. Soc. 127 (2005) 11777–84.

[188] L. Ding, M. Boccard, G. Bugnon, M. Benkhaira, S. Nicolay, M. Despeisse, et al., Highly transparent ZnO bilayers by LP-MOCVD as front electrodes for thin-film micromorph silicon solar cells, Sol. Energy Mater. Sol. Cells. 98 (2012) 331–336.

[189] C.-P. Liu, J. Xin, L. Wang, J. Song, A.Y.S. Lee, P. Ho, Low-temperature solution growth of textured zinc oxide films for light trapping enhancement in thin film silicon solar cells, RSC Adv. 4 (2014) 34669.

[190] P.F. Cai, J.B. You, X.W. Zhang, J.J. Dong, X.L. Yang, Z.G. Yin, et al., Enhancement of conductivity and transmittance of ZnO films by post hydrogen plasma treatment, J. Appl. Phys. 105 (2009) 083713.

[191] J.-M. Lee, K.-K. Kim, S.-J. Park, W.-K. Choi, Low-resistance and nonalloyed ohmic contacts to plasma treated ZnO, Appl. Phys. Lett. 78 (2001) 3842.

[192] http://www.beneq.com/aerosol-equipment-general.html.

[193] B.C. Cheng, Y.H. Xiao, G.S. Wu, L.D. Zhang, Controlled Growth and Properties of One-Dimensional ZnO Nanostructures with Ce as Activator/Dopant, Adv. Funct. Mater. 14 (2004) 913–919.

[194] Q. Cheng, K.K. Ostrikov, Property-performance control of multidimensional, hierarchical, single-crystalline ZnO nanoarchitectures, Chemphyschem. 13 (2012) 1535–41.

[195] C.-L. Hsu, S.-J. Chang, Y.-R. Lin, S.-Y. Tsai, I.-C. Chen, Vertically well aligned P-doped ZnO nanowires synthesized on ZnO-Ga/glass templates, Chem. Commun. (Camb). (2005) 3571–3.

[196] G.R. Li, T. Hu, G.L. Pan, T.Y. Yan, X.P. Gao, H.Y. Zhu, Morphology−Function Relationship of ZnO: Polar Planes, Oxygen Vacancies, and Activity, J. Phys. Chem. C. 112 (2008) 11859–11864.

[197] K. Fink, Ab initio cluster calculations on the electronic structure of oxygen vacancies at the polar ZnO(0001) surface and on the adsorption of H_2, CO, and CO_2 at these sites, Phys. Chem. Chem. Phys. 8 (2006) 1482–9.

[198] D.J. Lewis, P. O'Brien, Ambient pressure aerosol-assisted chemical vapour deposition of $(CH_3NH_3)PbBr_3$, an inorganic-organic perovskite important in photovoltaics, Chem. Commun. (Camb). 50 (2014) 6319–2631.

[199] D.S. Bhachu, D.O. Scanlon, E.J. Saban, H. Bronstein, I.P. Parkin, C.J. Carmalt, et al., Scalable Route to $CH_3NH_3PbI_3$ Perovskite Thin Films by Aerosol Assisted Chemical Vapor Deposition, J. Mater. Chem. A. 3 (2015) 9071–9073.

[200] M. Jiang, J. Wu, F. Lan, Q. Tao, D. Gao, G. Li, Enhancing the performance of planar organo-lead halide perovskite solar cells by using mixed halide source, J. Mater. Chem. A. 3 (2014) 963–967.

[201] D. Bi, S.-J. Moon, L. Häggman, G. Boschloo, L. Yang, E.M.J. Johansson, et al., Using a two-step deposition technique to prepare perovskite ($CH_3NH_3PbI_3$) for thin film solar cells based on ZrO_2 and TiO_2 mesostructures, RSC Adv. 3 (2013) 18762.

[202] D. Liu, M.K. Gangishetty, T.L. Kelly, Effect of $CH_3NH_3PbI_3$ Thickness on Device Efficiency in Planar Heterojunction Perovskite Solar Cells, J. Mater. Chem. A. 2 (2014) 19873–19881.

[203] W.A. Laban, L. Etgar, Depleted hole conductor-free lead halide iodide

heterojunction solar cells, Energy Environ. Sci. 6 (2013) 3249.

[204] Y.H. Lee, J. Luo, R. Humphry-Baker, P. Gao, M. Grätzel, M.K. Nazeeruddin, Unraveling the Reasons for Efficiency Loss in Perovskite Solar Cells, Adv. Funct. Mater. 25 (2015) 3925–3933.

[205] R. Lindblad, D. Bi, B. Park, J. Oscarsson, M. Gorgoi, H. Siegbahn, et al., Electronic Structure of $TiO_2/CH_3NH_3PbI_3$ Perovskite Solar Cell Interfaces, J. Phys. Chem. Lett. 5 (2014) 648–653.

[206] R. Lindblad, N.K. Jena, B. Philippe, J. Oscarsson, D. Bi, A. Lindblad, et al., Electronic Structure of $CH_3NH_3PbX_3$ Perovskites: Dependence on the Halide Moiety, J. Phys. Chem. C. 119 (2015) 1818–1825.

[207] Y. Dang, Y. Liu, Y. Sun, D. Yuan, X. Liu, W. Lu, et al., Bulk crystal growth of hybrid perovskite material $CH_3NH_3PbI_3$, CrystEngComm. 17 (2014) 665–670.

[208] H.-S. Kim, C.-R. Lee, J.-H. Im, K.-B. Lee, T. Moehl, A. Marchioro, et al., Lead iodide perovskite sensitized all-solid-state submicron thin film mesoscopic solar cell with efficiency exceeding 9%, Sci. Rep. 2 (2012) 591.

[209] Q. Chen, H. Zhou, T.-B. Song, S. Luo, Z. Hong, H.-S. Duan, et al., Controllable self-induced passivation of hybrid lead iodide perovskites toward high performance solar cells, Nano Lett. 14 (2014) 4158–4163.

Appendix A – Publications

- **S. Chen**, J. Briscoe, Y. Shi, K. Chen, R. Wilson, S. Dunn, R. Binions, A simple, low-cost CVD route to high quality $CH_3NH_3PbI_3$ perovskite thin films, *CrystEngComm* 2015, 17, 7486-7489.

- **S. Chen**, M. McLachlan, A. Sapelkin, R. Binions, Aerosol assisted chemical vapour deposition of transparent conductive ZnO thin films with hexagonal microplate surfaces and ultrahigh haze value, *Journal of Materials Chemistry A* 2015, 3, 22311-22315.

- **S. Chen**, G. Carraro, D. Barreca, A. Sapelkin, W. Chen, X. Huang, Q. Cheng, F. Zhang, R. Binions, Aerosol assisted chemical vapour deposition of Ga-doped ZnO films for energy efficient glazing: Effects of doping concentration on the film growth behaviour and opto-electronic properties, *Journal of Materials Chemistry A* 2015, 3, 13039-13049.

- **S. Chen**, R. Wilson, R. Binions, Synthesis of highly surface-textured ZnO thin films by aerosol assisted chemical vapour deposition, *Journal of Materials Chemistry A* 2015, 3, 5794-5797.

- **S. Chen**, M.E.A. Warwick, R. Binions, Effects of film thickness and thermal treatment on the structural and opto-electronic properties of Ga-doped ZnO films deposited by sol-gel method, *Solar Energy Materials and Solar Cells* 2015, 137, 202-209.

- **S. Chen**, G. Carraro, D. Barreca, R. Binions, Growth and electro-optical properties of Ga-doped ZnO films prepared by aerosol assisted chemical vapour deposition, *Thin Solid Films* 2015, 584, 316-319.

- **S. Chen**, N. Nuruzzaman, I.P. Parkin, R. Binions, Temperature and thickness dependent growth behaviour and opto-electronic properties of Ga-doped ZnO films prepared by aerosol assisted chemical vapour deposition, *Journal of Materials Chemistry A* 2014, 2, 17174-17182.

Appendix B – Conference Presentations

- A simple, low-cost CVD route to high quality $CH_3NH_3PbI_3$ perovskite thin films, ***Next Generation Materials for Solar Photovoltaics, January 13, 2016, London, UK. (Poster presentation)***

- A simple, low-cost CVD route to high quality $CH_3NH_3PbI_3$ perovskite thin films, ***20th Biennial European Conference on Chemical Vapor Deposition (EuroCVD 20), July 13-17, 2015, Sempach, Switzerland. (Poster presentation)***

- Aerosol assisted chemical vapour deposition of Ga-doped ZnO films for energy efficient glazing, ***The 1st Belux workshop on Coating, Materials, Surfaces and Interfaces, September 11-12, 2014, Belvaux, Luxembourg. (Oral presentation)***

- Aerosol assisted chemical vapour deposition of Ga-doped ZnO films for energy efficient glazing, ***The 7th International Conference on Technological Advances of Thin Films & Surface Coatings (ThinFilms2014), July 15-18, 2014, Chongqing, China. (Oral presentation)***

- Effects of film thickness and thermal treatment on the properties of 1 at.% Ga-doped ZnO films deposited by sol-gel method, ***Functional Thin Films 2013, The 4th Vacuum Symposium UK, October 17, 2013, Coventry, UK. (Poster presentation)***